

Western University

Scholarship@Western

Digitized Theses

Digitized Special Collections

2009

Growth and Characterization of Hafnium Silicate Films

Jian Liu

Follow this and additional works at: <https://ir.lib.uwo.ca/digitizedtheses>

Recommended Citation

Liu, Jian, "Growth and Characterization of Hafnium Silicate Films" (2009). *Digitized Theses*. 4159.
<https://ir.lib.uwo.ca/digitizedtheses/4159>

This Thesis is brought to you for free and open access by the Digitized Special Collections at Scholarship@Western. It has been accepted for inclusion in Digitized Theses by an authorized administrator of Scholarship@Western. For more information, please contact wlsadmin@uwo.ca.

GROWTH AND CHARACTERIZATION OF HAFNIUM SILICATE FILMS

(Thesis Format: Monograph)

by

Jian Liu

Graduate Program in Physics

A thesis submitted in partial fulfillment
of the requirements for the degree of
Doctor of Philosophy

The School of Graduate and Postdoctoral Studies
The University of Western Ontario
London, Ontario, Canada

©Jian Liu 2009

ABSTRACT

Hafnium silicate is one of the most promising high dielectric constant (high- κ) candidates being investigated as an alternative to replace SiO_2 as a gate dielectric material in complementary metal-oxide-semiconductor transistors. In this thesis, Hf silicate films were grown by atomic layer deposition using the liquid precursors tetrakis(diethylamido)hafnium (TDEAH) and tris(2-methyl-2-butoxy)silanol (TMBS). The dynamic growth processes were monitored by in situ spectroscopic ellipsometry. A self-limiting growth with a rate ~ 1 monolayer per cycle was observed only after several initial cycles – a behaviour that is ascribed to the chemistry of the initial Si substrate surface.

The film composition, as a function of the substrate temperature and TMBS pulse time, was characterized by x-ray photoelectron spectroscopy (XPS) and medium energy ion scattering (MEIS). It was found that the Hf concentration, i.e., the $\text{Hf}/(\text{Hf}+\text{Si})$ value, can only be adjusted in the range 0.22–0.30; the carbon contamination in the film can be minimized by assuring that the self-limiting condition is achieved for the TMBS precursor. A possible reaction mechanism between the TDEAH and TMBS precursors is proposed.

Hf distributions in the as-grown and annealed Hf silicate films with thicknesses in the range 4–20 nm were investigated by high resolution transmission electron microscopy (HRTEM), angle resolved x-ray photoelectron spectroscopy (ARXPS) and MEIS. HRTEM images showed a layered structure for films thinner than 8 nm. ARXPS data also showed a non-uniform distribution of Hf throughout the film depth. A diffusion of SiO_2 to the film surface after a longer time anneal was observed by MEIS. All these observations provide evidence for surface-directed spinodal decomposition in the pseudobinary $(\text{HfO}_2)_x(\text{SiO}_2)_{1-x}$ alloy system.

Key words: Atomic layer deposition; Hafnium silicate films; High- κ dielectric; Phase separation; Spinodal decomposition; Surface-directed spinodal decomposition.

STATEMENT OF CO-AUTHORSHIP

The following thesis contains material from previously published manuscripts coauthored by Jian Liu, Dr. W. N. Lennard, Prof. L. V. Goncharova, Dr. D. Landheer, Dr. X. Wu, Dr. S. A. Rushworth and Dr. A. C. Jones. All the experiments were performed by Jian Liu under the supervision of Prof. Lennard with the exception of the TEM images presented in Chapter 5, which were performed by Dr. Wu. The film growth and x-ray photoelectron spectroscopy experiments were performed by Jian Liu at IMS-NRCC under the direction of Dr. Landheer. Prof. Goncharova was included for her many helpful suggestions, and as a coauthor on a published work. Drs. Rushworth and Jones were included for providing the silicon precursor used in the film growth.

To My Parents

ACKNOWLEDGEMENTS

I would like to thank my supervisor, Prof. William Lennard, for all his support to my research and his patience with me. His extensive knowledge and guidance have made this thesis possible. I am grateful for having had the opportunity to work on this project, and am deeply satisfied with what I have learned from these studies.

I would like to thank Dr. Dolf Landheer at the National Research Council of Canada (NRCC) for providing me with the opportunity to work in his lab and for his guidance during my experiments. I am grateful to Dr. Xiaohua Wu at NRCC for his help with transmission electron microscopy experiments. I would also like to thank Dr. Jian-Hao Chen from National Chiao Tung University in Taiwan for teaching me about the intricacies of atomic layer deposition. I am indebted to Prof. Lyudmila Goncharova at UWO for helpful discussions and to my advisory committee members, Profs. Martin Zinke-Allmang and Jeffrey Hutter, for their most helpful suggestions.

I am most appreciative of the excellent technical assistance of several individuals which has benefited my research: specifically Mr. Jack Hendriks at UWO; Mr. Les Lebrun, Mr. Guy Parent and Ms. Simona Moisa at NRCC. I would like to acknowledge the administrative staff and students in the Physics and Astronomy Department who have provided assistance during my tenure at UWO.

Finally I thank my wife for her patience.

LIST OF ABBREVIATIONS

AL	Attenuation Length
ALD	Atomic Layer Deposition
ARXPS	Angle Resolved X-ray Photoelectron Spectroscopy
BE	Binding Energy
BF	Bright Field
CM	Center of Mass
CMOS	Complementary Metal Oxide Semiconductor
CRT	Cathode-Ray Tube
DF	Dark Field
EOT	Equivalent Oxide Thickness
FWHM	Full Width at Half Maximum
GISAXS	Grazing-Incidence Small Angle X-ray Scattering
HAADF	High-Angle Annular Dark Field
HRTEM	High-Resolution Transmission Electron Microscopy
IMS	Institute for Microstructural Sciences
ISP	In Situ Processing
MBE	Molecular Beam Epitaxy
MEIS	Medium Energy Ion Scattering
ML	Monolayer
MOCVD	Metal-Organic Chemical Vapour Deposition
MOSFET	Metal Oxide Semiconductor Field-Effect Transistor
NRA	Nuclear Reaction Analysis
NRCC	National Research Council of Canada
POI	Plane of Incidence
PSD	Position Sensitive Detector

PVD	Physical Vapour Deposition
RBS	Rutherford Backscattering
RCA	Radio Corporation of America
RGAs	Residual Gas Analyzer
RTA	Rapid Thermal Anneal
sccm	standard cubic centimeters per minute
SD	Spinodal Decomposition
SDSD	Surface-Directed Spinodal Decomposition
SE	Spectroscopic Ellipsometry
STEM	Scanning Transmission Electron Microscopy
TDEAH	Tetrakis(diethylamido)hafnium
TEA	Toroidal Electrostatic Analyzer
TEM	Transmission Electron Microscopy
TMBS	Tris(2-methyl-2-butoxy)silanol
XPS	X-ray Photoelectron Spectroscopy

TABLE OF CONTENTS

CERTIFICATE OF EXAMINATION	ii
ABSTRACT	iii
COAUTHORSHIP	v
DEDICATION	vi
ACKNOWLEDGEMENTS	vii
LIST OF ABBREVIATIONS	viii
TABLE OF CONTENTS	x
LIST OF FIGURES	xiii
LIST OF TABLES	xxi
1 Introduction	1
1.1 How transistors work and how to evaluate transistor performance . .	2
1.2 How to improve transistor performance	6
1.3 Scaling limit of traditional gate dielectrics: SiO_2 and SiO_xN_y	7
1.4 Requirements for high- κ dielectrics	12
1.4.1 High permittivity and high barrier height	12
1.4.2 Thermodynamic stability on Si	13
1.4.3 Interface quality	18

1.4.4	Film morphology	19
1.4.5	Process compatibility	20
2	Thin film characterization techniques	24
2.1	Spectroscopic ellipsometry	24
2.2	X-ray photoelectron spectroscopy	27
2.3	Medium energy ion scattering	32
2.3.1	Kinematics of elastic scattering and identity of the target atom	32
2.3.2	Rutherford scattering cross section and areal density of target atoms	33
2.3.3	Energy loss of incident ions and backscattering depth profile .	36
2.3.4	Toroidal electrostatic analyzer	38
2.3.5	Correction of the MEIS raw image	39
2.3.6	TEA dead time measurement	41
2.3.7	MEIS measurement geometry and an example of a MEIS spectrum	45
2.4	Transmission electron microscopy	46
3	Atomic layer deposition of Hf silicate films	53
3.1	Atomic layer deposition	53
3.2	Precursor consideration	55
3.3	Deposition of Hf silicate films by ALD	58
3.3.1	ALD facility and preparation of silicon substrate	58
3.3.2	ALD growth process of Hf silicate films	61
3.4	Discussion and conclusion	68
4	Film composition and reaction mechanism between TDEAH and TMBS	72
4.1	Film composition	72

4.1.1	XPS analysis	72
4.1.2	MEIS analysis	81
4.1.3	NRA analysis of nitrogen impurity	83
4.1.4	Discussion	86
4.2	Reaction mechanism between TDEAH and TMBS	87
4.3	Summary	93
5	Film structure	97
5.1	Surface-directed spinodal decomposition	98
5.2	Surface-directed spinodal decomposition in Hf silicate films	101
5.2.1	Structure of the as-grown films	101
5.2.2	Film structure after RTA	107
5.2.3	Thickness effect on film structure	112
5.2.4	Film structure after long time anneal	115
5.2.5	XPS and MEIS analysis	121
5.3	Discussion and conclusion	129
6	Conclusions	134
A	Copyright permission	137
A.1	Copyright permission for material contained within Chapter 3 and Chapter 4	138
A.2	Copyright permission for material contained within Chapter 5	139
	CURRICULUM VITAE	140

LIST OF FIGURES

1.1	Moore's Law and scaling of transistor dimensions. The number of transistors (solid diamonds), transistor minimum lateral feature size (open triangles), and transistor minimum physical oxide thickness (solid circles) are shown as a function of time. Red symbols are anticipated technology. Data were extracted from Intel website: www.intel.com . Solid lines are to guide the eye.	2
1.2	Schematic of the cross-section of an nMOSFET transistor.	3
1.3	Circuit symbols and voltage terminals of (a) nMOSFET and (b) pMOSFET. After Ref. [2].	4
1.4	Circuit diagram of a CMOS inverter. After Ref. [2].	5
1.5	Gate leakage current as a function of EOT for SiO_2 and $(\text{SiO}_2)_{x/2}(\text{Si}_3\text{N}_4)_{1-x/2}$. See Ref. [7].	9
1.6	Bonding structure of SiO_2 indicating the minimum thickness of the bulk oxide is about 0.7 nm. See Ref. [11].	10
1.7	Energy-band diagram for a ideal metal-dielectric-semiconductor structure, after [21].	13
1.8	Predicted barrier heights for a range of high- κ gate oxides. After Ref. [22].	14
1.9	Static dielectric constant versus band gap for candidate gate oxides. The dashed curve is to guide the eye. After Ref. [22].	14
1.10	Calculated phase diagrams for (a) Ta–Si–O and (b) Ti–Si–O systems in the temperature range 700–1000 °C. After Ref. [23].	15

1.11	Phase diagram for Zr–Si–O system in the temperature range 700–950 °C. After Ref. [24].	16
1.12	Summary of which elements have an oxide that may be thermodynamically stable in contact with silicon at 1000 K. Adapted from Ref. [25].	17
2.1	Schematic of a light beam reflecting from a surface.	25
2.2	A light ray propagates from medium 1 with complex index of refraction \tilde{N}_1 into medium 2 with complex index of refraction \tilde{N}_2 . The angle of reflection and angle of refraction are ϕ_1 and ϕ_2 , respectively.	26
2.3	Reflections and transmissions of a light ray incident upon a thin film on top of a thick substrate.	27
2.4	Schematic of the relevant energy levels for binding energy measurements. Note that the conducting sample and spectrometer are in electrical contact and thus have common Fermi levels. $h\nu$ is the incident photon energy. E_{kin}^1 is the photoelectron kinetic energy relative to the vacuum level of the sample. The work function difference between the spectrometer and the sample is $\phi_{spec} - \phi_s$. After Ref. [4].	29
2.5	Si 2p XPS peaks for a 5 nm Hf silicate film on a Si substrate at photoelectron takeoff angles of 75° (solid line) and 45° (dashed line). . .	30
2.6	Schematic for ARXPS measurements.	30
2.7	Schematic representation of an elastic collision between a projectile of mass M_1 , energy E_0 and a target of mass M_2 which is initially at rest. After collision, the energies of the projectile and the target are E_1 and E_2 , and their (laboratory) scattering angles are θ and ϕ , respectively. After [4].	33
2.8	Plot of the kinematic factor as a function of scattering angle for protons on Hf, Si, O and C targets.	34

2.9	Travelling path of an incident ion in the target. The target normal is tilted θ_1 degree from the incident ion beam. As an incident ion with initial energy E_0 travels a distance $t/\cos\theta_1$ in the target, its energy reduces to E . Then the incident ion loses energy $(1 - k)E$ during the subsequent elastic scattering. θ is the lab scattering angle. The scattered ion then loses a certain amount of energy on its way out of the target with its final detected energy E_1 . After Ref. [4].	37
2.10	Schematic of the toroidal electrostatic analyzer system.	38
2.11	Schematic of the charge dividing collector. The electron cloud produced by the scattered ion impinging on the microchannel plates is analyzed. The charge is drained to four charge sensitive amplifiers A, B, C and D. The angle and energy of the scattered ion are determined by the relative values of the charges collected by amplifiers A, B, C and D.	40
2.12	Ta edge for 100 keV incident protons at angle channel 120 fitted by an error function. The coordinates of the half-height point are shown. .	41
2.13	dE/dC for each angular position of the PSD.	42
2.14	Channel position corresponding to 98.4 keV scattered protons for a TEA setting of 96.1 keV for each angular channel.	42
2.15	Output count rate versus input count rate for the TEA. The solid curve is a fit to a paralyzable model. The dashed line shows the simulation where the output count rate is equal to the input count rate.	44
2.16	Illustration of two idealized models of dead time behaviour for radiation detectors. After Ref. [12].	45

2.17	Schematic of MEIS measurement geometry. Thin films were grown on a Si(100) substrate. The incident beam was aligned to the $\langle 101 \rangle$ direction and the scattered ions towards the $\langle 10\bar{1} \rangle$ direction were detected by the TEA.	46
2.18	A 2-dimensional spectrum for a 4 nm Hf silicate film grown on Si(100). The incident beam is 95 keV $^1\text{H}^-$ ions and the sample is aligned in the geometry shown in Fig. 2.17.	47
2.19	The RBS spectrum taken from Fig. 2.18 at scattering angle 90° . . .	47
2.20	Schematic ray path for the two basic operations of a TEM imaging system: (a) projecting the diffraction pattern on the viewing screen and (b) projecting the image onto the viewing screen. After Ref. [13].	49
2.21	The creation of a stationary diffraction pattern in the back focal plane of the objective lens in STEM imaging. After Ref. [13].	50
2.22	Schematic of the HAADF detector setup in a STEM. After Ref. [13].	51
3.1	Scheme of (a) an ALD window limited by (b) precursor condensation, (c) insufficient reactivity, (d) precursor decomposition and (e) precursor desorption. If the decomposition rate is dependent on the number of available reactive sites as in (f), actual ALD window cannot be observed. After ref [5].	54
3.2	Schematic molecular structures of (a) TDEAH and (b) TMBS. . . .	57
3.3	Vapour pressures of TDEAH and TMBS.	57
3.4	ISP processing facility for 4-inch wafer at NRCC-IMS.	58
3.5	Schematic of the ALD system at NRCC-IMS.	59
3.6	Si 2p XPS peaks before and after substrate oxidation.	60
3.7	Growth process of a film deposited at 350°C : a – film thickness measured by ellipsometry; b – Ar partial pressure; c – N_2 partial pressure; d – H_2O partial pressure.	62

3.8	Growth rate as a function of cycle number for the growth shown in Fig. 3.7.	63
3.9	Details of the variation of the film thickness and gaseous partial pressures during the 15th growth cycle of the deposition (at 350 °C) shown in Fig. 3.7: film thickness (solid curve) measured by ellipsometry; Ar partial pressure (dashed curve); N ₂ partial pressure (dotted curve). Note that TDEAH is delivered by argon, while TMBS is delivered by nitrogen.	64
3.10	Film thickness as a function of the number of cycles at T _{sub} = 350 °C. Slope of linear fit (solid line) to TEM data = 0.33 ± 0.02 nm/cycle; slope of linear fit (dashed line) to ellipsometry data = 0.31 ± 0.03 nm/cycle.	65
3.11	One of the growth cycles at T _{sub} = 200 °C: film thickness (solid curve) measured by ellipsometry; Ar partial pressure (dashed curve); N ₂ partial pressure (dotted curve).	65
3.12	Growth rate as a function of TMBS pulse time for three substrate temperatures (curves are to guide the eye).	66
3.13	Film deposition at T _{sub} = 200 °C and N ₂ flow rate 40 sccm: film thickness (solid curve) measured by ellipsometry; Ar partial pressure (dashed curve); N ₂ partial pressure (dotted curve).	67
3.14	One of the growth cycles at T _{sub} = 375 °C: film thickness (solid curve) measured by ellipsometry; Ar partial pressure (dashed curve); N ₂ partial pressure (dotted curve).	67
3.15	Film thickness as function of cycle number measured by ellipsometry for a film deposited on SC1 cleaned SiO ₂ surface at T _{sub} = 350 °C. .	69
4.1	Ex situ XPS peaks of a film deposited at 350 °C: (a) Si 2p, (b) Hf 4f, and (c) O 1s peaks.	74

4.2	XPS peaks of a film before and after in situ anneal at 800°C for ~2 s: (a) Si 2p, (b) Hf 4f and (c) O 1s peaks.	76
4.3	C 1s XPS peaks: (a) in situ, (b) ex situ after several days of exposure to air.	77
4.4	C 1s XPS peaks before and after in situ anneal.	78
4.5	in situ N 1s XPS peak for a film deposited at 350°C.	79
4.6	(a) MEIS spectrum for the sample deposited at 350°C. The arrows indicate the positions of surface edges of Hf, Si, O and C, respectively. (b) The depth profiles of Hf, Si, O and C extracted from a fit to the spectrum shown in (a).	82
4.7	NRA measurements of N content in Hf silicate films.	84
4.8	Proposed reaction mechanism between TDEAH and TMBS. Me ↔ [–CH ₃] group; Et ↔ [–C ₂ H ₅] group; R ↔ [–C(CH ₃) ₂ C ₂ H ₅] group. .	89
4.8	Proposed reaction mechanism between TDEAH and TMBS. Me ↔ [–CH ₃] group; Et ↔ [–C ₂ H ₅] group; R ↔ [–C(CH ₃) ₂ C ₂ H ₅] group. (cont.)	90
5.1	Typical temperature dependence of the free energy of a system pre- senting a miscibility gap ($T_1 < T_c < T_2$).	99
5.2	Example of a miscibility gap and a spinodal line.	100
5.3	(a) BF image of a 5.3 nm as-grown film; (b) line intensity profile inte- grated over the width of the rectangle shown in (a); (c) DF image of the 5.3 nm as-grown film.	103
5.4	(a) BF image of a 4 nm as-grown film; (b) line intensity profile inte- grated over the width of the rectangle shown in (a).	104
5.5	(a) BF image of a 6.1 nm as-grown film; (b) line intensity profile inte- grated over the width of the rectangle shown in (a); (c) DF image of the 6.1 nm as-grown film.	105

5.6	(a) BF image of a 12.5 nm as-grown film; (b) line intensity profile integrated over the width of the rectangle shown in (a); (c) DF image of the 12.5 nm as-grown film.	106
5.7	(a) BF image of the 5.3 nm film after RTA; (b) line intensity profile integrated over the width of the rectangle shown in (a).	107
5.8	(a) BF image of the 6.1 nm film after RTA; (b) line intensity profile integrated over the width of the rectangle shown in (a); (c) DF image of the 6.1 nm film after RTA.	109
5.9	(a) BF image of a ~ 6.9 nm film after RTA; (b) line intensity profile integrated over the width of the rectangle shown in (a).	110
5.10	(a) BF image of the 12.5 nm film after RTA; (b) line intensity profile integrated over the width of the rectangle shown in (a); (c) DF image of the 12.5 nm film after RTA.	111
5.11	Si 2p XPS peaks of the 6.1 nm film before and after HF etch.	114
5.12	Si 2p XPS peaks of the HF etched 6.1 nm film (Fig. 5.11) before and after RTA.	114
5.13	(a) BF image of the 6.1 nm film after RTA, HF etch and RTA; (b) line intensity profile integrated over the width of the rectangle shown in (a); (c) DF image of the 6.1 nm film after RTA, HF etch and RTA.	116
5.14	(a) BF image of the 12.5 nm film after RTA, HF etch and RTA; (b) line intensity profile integrated over the width of the rectangle shown in (a).	117
5.15	(a) BF image of the 6.1 nm film after 600 s anneal at 800 °C in N ₂ ; (b) line intensity profile integrated over the width of the rectangle shown in (a); (c) DF image of the 6.1 nm film after 600 s anneal at 800 °C in N ₂	119

5.16	(a) BF and (b) DF images of the 12.5 nm film after 600 s anneal at 800 °C in N ₂ . Some of the crystalline regions are encircled.	120
5.17	(a) BF image of a 20 nm as-grown film; (b) line intensity profile integrated over the width of the rectangle shown in (a); (c) DF image of the 20 nm as-grown film. Some of the crystalline regions are encircled.	122
5.18	Plan-view BF images of the 6.1 nm film: (a) after RTA and (b) after a 600 s anneal at 800 °C in N ₂	123
5.19	ARXPS peaks for the 5.3 nm film before and after RTA at $\theta = 45^\circ$ and 75° : (a) Si 2p; (b) Hf 4f; (c) O 1s.	125
5.20	ARXPS Hf 4f peaks for the 6.1 nm as-grown film, and for the same film after RTA and 600 s anneal at 800 °C in N ₂	126
5.21	Schematic of the layered structure of the 5.3 nm film.	128
5.22	MEIS spectra of the 6.1 nm film: as-grown, after RTA and after 600 s anneal at 800 °C in N ₂	129

LIST OF TABLES

1.1	Gate oxide (SiO_2) scaling limits under different circumstances. After Ref. [7].	8
2.1	PSD output count rate for protons scattered from Ta_2O_5 in the energy range 95–99 keV for different ion beam current intensities.	43
3.1	A typical film deposition cycle.	60
4.1	As-grown film composition calculated from in situ XPS data and MEIS data.	80
4.2	Parameters derived from a fit to the MEIS spectrum shown in Fig. 4.6(a).	81
4.3	Details of the samples used for NRA.	85
4.4	N areal density measured by NRA.	85
5.1	Si 2p XPS peak intensities.	113
5.2	Summary of binding energies and peak widths of Hf 4f _{7/2} peaks shown in Fig. 5.19(b).	124
5.3	Hf concentration extracted from ARXPS.	127

CHAPTER 1

INTRODUCTION

The integrated circuit is one of the most important inventions of the last century. It has revolutionized the world of information technology. Integrated circuits can be found in almost every modern electrical device: e.g., computers, cars, television sets, mp3 players, cellular phones, etc. The most fundamental component of integrated circuits is the metal oxide semiconductor field-effect transistor (MOSFET). MOSFETs are basically switches that process the ones and zeroes that make up our digital world. Transistors have been made smaller and smaller. By making smaller transistors, more of them could be integrated in a single chip. Smaller transistors can run faster, consume less power, and cost less. In 1965, Gordon Moore predicted that the number of transistors on a chip will double about every two years [1]. Later, his prediction was named “Moore’s Law”. The industry has been working hard to follow Moore’s law since then. The exponential increase in the device density and decrease in the device dimension is called “scaling” in the semiconductor industry. Figure 1.1 shows the increase of the number of transistors on a processor (solid diamonds), the decrease of the feature size (open triangles) and the gate oxide thickness (solid circles) since 1970. In 1970, a transistor had a dimension of tens of micrometers and an integrated circuit had thousands of transistors. Today’s transistors have a dimension

of only tens of nanometers. With Intel's 32 nm technology, which is going into production in 2009, 1.9 billion transistors can be integrated on a chip. Over 4 million 32 nm transistors can be fitted on the period at the end of this sentence (estimated to be $1/10 \text{ mm}^2$ in area). The technology has brought vast performance improvement to integrated circuits. In this chapter, the working principle of transistors and the main methods of improving transistor performance are briefly reviewed.

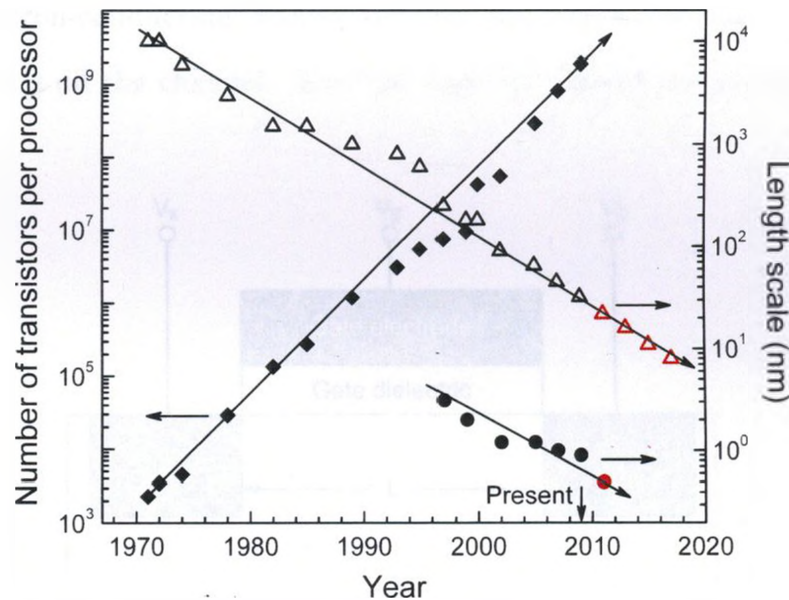


Figure 1.1: Moore's Law and scaling of transistor dimensions. The number of transistors (solid diamonds), transistor minimum lateral feature size (open triangles), and transistor minimum physical oxide thickness (solid circles) are shown as a function of time. Red symbols are anticipated technology. Data were extracted from Intel website: www.intel.com. Solid lines are to guide the eye.

1.1 How transistors work and how to evaluate transistor performance

There are two kinds of MOSFETs: n(for n-type)MOSFET and p(for p-type)MOSFET. Figure 1.2 shows the basic structure of an nMOSFET, in which the device is built on

p-type silicon substrate. The source and drain regions are made of highly doped n-type silicon. Between them lies the transistor channel, a lightly doped p-type region. On top of the channel lies a thin layer of dielectric called the gate oxide, which used to be made of SiO_2 . The gate electrode, which is made of polycrystalline silicon (in the case of nMOSFET, it is also n-type), stacks on the gate oxide. The nMOSFET works like this: a positive voltage on the gate attracts the electrons in the substrate to form an electron-conducting channel between the source and drain, while a negative voltage shuts off the channel. The “on” and “off” states can therefore represent “1” and “0”.

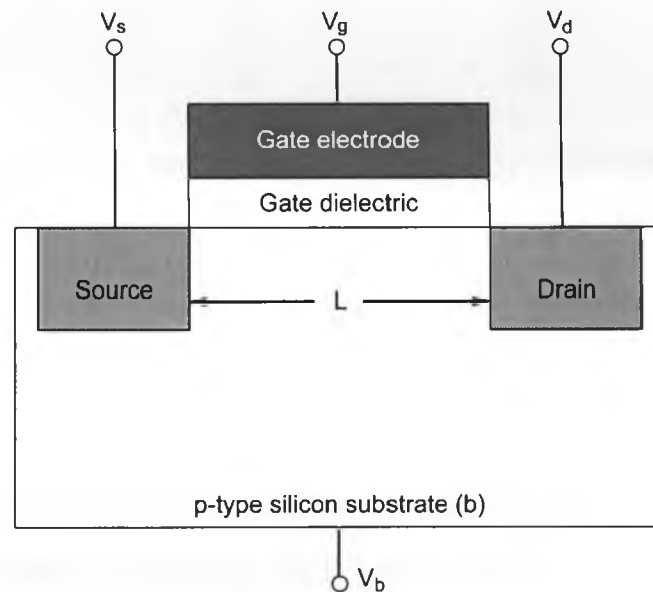


Figure 1.2: Schematic of the cross-section of an nMOSFET transistor.

A pMOSFET is just the complement of nMOSFET. The substrate and channel are n-type, while the source, drain and the gate are p-type. A negative voltage turns on the pMOSFET.

The circuit symbols for nMOSFETs and pMOSFETs are shown in Fig. 1.3. A MOSFET has four terminals. Unless specified, the body terminal (p-substrate) of an nMOSFET is connected to the ground (lowest voltage), while the body terminal

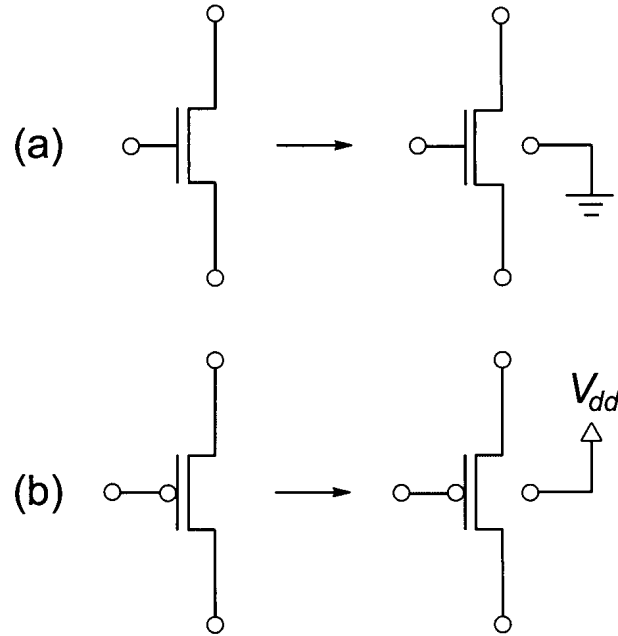


Figure 1.3: Circuit symbols and voltage terminals of (a) nMOSFET and (b) pMOSFET. After Ref. [2].

(n-substrate) of a pMOSFET is connected to the power supply V_{dd} (highest voltage).

Transistor performance can be evaluated by the most basic element of digital static complementary metal oxide semiconductor (CMOS) circuit, the CMOS inverter, which is a combination of an nMOSFET and a pMOSFET. Figure 1.4 shows the diagram of a CMOS inverter. The source terminal of the nMOSFET is connected to the ground, while the source of the pMOSFET is connected to V_{dd} . The gates of the two MOSFETs are tied together as the input node. The two drains are tied together as the output node. The CMOS inverter works like this: when the input voltage is high ($V_{in} = V_{dd}$), the nMOSFET is on and the pMOSFET is off. The nMOSFET channel is conducting. Therefore, the output is equal to ground, i.e., $V_{out} = 0$. On the other hand, when input voltage is low ($V_{in} = 0$), the pMOSFET is turned on while the nMOSFET is turned off. The output voltage is high, i.e., $V_{out} = V_{dd}$. Since the output voltage is always the opposite to the input voltage, this circuit is called

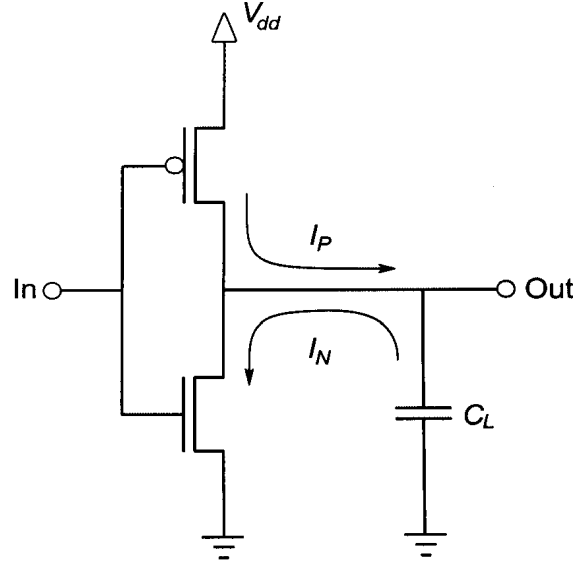


Figure 1.4: Circuit diagram of a CMOS inverter. After Ref. [2].

an inverter.

When the nMOSFET is on, it can be shown that the switching time, i.e. the time required to pull the output voltage from V_{dd} down to $V_{dd}/2$ is [2]

$$\tau_n = \frac{C_L V_{dd}}{2I_{Nsat}}, \quad (1.1)$$

where C_L is the load capacitance, I_{Nsat} is the saturation current flowing through the nMOSFET channel.

Similarly, when the pMOSFET is on, the switching time to pull the output voltage from 0 up to $V_{dd}/2$ is

$$\tau_p = \frac{C_L V_{dd}}{2I_{Psat}}. \quad (1.2)$$

Therefore, the average switching time is

$$\bar{\tau} = \frac{\tau_n + \tau_p}{2} = \frac{C_L V_{dd}}{4} \left(\frac{1}{I_{Nsat}} + \frac{1}{I_{Psat}} \right), \quad (1.3)$$

which indicates the response speed of a CMOS inverter.

1.2 How to improve transistor performance

Equation 1.3 shows that increases of I_{Nsat} and I_{Psat} help to reduce the CMOS inverter switching time. Using the so-called gradual-channel approximation, the drain current, I_N , flowing through the channel of an nMOSFET can be expressed as [3]

$$I_N = \frac{W}{L} \mu C_{inv} \left(V_G - V_T - \frac{V_D}{2} \right) V_D, \quad (1.4)$$

where W is the width of the transistor, L is the length of the channel, μ is the channel carrier mobility, C_{inv} is the gate-insulator capacitance, and V_G , V_T and V_D are the gate voltage, threshold voltage and drain voltage, respectively. The channel carrier mobility μ can be assumed constant. From Equation 1.4, it can be seen that I_N increases linearly with V_D , and then reaches its maximum value when $V_{D,sat} = V_G - V_T$,

$$I_{Nsat} = \frac{W}{L} \mu C_{inv} \frac{(V_G - V_T)^2}{2}. \quad (1.5)$$

The increase of V_G is limited because too large a V_G will result in an undesirable, high electric field across the gate dielectric. Thus, even in this simplified approximation, we can see that a reduction in the channel length or increase in the gate-insulator capacitance will result in an increase of the drain current.

In the case of increasing gate capacitance, if we consider a parallel plate capacitor, the capacitance is

$$C = \frac{\kappa \epsilon_0 A}{t}, \quad (1.6)$$

where κ is the dielectric constant, ϵ_0 is the permittivity of free space, A is the area and t is the thickness of the dielectric. As can be seen from Equations 1.6, 1.5 and 1.3, a decrease of the gate insulator thickness will result in an increase of the gate capacitance and drain current, and therefore a decrease of CMOS inverter switching time.

1.3 Scaling limit of traditional gate dielectrics: SiO_2 and SiO_xN_y

As the gate dielectric, thermally grown SiO_2 had ruled the semiconductor industry for over 40 years because of its unique properties: high band gap (9.0 eV), low interface state density in contact with Si ($\sim 10^{10} \text{ cm}^{-2} \text{ eV}^{-1}$) and thermodynamic stability on Si. As the SiO_2 thickness enters the nanometer regime, the direct tunneling current increases exponentially with the decrease of gate oxide thickness. Silicon nitride, Si_3N_4 , has a higher dielectric constant ($\kappa \sim 7$) than SiO_2 ($\kappa \sim 3.9$). However, application of a pure nitride layer at the channel interface degrades the device performance [4]. In contrast, improved electrical properties have been reported by using various silicon oxynitrides, i.e., SiO_xN_y [5, 6], which has a dielectric constant in the range $3.9 < \kappa < 7$ depending on x and y values and therefore offers a short term solution for CMOS scaling.

An important term should be introduced to characterize the dielectrics with higher κ than SiO_2 , i.e., equivalent oxide thickness (EOT). The EOT represents the theoretical

thickness of SiO_2 that would be required to achieve the same capacitance density as the dielectric. If $t_{\text{high-}\kappa}$ is the thickness of a high- κ dielectric to achieve the same capacitance density as SiO_2 with a thickness of t_{EOT} , from Equation 1.6, we have

$$\frac{C}{A} = \frac{\kappa_{\text{high-}\kappa} \epsilon_0}{t_{\text{high-}\kappa}} = \frac{\kappa_{\text{SiO}_2} \epsilon_0}{t_{\text{EOT}}}, \quad (1.7)$$

therefore,

$$\frac{\kappa_{\text{high-}\kappa}}{t_{\text{high-}\kappa}} = \frac{\kappa_{\text{SiO}_2}}{t_{\text{EOT}}}, \quad (1.8)$$

or

$$t_{\text{high-}\kappa} = \frac{\kappa_{\text{high-}\kappa}}{\kappa_{\text{SiO}_2}} t_{\text{EOT}}. \quad (1.9)$$

The scaling limits of gate oxides depend on leakage current and the power consumption of specific applications. Lo and Taur [7] calculated the tunneling current for SiO_2 and $(\text{SiO}_2)_{x/2}(\text{Si}_3\text{N}_4)_{1-x/2}$ as a function of EOT (Fig. 1.5) and analyzed the scaling limit of SiO_2 for different applications (Table 1.1). For example, as far as the functionality of a single transistor is concerned, the oxide thickness can be aggressively scaled to 0.5 nm according to their calculation.

Table 1.1: Gate oxide (SiO_2) scaling limits under different circumstances. After Ref. [7].

Application	Tolerable gate current density (A/cm^2)	Gate oxide (SiO_2) limit (nm)	Gate length limit (nm)
Single transistor/circuit	10^6	0.5	10
High performance processor/logic	10^3	1	20
Low power processor and SRAM	10	1.5	40
DRAM cell transistor	3×10^{-4}	2.5	100

On the other hand, the scaling down of the gate oxide thickness raised the issue as to how far the SiO_2 thickness can be reduced while still maintaining its bulk properties.

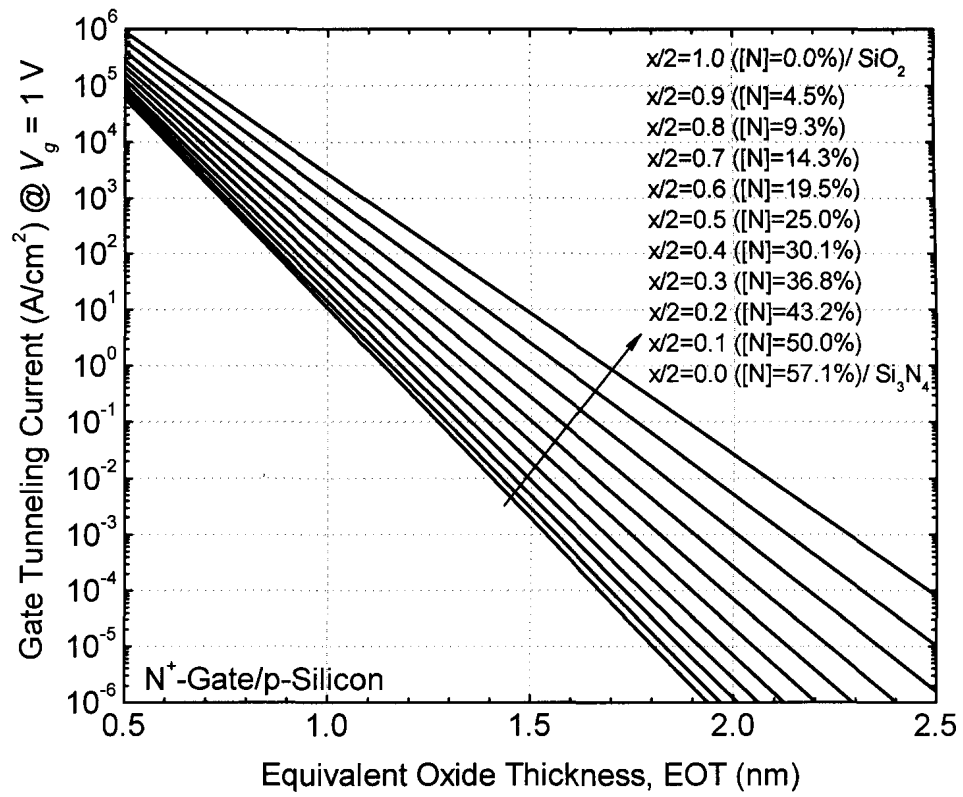


Figure 1.5: Gate leakage current as a function of EOT for SiO_2 and $(\text{SiO}_2)_{x/2}(\text{Si}_3\text{N}_4)_{1-x/2}$. See Ref. [7].

Experiments and calculations have been done on ultrathin SiO_2 films on Si. Tang *et al.* [8] studied the electronic structure of SiO_2/Si interface using first-principles pseudopotential method. They concluded that the conduction band offset increases with the thickness of the SiO_2 and saturates for oxide thickness of 0.7 nm and beyond. Muller *et al.* [9] studied the unoccupied electronic density of state of SiO_2 films by measuring the oxygen K-edge in electron energy loss spectroscopy (with a probe size of ~ 0.26 nm). Their study showed that after two monolayers of SiO_2 from the Si channel interface, oxygen atoms have the full arrangement of the second nearest oxygen neighbours and therefore form the full band gap that exists in bulk SiO_2 . The first-principles study by Neaton *et al.* [10] showed that the energy gap for a given O atom of SiO_2 is determined by the number of O second nearest neighbours. The first row of O atoms cannot have the full six second nearest neighbour O atoms. Thus the second row of O atoms is the first layer of O atoms that have the required six second nearest neighbour O atoms. The thickness required for SiO_2 to have a full width band gap is therefore 0.16 nm (one Si–O bond length) $+ 2 \times 0.27 \text{ nm}$ (the distance between two neighbouring O atoms) $= 0.7 \text{ nm}$ (as shown in Fig. 1.6).

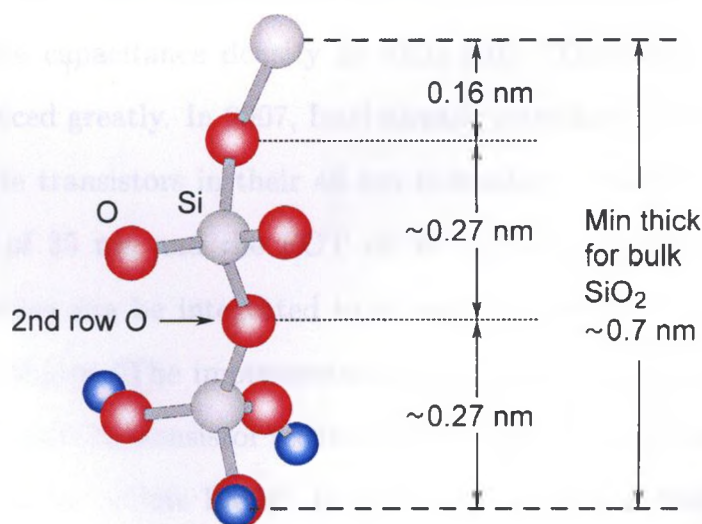


Figure 1.6: Bonding structure of SiO_2 indicating the minimum thickness of the bulk oxide is about 0.7 nm. See Ref. [11].

This conclusion is in agreement with the calculation by Tang *et al.* [8] and the experiment by Muller *et al.* [9] Thus 0.7 nm is the ultimate thickness limit of SiO₂ to maintain its bulk properties. However, the technologically achievable thickness of SiO₂ is much larger than the theoretical limit. The thickness of the interface in the form of suboxide between SiO₂ and the silicon substrate is ~ 0.5 nm depending on the processing condition. Also interfacial roughness may increase the technologically feasible lowest SiO₂ thickness. It has been reported that transistors with gate oxides as thin as 1.3–1.5 nm can operate satisfactorily [12–15]. Although the leakage current density can be as high as 1.0–10 A/cm² (at V_{dd}), transistors for high performance microprocessor applications can sustain these currents, as listed in Table 1.1. Later, Timp *et al.* [14, 16] found that further reducing SiO₂ gate oxide to about 1.0–1.2 nm in CMOS structure results in no further gains in transistor drive current. This result has been confirmed by other groups [15, 17, 18]; thus the practical limit for reducing SiO₂ thickness in CMOS technology is ~ 1.0 –1.2 nm.

Therefore, high- κ materials must be found in order to further scale CMOS transistors [19]. With high- κ dielectrics, a physically thicker layer can be used as gate insulator to achieve the same capacitance density as SiO₂ [20]. Thus, the leakage current density can be reduced greatly. In 2007, Intel already introduced the first generation high- κ + metal gate transistors in their 45 nm technology. Intel's 45 nm transistor has a gate length of 35 nm and the EOT of its high- κ gate dielectric is 1.0 nm. 820 million transistors can be integrated in a single processor. According to Intel cofounder Gordon Moore, "The implementation of high- κ and metal gate materials marks the biggest change in transistor technology since the introduction of polysilicon gate MOS transistors in the late 1960s". In the fourth quarter of 2009, Intel's 32 nm technology, the second generation high- κ + metal gate, will go into production. The 32 nm transistors have a gate length of 30 nm, and its high- κ gate insulator layer has an EOT of 0.9 nm. Intel expects to push CMOS technology forward until 2017 to 8

nm technology. The research toward this goal is underway.

1.4 Requirements for high- κ dielectrics

Any high- κ material must meet a set of requirements to replace SiO_2 as a successful gate dielectric.

1.4.1 High permittivity and high barrier height

We have already seen that materials that can be used to replace SiO_2 as gate dielectrics must have higher permittivity than SiO_2 in order to improve the performance of the CMOS devices. However, this higher permittivity requirement must be balanced against the barrier height for the tunneling process. This barrier height is $\Delta E_C = q[\chi - (\Phi_M - \Phi_B)]$, for electrons travelling from the silicon substrate to the gate, and Φ_B for electrons travelling from the gate to the silicon substrate (Fig. 1.7).

The direct tunneling leakage current can be expressed as [21]

$$J_{DT} = \frac{A}{t_{diel}^2} \exp \left(-2t_{diel} \sqrt{\frac{2m^*q}{\hbar^2} \left\{ \Phi_B - \frac{V_{diel}}{2} \right\}} \right), \quad (1.10)$$

where A is a constant, t_{diel} is the physical thickness of the dielectric, V_{diel} is the voltage drop across the dielectric, and m^* is the electron effective mass in the dielectric. Equation 1.10 shows that the direct tunneling current increases exponentially with decreasing barrier height. Therefore, gate dielectrics with high barrier height to silicon are desirable in order to obtain low leakage current.

A large band gap E_G generally corresponds to a large ΔE_C . Figure 1.8 shows the

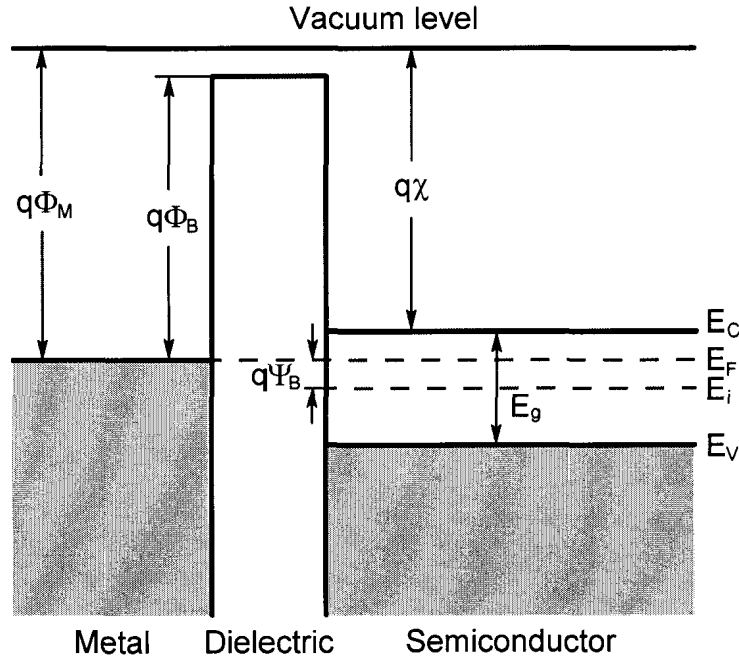


Figure 1.7: Energy-band diagram for a ideal metal-dielectric-semiconductor structure, after [21].

ΔE_C values for some high- κ dielectrics calculated by Robertson [22]. Materials with $\Delta E_C < 1.0$ eV are less likely to be used in gate dielectric applications. Figure 1.9 shows that the κ value of the candidate oxides tends to vary inversely with the band gap. Therefore, the choice of high- κ must be balanced by the value of band offset.

1.4.2 Thermodynamic stability on Si

Any potential gate dielectrics must be thermodynamically stable in direct contact with Si. The gate dielectric/Si substrate structure should be capable of withstanding a $\sim 900^\circ\text{C}$ annealing step which is the dopant activation process of the source and drain in the transistor making process. The gate dielectrics must not react with Si to form either SiO_2 or silicide. The SiO_2 layer in series with a high- κ dielectric will nullify the benefit of the high- κ dielectric since the required EOT of the gate

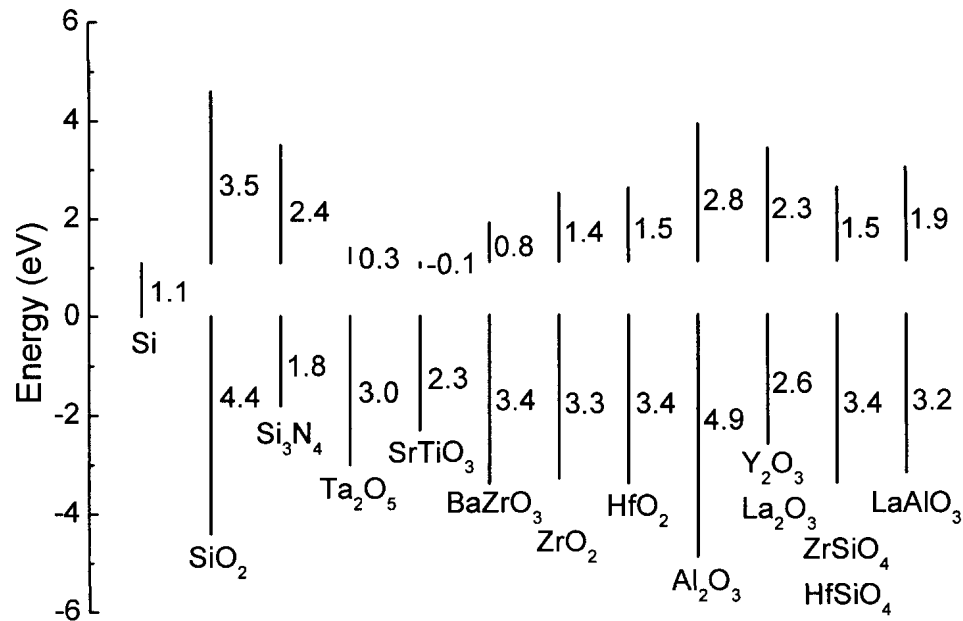


Figure 1.8: Predicted barrier heights for a range of high- κ gate oxides. After Ref. [22].

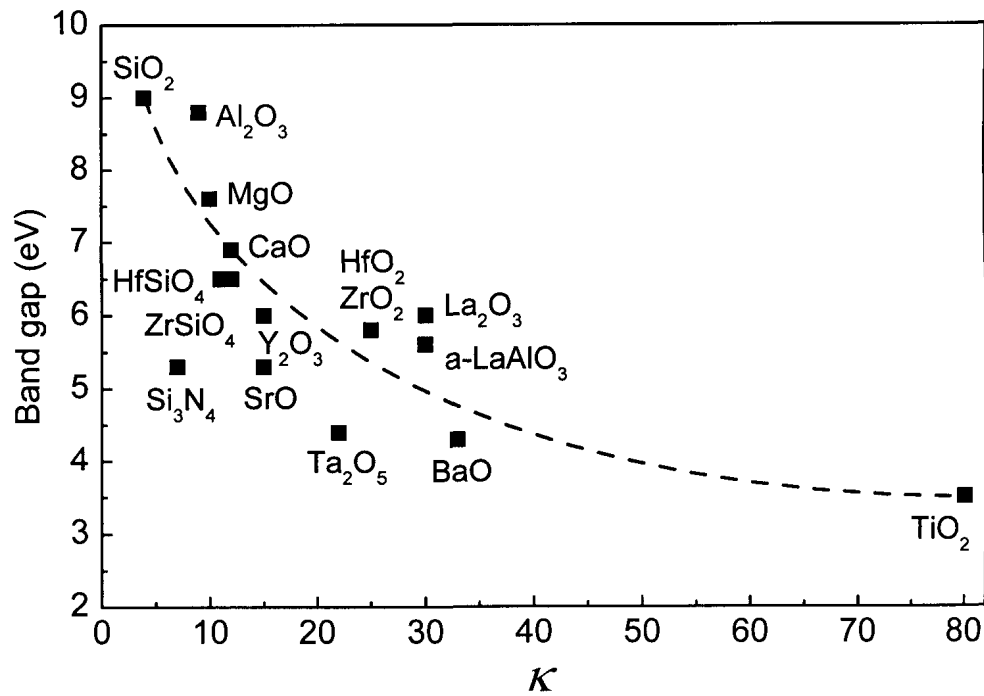


Figure 1.9: Static dielectric constant versus band gap for candidate gate oxides. The dashed curve is to guide the eye. After Ref. [22].

stack in future MOSFETs is <1 nm. The silicide formed at the interface is generally conductive and would short out the field effect.

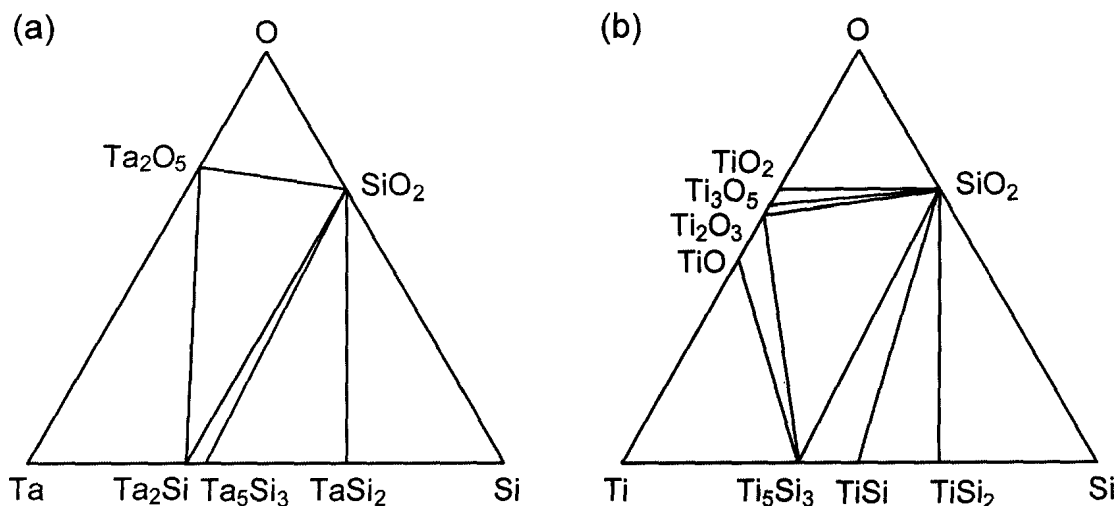


Figure 1.10: Calculated phase diagrams for (a) Ta–Si–O and (b) Ti–Si–O systems in the temperature range 700–1000 °C. After Ref. [23].

An important approach to predict the relative stability of a three-component system can be explained through a ternary phase diagram. The ternary phase diagrams for Ta–Si–O and Ti–Si–O systems were calculated through an analysis of the Gibbs free energies governing the relevant chemical reactions [23] and are shown in Fig. 1.10. A given point in the diagram represents the relative compositions of phases that can be stable with each other at a certain temperature. The stable phases are defined by the points which connect those tie lines, which cannot cross. Tie lines connect two compositions that can be in equilibrium with each other – without reaction. As can be seen from Fig. 1.10, Ta_2O_5 and TiO_2 are not stable in contact with Si and tend to react with Si to form SiO_2 and silicide. In contrast to the Ta–Si–O and Ti–Si–O systems, the tie lines in the phase diagram for the Zr–Si–O system, shown in Fig. 1.11, indicate that ZrO_2 and ZrSiO_4 and indeed any composition $(\text{ZrO}_2)_x(\text{SiO}_2)_{1-x}$ is stable in contact with Si up to high temperatures.

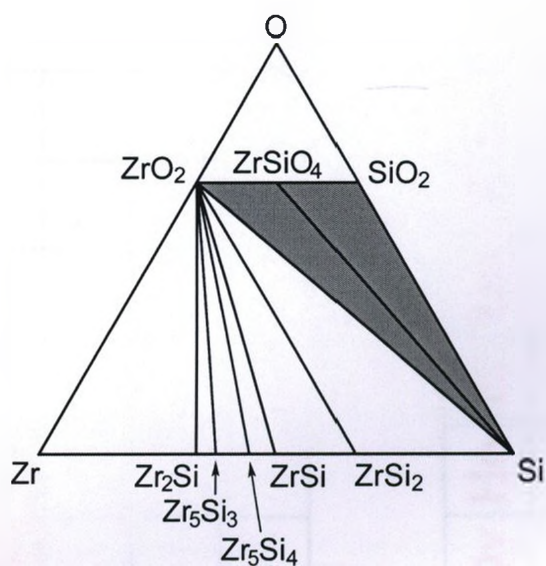


Figure 1.11: Phase diagram for Zr–Si–O system in the temperature range 700–950 °C. After Ref. [24].

Hubbard and Schlom calculated the thermodynamic stability for oxides of all the elements in the periodic table [25]. Figure 1.12 shows only the elements that may have stable oxides on a silicon substrate (see Ref. [25] for the reasons why other elements are eliminated). As can be seen from Fig. 1.12, there are only few oxides which are thermodynamically stable on Si: BeO, MgO, CaO, SrO, Al₂O₃, ZrO₂, HfO₂, Y₂O₃, La₂O₃ and the lanthanides. The group II oxides SrO, etc., are excluded because they are very reactive with water. The candidates left are Al₂O₃, ZrO₂, HfO₂, Y₂O₃, La₂O₃ and various lanthanides such as Ce₂O₃, Pr₂O₃, Nd₂O₃ and Gd₂O₃.

Al₂O₃ has the disadvantage of a rather low κ -value ($\kappa \sim 9$). Zr and Hf are both from column IV and have similar chemical properties. However, experiments showed that ZrO₂ is not completely stable on a Si substrate. It was found that ZrO₂ can react with Si to form silicide, ZrSi₂ [26, 27]. For this reason, HfO₂ is presently the preferred high- κ oxide over ZrO₂. La₂O₃ has a slightly higher κ than HfO₂, but is more hygroscopic. Y₂O₃ also has a lower κ than La₂O₃. The other lanthanides Ce₂O₃, Pr₂O₃, Nd₂O₃ and Gd₂O₃ have similar properties as La₂O₃.

IA												III A	IV A	V A	VI A	VII A	Noble
	II A																
Li	Be																
	Mg	III B	IV B	V B	VI B	VII B	VIII B		IB	II B		Al	Si				
	Ca	Sc															
	Sr	Y	Zr														
		†	Hf														
		‡															

†	La	Ce	Pr	Nd		Sm	Eu	Gd	Tb	Dy	Ho	Er	Tm	Yb	Lu
‡															

Insufficient thermodynamic data to complete calculations

Experimentally demonstrated

Figure 1.12: Summary of which elements have an oxide that may be thermodynamically stable in contact with silicon at 1000 K. Adapted from Ref. [25].

1.4.3 Interface quality

The interface of the gate dielectric with the Si channel is of particular importance in the gate stack. The carriers induced by the gate are induced within angstroms [1 angstrom (\AA) = 10^{-10} m] of the silicon oxide interfaces. The interface must have the highest electrical quality, in terms of roughness and the absence of interface defects. The interface defects may result in defect charges, which include interface state charges, fixed charges, dielectric-trapped charges and mobile ionic charges [3]. The interface state charges are located close to the Si/SiO₂ interface and have energy states close to the Fermi level (E_F) range of the semiconductor, that is, mainly within the Si energy gap, making them able to exchange charges with the semiconductor in a short time. The fixed charges are located at or very near to the interface but cannot exchange charges. Dielectric trapped charges are located in the bulk dielectric. The mobile ionic charges are mainly contaminations such as sodium ions diffused from the polysilicon gate electrode into the dielectrics. These charges cause flat band voltage shift and hysteresis shift in capacitance–voltage (C–V) measurements, and mobility degradation of current carriers in the channel. The reduction in carrier mobility lowers the saturation current, which is enhanced by the use of high- κ dielectrics. Thus it is clearly desired that the defect density at the interface between high- κ dielectrics and the Si channel be kept as low as possible. It is difficult to imagine that any materials can have a better interface with Si than thermal SiO₂. In modern CMOS processing, for the interface of thermal SiO₂ on Si, the defect charge densities are on the order of 10^{10} cm^{-2} and the midgap interface state densities (D_{it}) are $10^{10} \text{ cm}^{-2}\text{eV}^{-1}$. Most of the high- κ materials proposed show D_{it} values $\sim 10^{11} - 10^{12} \text{ cm}^{-2}\text{eV}^{-1}$. A post-deposition anneal can partly remove various kinds of defects. For example, a low temperature (350–400 °C) anneal in forming gas (typically 90% N₂ : 10% H₂), which is a standard final anneal in the CMOS process, is believed to

passivate interfacial traps (dangling bonds) with hydrogen. The ideal gate dielectric stack may turn out to have an interface comprised of several monolayers of Si—O (and possibly N) containing material, which could be a pseudobinary layer, at the channel interface layer [28].

1.4.4 Film morphology

Polycrystalline gate dielectrics may be problematic because grain boundaries serve as high-leakage paths and dopant diffusion paths [29], and this may lead to the need for an amorphous interfacial layer to reduce leakage current. In addition, grain size and orientation changes throughout a polycrystalline film can cause significant variations in κ , leading to device reliability issues. Single crystal oxides can in principle avoid grain boundaries while providing a good interface. However, the single crystal oxide films may only be obtainable by molecular beam epitaxy (MBE) approaches. A manufacturable scaled CMOS process incorporating MBE methods remains a clear challenge due to the poor throughput relative to the present Si-based fabrication operations. For the above reason, it is desirable to select a material which remains in an amorphous state throughout the necessary CMOS processing treatments. However, most of the advanced gate dielectrics studied to date have a low crystallization temperature (with the exception of Al_2O_3). Thus by using pseudobinary alloys, such as $(\text{ZrO}_2)_x(\text{SiO}_2)_{1-x}$ and $(\text{HfO}_2)_x(\text{SiO}_2)_{1-x}$, it may be possible to combine the desirable properties of two different oxides while eliminating the undesirable properties of each individual material.

1.4.5 Process compatibility

A crucial factor in determining the final film quality and properties is the method by which the dielectrics are deposited in a fabrication process. The deposition process for the dielectric must be compatible with current or expected CMOS processing. A variety of techniques have been employed to deposit high- κ dielectric films. These include physical vapour deposition (PVD) [30–32], metal-organic chemical vapour deposition (MOCVD) [33–35], MBE [36–38] and atomic layer deposition (ALD) [39–42]. PVD is a convenient means to prepare thin films. However, the damage to the substrate induced by the sputtering process makes PVD an unacceptable method to prepare the gate dielectric [28]. It has been found that the surfaces of films deposited by MOCVD were uneven enough to leave some gaps and pockets in which charges could get stuck. MBE can also be excluded for its low throughput. In ALD, films can be deposited one atomic layer at a time, which provides a smooth surface and low defect density. For these reasons, ALD is a preferred process for depositing high- κ gate dielectrics in the future CMOS process [43].

It is expected that Moore's Law can be pushed forward for another decade. While Intel announced that 32 nm technology will go into production by the end of 2009, the technology to further scale CMOS transistors is still being researched. As can be seen from the above discussion, any high- κ candidates must satisfy a set of strict requirements to be used as gate dielectrics. These requirements present a huge challenge for researchers. The objective of this thesis is: (i) to study the atomic layer deposition process for hafnium silicate films using precursors tetrakis(diethylamido)hafnium and tris(2-methyl-2-butoxy)silanol, (ii) to measure the resulting film compositions and structures, and (iii) to explore the possibility of applying hafnium silicate films as the gate insulator.

BIBLIOGRAPHY

- [1] G. E. Moore, *Electronics* **38**, 114 (1965).
- [2] Y. Taur and T. H. Ning, *Fundamentals of Modern VLSI Devices* (Cambridge University Press, 1998).
- [3] T. Hori, *Gate Dielectrics and MOS ULSIs: Principles, Technologies and Applications* (Springer, 1997).
- [4] V. Misra, H. Lazar, Z. Wang, Y. Wu, H. Niimi, G. Lucovsky, J. J. Wortman, and J. R. Hauser, *J. Vac. Sci. Technol. B* **17**, 1836 (1999).
- [5] H. Yang and G. Lucovsky, in *IEDM Tech. Dig.* (1999), p. 245.
- [6] X. Guo and T. P. Ma, *IEEE Electron Device Lett.* **19**, 207 (1998).
- [7] H. R. Huff and D. C. Gilmer, *High Dielectric Constant Materials* (Springer, 2005).
- [8] S. Tang, R. M. Wallace, A. Seabaugh, and D. King-Smith, *Appl. Surf. Sci.* **135**, 137 (1998).
- [9] D. A. Muller, T. Sorsch, S. Moccio, F. H. Baumann, K. Evans-Lutterodt, and G. Timp, *Nature* **399**, 758 (1999).
- [10] J. B. Neaton, D. A. Muller, and N. W. Ashcroft, *Phys. Rev. Lett.* **85**, 1298 (2000).
- [11] H. Wong and H. Iwai, *Microelectron. Eng.* **83**, 1867 (2006).
- [12] H. S. Momose, M. Ono, T. Yoshitomi, T. Ohguro, S. Nakamura, M. Saito, and H. Iwai, *IEEE Trans. Electron Devices* **43**, 1233 (1996).
- [13] G. Timp, A. Agarwal, F. H. Baumann, T. Boone, M. Buonanno, R. Cirelli, V. Donnelly, M. Foad, D. Grant, M. Green, et al., in *IEDM Tech. Dig.* (1997), p. 930.
- [14] G. Timp, J. Bude, K. K. Bourdelle, J. Garno, A. Ghetti, H. Gossmann, M. Green, G. Forsyth, Y. Kim, R. Kleiman, et al., in *IEDM Tech. Dig.* (1999), p. 55.

- [15] T. Ghani, K. Mistry, P. Packan, S. Thompson, M. Stettler, S. Tyagi, and M. Bohr, in *Symp. VLSI Technol.* (2000), p. 174.
- [16] G. Timp, K. K. Bourdelle, J. E. Bower, F. H. Baumann, T. Boone, R. Cirelli, K. Evans-Lutterodt, J. Garino, A. Ghetti, H. Gossmann, et al., in *IEDM Tech. Dig.* (1998), p. 615.
- [17] B. Yu, H. Wang, C. Riccobene, Q. Xiang, and M.-R. Lin, in *Symp. VLSI Technol.* (2000), p. 90.
- [18] B. E. Weir, P. J. Silverman, M. A. Alam, F. Baumann, D. Monroe, A. Ghetti, J. D. Bude, G. L. Timp, A. Hamad, T. M. Oberdick, et al., in *IEDM Tech. Dig.* (1999), p. 437.
- [19] P. A. Packan, *Science* **285**, 2079 (1999).
- [20] J. Robertson, *Rep. Prog. Phys.* **69**, 327 (2006).
- [21] S. M. Sze, *Physics of Semiconductor Devices* (Wiley, New York, 1982).
- [22] J. Robertson, *J. Vac. Sci. Technol. B* **18**, 1785 (2000).
- [23] R. Beyers, *J. Appl. Phys.* **56**, 147 (1984).
- [24] S. Q. Wang and J. W. Mayer, *J. Appl. Phys.* **64**, 4711 (1988).
- [25] K. J. Hubbard and D. G. Schlom, *J. Mater. Res.* **11**, 2757 (1996).
- [26] M. Copel, M. Gribelyuk, and E. Gusev, *Appl. Phys. Lett.* **76**, 4368 (2000).
- [27] M. Gutowski, J. E. Jaffe, C.-L. Liu, M. Stoker, R. I. Hegde, R. S. Rai, and P. J. Tobin, *Appl. Phys. Lett.* **80**, 18979 (2002).
- [28] G. D. Wilk, R. M. Wallace, and J. M. Anthony, *J. Appl. Phys.* **89**, 5243 (2001).
- [29] G. Pant, A. Gnade, M. J. Kim, R. M. Wallace, B. E. Gnade, M. A. Quevedo-Lopez, and P. D. Kirsch, *Appl. Phys. Lett.* **88**, 032901 (2006).
- [30] G. D. Wilk, R. M. Wallace, and J. M. Anthony, *J. Appl. Phys.* **87**, 484 (2000).
- [31] A. Callegari, E. Cartier, M. Gribelyuk, H. F. Okorn-Schmidt, and T. Zabel, *J. Appl. Phys.* **90**, 6466 (2001).
- [32] P. Panchaietch, G. Pant, M. J. Kim, R. M. Wallace, and B. E. Gnade, *J. Vac. Sci. Technol. A* **22**, 395 (2004).
- [33] J. Kim and K. Yong, *J. Cryst. Growth* **263**, 442 (2004).

- [34] Z. M. Rittersma, J. J. G. P. Loo, Y. V. Ponomarev, M. A. Verheijen, M. Kaiser, F. Roozeboom, S. V. Elshocht, and M. Caymax, *J. Electrochem. Soc.* **151**, G870 (2004).
- [35] B. Xia, M. L. Fisher, H. Stemper, and A. Misra, *J. Mater. Res.* **22**, 1024 (2007).
- [36] R. A. McKee, F. J. Walker, and M. F. Chisholm, *Phys. Rev. Lett.* **81**, 3014 (1998).
- [37] J. W. Seo, J. Fompeyrine, A. Guiller, G. Norga, C. Marchiori, H. Siegwart, and J.-P. Locquet, *Appl. Phys. Lett.* **83**, 5211 (2003).
- [38] S. Guha, N. A. Bojarczuk, and V. Narayanan, *Appl. Phys. Lett.* **80**, 766 (2002).
- [39] D. M. Hausmann, E. Kim, J. Becker, and R. G. Gordon, *Chem. Mater.* **14**, 4350 (2002).
- [40] Y. Senzaki, S. Park, H. Chatham, L. Bartholomew, and W. Nieveen, *J. Vac. Sci. Technol. A* **22**, 1175 (2004).
- [41] Y. Xuan, D. Hojo, and T. Yasuda, *Appl. Phys. Lett.* **84**, 5097 (2004).
- [42] R. G. Gordon, J. Becker, D. Hausmann, and S. Suh, *Chem. Mater.* **13**, 2463 (2001).
- [43] M. T. Bohr, R. S. Chau, T. Ghani, and K. Mistry, *IEEE Spectr.* **44**, 29 (2007).

CHAPTER 2

THIN FILM CHARACTERIZATION TECHNIQUES

The film compositions and film structures of Hf silicate thin films grown using the ALD process were characterized by a variety of techniques, specifically spectroscopic ellipsometry (SE), x-ray photoelectron spectroscopy (XPS), medium energy ion scattering (MEIS) and high-resolution transmission electron microscopy (HRTEM). The film deposition processes were monitored by SE. XPS was used to study the chemical states of constituent elements and the elemental composition of the film. The absolute concentrations and depth profiles of Hf in the films were measured by MEIS. Film structures were primarily studied by HRTEM. In this chapter, the principles of these techniques are briefly introduced and the calibration of the MEIS detector is discussed.

2.1 Spectroscopic ellipsometry

Spectroscopic ellipsometry is a very important technique to measure film thickness. It can also be used to analyze multi-layer films and to determine the optical constant dispersion relationship. It is a non-contact, non-destructive technique and can be used to monitor film thickness change during the film deposition process.

The principle of ellipsometric analysis is based on the Fresnel reflection or transmission equation. Figure 2.1 shows a polarized light beam reflecting from a surface. The plane of incidence (POI) is defined as the plane formed by the incident beam and the surface normal. The electric field of the incident or reflected light beam can be decomposed into a p -component (subscript p), E_p , which is in the POI, and a s -component (subscript s), E_s , which is perpendicular to the POI.

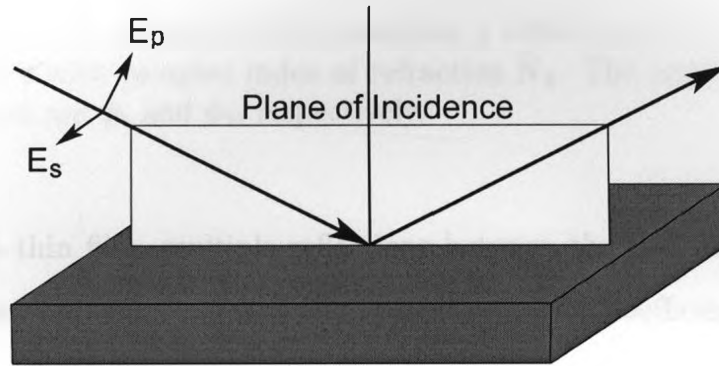


Figure 2.1: Schematic of a light beam reflecting from a surface.

Figure 2.2 shows the schematic of a light beam propagating from medium 1 with a complex index of refraction, \tilde{N}_1 , into medium 2 with a complex index of refraction, \tilde{N}_2 . Reflection and refraction occur at the interface. The angle of reflection is equal to the angle of incidence, i.e., $\phi_r = \phi_i = \phi_1$. If the angle of refraction is ϕ_2 , Snell's law [1] requires

$$\tilde{N}_1 \sin \phi_1 = \tilde{N}_2 \sin \phi_2. \quad (2.1)$$

The Fresnel reflection coefficients, which are the ratios of the outgoing to the incoming electric field magnitudes, are given by [2]

$$\begin{aligned} r_p &= \frac{E_{rp}}{E_{ip}} = \frac{\tilde{N}_2 \cos \phi_1 - \tilde{N}_1 \cos \phi_2}{\tilde{N}_2 \cos \phi_1 + \tilde{N}_1 \cos \phi_2} \\ r_s &= \frac{E_{rs}}{E_{is}} = \frac{\tilde{N}_1 \cos \phi_1 - \tilde{N}_2 \cos \phi_2}{\tilde{N}_1 \cos \phi_1 + \tilde{N}_2 \cos \phi_2}. \end{aligned} \quad (2.2)$$

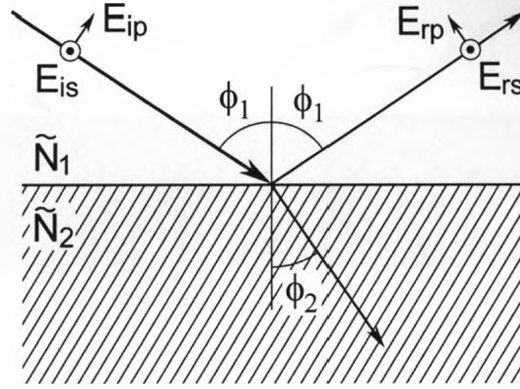


Figure 2.2: A light ray propagates from medium 1 with complex index of refraction \tilde{N}_1 into medium 2 with complex index of refraction \tilde{N}_2 . The angle of reflection and angle of refraction are ϕ_1 and ϕ_2 , respectively.

In the case of a thin film, multiple reflections between the two surfaces of the film have to be considered (Fig. 2.3) and the Fresnel reflection coefficients become [1]

$$\begin{aligned} R_p &= \frac{r_{12p} + r_{23p} \exp(-i2\beta)}{1 + r_{12p}r_{23p} \exp(-i2\beta)} \\ R_s &= \frac{r_{12s} + r_{23s} \exp(-i2\beta)}{1 + r_{12s}r_{23s} \exp(-i2\beta)}, \end{aligned} \quad (2.3)$$

where i is an imaginary number ($i = \sqrt{-1}$); subscripts 12 and 23 denote the Fresnel reflection coefficients at interfaces between media 1 and 2 and media 2 and 3, respectively; and

$$\beta = 2\pi \left(\frac{d}{\lambda} \right) \tilde{N}_2 \cos \phi_2, \quad (2.4)$$

where d is the film thickness and λ is the wavelength of the incident light in the film.

Ellipsometry measures changes in the polarization of the light after reflection, i.e., the phase and amplitude changes of E_s relative to E_p . If we define

$$\rho = \tan(\Psi) \exp(i\Delta) = \frac{R_p}{R_s}, \quad (2.5)$$

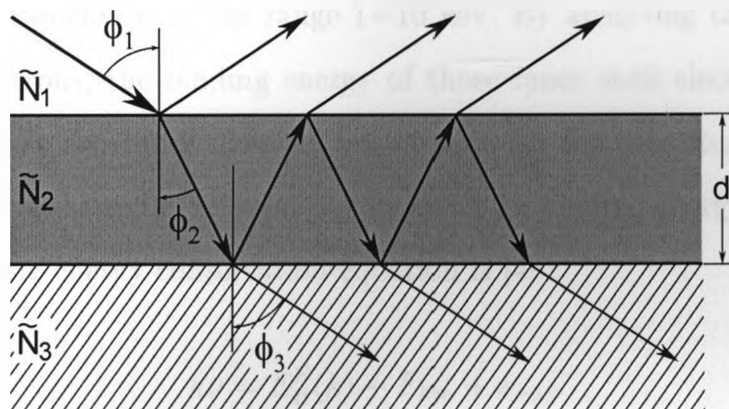


Figure 2.3: Reflections and transmissions of a light ray incident upon a thin film on top of a thick substrate.

where

$$\tan \Psi = \frac{|R_p|}{|R_s|} \quad (2.6)$$

$$\Delta = \Delta_{Rp} - \Delta_{Rs},$$

Ψ and Δ are the quantities measured by ellipsometry. As can be seen from Equations 2.2–2.5, Ψ and Δ are functions of the film thickness and incident light wavelength. In SE, Ψ and Δ are measured as a function of wavelength. The film thickness or index of refraction can then be fitted. The measurement of the change in polarization instead of the absolute light intensity gives ellipsometry greatly enhanced sensitivity [3] such that SE is capable of measuring thickness changes of the order of Å.

2.2 X-ray photoelectron spectroscopy

X-ray photoelectron spectroscopy (XPS), also known as electron spectroscopy for chemical analysis (ESCA), is currently a widely used surface analytical technique. When a solid sample is irradiated with a beam of monoenergetic photons, the inner shell electrons (photoelectrons) may be ejected. The energy of the commonly used x

ray in most instruments is in the range 1–10 keV. By analyzing the kinetic energy of the photoelectrons, the binding energy of those inner shell electrons can be determined, therefore providing chemical information for the constituent atoms in the sample. Figure 2.4 shows the relevant energy levels for binding energy measurements. The corresponding energy conservation equation is [4]

$$h\nu = E_B^F(k) + E_{kin} + \phi_{spec} \quad (2.7)$$

in which $h\nu$ is the energy of the incident x rays, $E_B^F(k)$ is the binding energy referred to the Fermi level, E_{kin} is the kinetic energy of the electrons measured inside the spectrometer analyzer, and ϕ_{spec} is the spectrometer work function.

The binding energy of inner shell electrons in a given element depends on the chemical environment of that element. For example, Fig. 2.5 shows the Si 2p XPS peaks for a 5 nm Hf silicate film on a Si substrate at a photoelectron takeoff angle (θ), which is defined as the angle between the ejected electrons and the sample surface (Fig. 2.6), of 75° (solid line) and 45° (dashed line). The binding energies of the Si 2p electrons from the Hf silicate film and from the Si substrate are separated by ~ 4 eV. For the Si 2p signal from the substrate, the Si 2p_{3/2} and Si 2p_{1/2} peaks can even be resolved by using monochromatic Al $K\alpha$ x rays.

The intensity or area of the photoelectron peaks can be used for quantitative analysis. The probability, P_{pe} , of an incident photon to create a photoelectron in a subshell k can be expressed as [4]

$$P_{pe} = \sigma^k Nt, \quad (2.8)$$

where Nt is the number of atoms/cm² in a layer of thickness t and σ^k is the cross section for ejecting a photoelectron from a given subshell k . If $\theta = 90^\circ$, the number of photoelectrons that can escape from a solid without undergoing an elastic collision

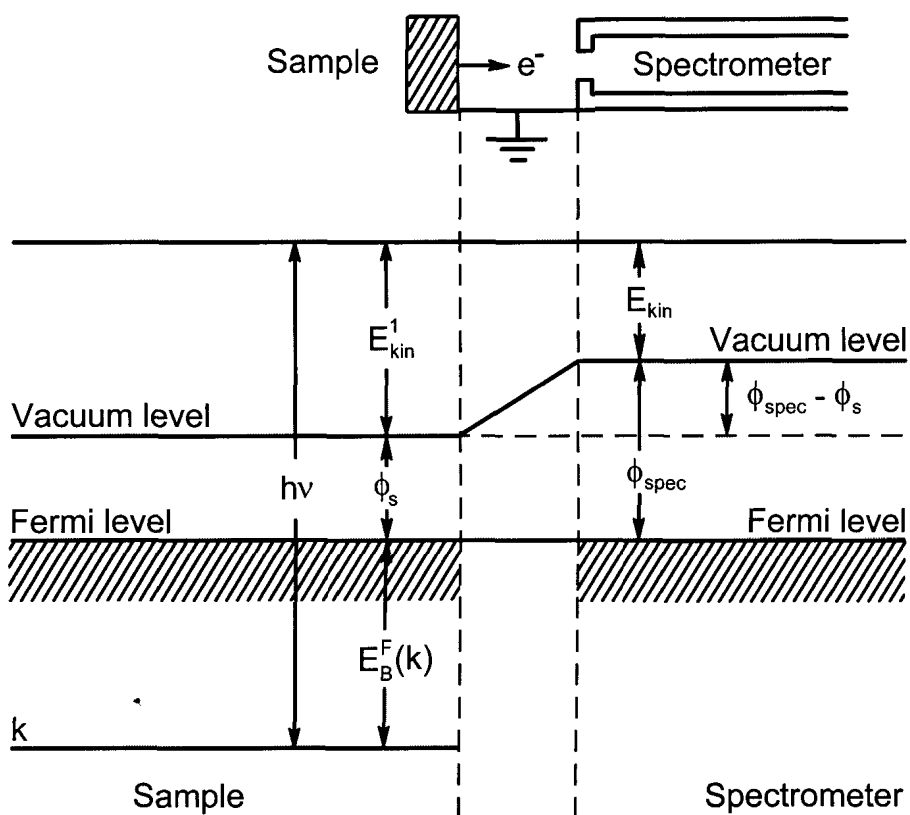


Figure 2.4: Schematic of the relevant energy levels for binding energy measurements. Note that the conducting sample and spectrometer are in electrical contact and thus have common Fermi levels. $h\nu$ is the incident photon energy. E_{kin}^1 is the photoelectron kinetic energy relative to the vacuum level of the sample. The work function difference between the spectrometer and the sample is $\phi_{spec} - \phi_s$. After Ref. [4].

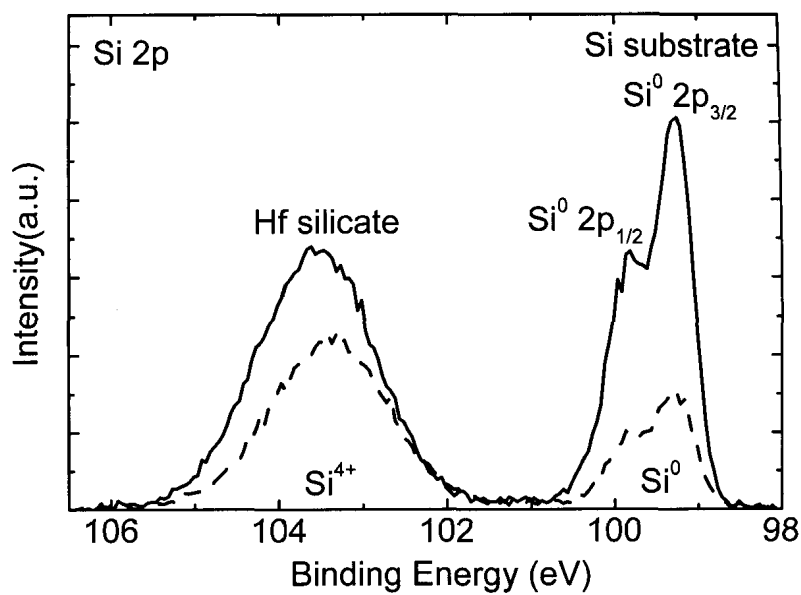


Figure 2.5: Si 2p XPS peaks for a 5 nm Hf silicate film on a Si substrate at photoelectron takeoff angles of 75° (solid line) and 45° (dashed line).

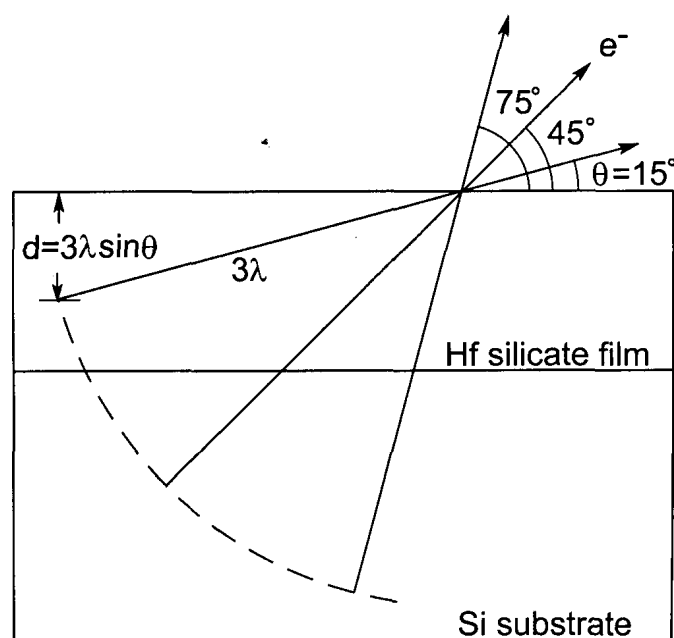


Figure 2.6: Schematic for ARXPS measurements.

decreases with depth d according to $\exp(-d/\lambda)$, where λ is defined as the mean free path for the photoelectrons. Therefore, the probability for an incident photon to create a detectable photoelectron from a subshell k in a thick target is $P_d = \sigma^k N \lambda$ by integrating the $\exp(-t/\lambda)$ function from $t = 0$ to $t = \infty$. Whether a photoelectron contributes to the photoelectron peak in an XPS spectrum also depends on the final state of the atom after ejecting this photoelectron. Only when an atom remains in the ground state configuration with a single vacancy in an inner shell after ejecting a photoelectron does a photoelectron contribute to the photoelectron peak. We use y to denote the efficiency for the production of a photoelectron peak signal for a given atom in a certain chemical environment. Finally, considering the instrumental efficiency T , a photoelectron peak intensity can be expressed as $I \propto n \sigma \lambda y T$, where n is the density of the element of interest in the sample. If we define the sensitivity factor $F = \sigma \lambda y T$, we have $I \propto n F$, and therefore, $n \propto I/F$.

Suppose there are two elements, A and B, in a sample. The relative concentrations of A and B are generally of interest. For example, the relative concentration of A can be calculated from

$$\frac{n_A}{n_A + n_B} = \frac{I_A/F_A}{I_A/F_A + I_B/F_B}. \quad (2.9)$$

In XPS measurements, 95% of the signal intensity comes from a depth of 3λ in the photoelectron emitting direction since the photoelectron intensity is attenuated exponentially with depth. The sampling depth of the sample can be changed by varying θ . This technique is known as angle-resolved XPS (ARXPS). Figure 2.6 shows a schematic for ARXPS measurements. The sampling depth, d , increases as θ increases via the relation $d = 3\lambda \sin \theta$. Therefore, ARXPS can be used to detect a compositional change with film depth. As can be seen from Fig. 2.5, the intensity ratio $I_{Si^{4+}}/I_{Si^0}$ increases as θ decreases, indicating that the contribution to the Si 2p peaks from the substrate is lower at $\theta = 45^\circ$ than at $\theta = 75^\circ$.

2.3 Medium energy ion scattering

Medium energy ion scattering (MEIS) is a high-resolution variant of Rutherford backscattering (RBS). In RBS measurements, a beam of monoenergetic ions (usually MeV ^4He ions) bombards a target. Then elastic scattering, which is governed by the well-known Coulomb repulsion, occurs between the incident ions and the target nuclei. The backscattered ions then enter a detector where they are energy analyzed. The energy value of a backscattered peak provides mass information and thus the identity of the target atoms. The intensity of a peak yields information on the absolute concentration of certain elements in the target. The shape of a backscattered peak can be deconvoluted to extract the depth profile of certain elements in the target.

2.3.1 Kinematics of elastic scattering and identity of the target atom

Here we consider a system of an incident ion with mass M_1 and kinetic energy E_0 and a stationary target atom with mass M_2 ($M_1 < M_2$, see Fig. 2.7). After collision, the kinetic energy of the incident ion is E_1 , and its laboratory scattering angle is θ . The energy of the (recoil) target atom after collision is E_2 . If we apply conservation of energy and conservation of momentum to the system, the following relation is obtained [4]

$$\frac{E_1}{E_0} = \left[\frac{(M_2^2 - M_1^2 \sin^2 \theta)^{1/2} + M_1 \cos \theta}{M_2 + M_1} \right]^2. \quad (2.10)$$

The energy ratio, $E_1/E_0 = k$, is defined as the kinematic factor. Equation 2.10 shows that for a given incident ion, k only depends on the mass of the target atom at a given scattering angle. This is the reason that RBS can be used to detect the identities of the target constituent elements, and even resolve isotopes. Figure 2.8 shows the

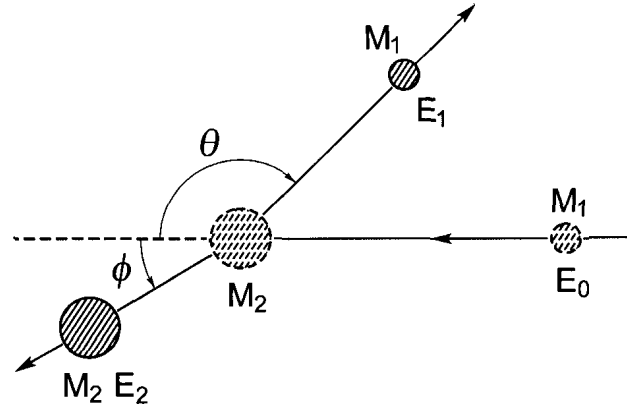


Figure 2.7: Schematic representation of an elastic collision between a projectile of mass M_1 , energy E_0 and a target of mass M_2 which is initially at rest. After collision, the energies of the projectile and the target are E_1 and E_2 , and their (laboratory) scattering angles are θ and ϕ , respectively. After [4].

scattering angle dependence of the kinematic factor for protons incident upon Hf, Si, O and C targets. Note that the scattering of H^+ and H^- incident ions is identical at ~ 100 keV since the electron(s) are stripped in a collision with the surface layer. In the actual MEIS experiments, H^- beam is usually used because of its high beam current. However, the energy of the backscattered ions yield no information about the chemical bonding of the target atoms because the energy of the incident ions in MEIS or RBS experiments varies from hundreds of keV to MeV, while the energy of chemical bonds is of the order of eV.

2.3.2 Rutherford scattering cross section and areal density of target atoms

The Rutherford scattering cross section characterizes the probability of scattering and has a dimension of area. In the center of mass (CM) coordinate frame, the scattering cross section can be expressed as [4]

$$\sigma(\theta_C) = \left(\frac{Z_1 Z_2 e^2}{4E_C} \right)^2 \sin^{-4} \left(\frac{\theta_C}{2} \right), \quad (2.11)$$

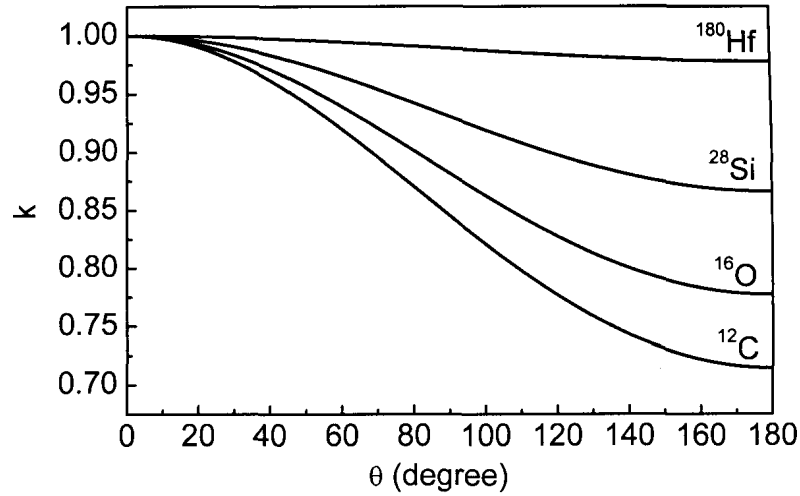


Figure 2.8: Plot of the kinematic factor as a function of scattering angle for protons on Hf, Si, O and C targets.

where θ_C is the CM scattering angle; Z_1 and Z_2 are the atomic numbers of the incident ion and the target atom, respectively; and E_C is the initial energy of the incident ion in the CM coordinates. Transformation to the laboratory frame gives [4]

$$\sigma(\theta) = \left(\frac{Z_1 Z_2 e^2}{2E} \right)^2 \frac{[\cos \theta + (1 - x^2 \sin^2 \theta)^{1/2}]^2}{\sin^4 \theta (1 - x^2 \sin^2 \theta)^{1/2}}, \quad (2.12)$$

where $x = M_1/M_2$ and θ is laboratory scattering angle.

Then, assuming that there is an ideal detector (i.e., the efficiency of the detector is 1), the yield, Y , of the scattered particles is given by

$$Y = Nt\sigma\Omega Q, \quad (2.13)$$

where Nt is the areal density [atoms/m²] of the species of interest, Ω is the solid angle subtended by the detector at the target and Q is the total number of incident particles. N denotes the density of the target atoms in atoms/m³ and t is the thickness. Therefore, if we know the scattering cross section value, by measuring the yield, Y ,

the areal density of the target atoms, Nt , can be determined.

Scattering cross sections can be obtained from Equation 2.12, which is based on the assumption that the interaction between the projectile and the scattering nucleus is a pure Coulomb interaction. However, at small scattering angle or low-energy, heavy ion collisions, the incident particle does not completely penetrate through the electron shells and therefore the innermost electrons screen the charge of the target nucleus. Because of this effect, the Coulomb potential between the projectile and the target nucleus must be modified to account for the screening effect of the innermost electrons.

Of a variety of screened Coulomb potentials [5, 6], the “Universal Potential” developed by Biersack and Ziegler [5] agrees best with the available measurements. For MEIS with primarily light incident ions (H^+ or $^4He^+$), the Molière potential is mostly used [7]. For the positively charged projectile and target nuclei with atomic numbers Z_1 and Z_2 , screened Coulomb potentials have the general form,

$$V(r) = \frac{Z_1 Z_2 e^2}{r} \phi\left(\frac{r}{a}\right), \quad (2.14)$$

where $\phi(r/a)$ is the screening function, and a is the screening length, which is the distance from the nucleus beyond which screening effects become important. In the Molière approximation, the screening function is,

$$\phi(x) = 0.35e^{-0.3x} + 0.55e^{-1.2x} + 0.10e^{-6.0x}. \quad (2.15)$$

For the purpose of MEIS, the commonly used screening length is,

$$a = \frac{0.8853a_0}{(\sqrt{Z_1} + \sqrt{Z_2})^{2/3}}, \quad (2.16)$$

where $a_0 = 0.529 \text{ \AA}$ is the Bohr radius.

Effectively, electron screening has the same effect as a slight increase in the incident ion energy. One can therefore assume an effective kinetic energy increase V_1 in Rutherford scattering [8]. The relationship between the corrected cross section (σ) and the Rutherford value (σ_R) can be expressed as [8],

$$\frac{\sigma}{\sigma_R} = \frac{1}{1 + \frac{V_1}{E}}. \quad (2.17)$$

where V_1 is estimated to be the decrease in potential energy caused by electron screening, which can be approximated by the first term of the Taylor expansion of Equation 2.14:

$$V_1 = \frac{Z_1 Z_2 e^2}{a} |\phi'(0)|. \quad (2.18)$$

2.3.3 Energy loss of incident ions and backscattering depth profile

As the light ions, such as H^+ and $^4He^+$, travel through the solid sample, they lose energy due to excitation and ionization in inelastic collisions with target atoms. This energy loss is called “electronic-energy loss”, which gives the MEIS technique the ability to extract depth profiles of the target constituent atoms. Microscopically, the “electronic-energy loss” is a discrete process. However, it is a good approximation to assume that the moving ions lose energy continuously in solid media.

Figure 2.9 shows the schematic of the path of a projectile in a target. The angle between the incident direction of the ion and the sample normal is θ_1 . θ is the lab scattering angle and $\theta_2 = 180^\circ - \theta_1 - \theta$ is the angle between the sample normal and the scattered direction. We use $S(E) = dE/dx$ to denote the energy loss per unit distance as the ion travels in the target. The energy loss of the incident ion on the

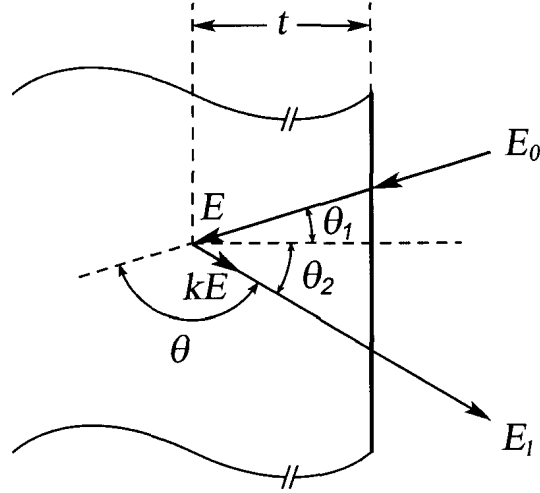


Figure 2.9: Travelling path of an incident ion in the target. The target normal is tilted θ_1 degree from the incident ion beam. As an incident ion with initial energy E_0 travels a distance $t/\cos\theta_1$ in the target, its energy reduces to E . Then the incident ion loses energy $(1-k)E$ during the subsequent elastic scattering. θ is the lab scattering angle. The scattered ion then loses a certain amount of energy on its way out of the target with its final detected energy E_1 . After Ref. [4].

inward path is $\Delta E_{in} = S_{in}(E)t/\cos\theta_1$, such that the ion energy after reaching depth t is $E = E_0 - \Delta E_{in}$. After elastic scattering, the energy of the scattered ion is kE (k is the kinematic factor). On the way out of the target, the scattered ion again experiences an energy loss, which is $\Delta E_{out} = S_{out}(E)t/\cos\theta_2$. Therefore, we have the following equation

$$E_1 = kE - \Delta E_{out} = kE_0 - t \left[\frac{kS_{in}(E)}{\cos\theta_1} + \frac{S_{out}(E)}{\cos\theta_2} \right]. \quad (2.19)$$

As can be seen, the energy of the scattered ion which escapes from the target surface depends on the depth where the elastic scattering occurred. By performing a computer simulation, the depth profile of the target atoms can be extracted from the measured scattered ion energy distribution.

2.3.4 Toroidal electrostatic analyzer

In order to achieve high resolution, a toroidal electrostatic analyzer (TEA) is used to analyze the backscattered ions in MEIS. Figure 2.10 shows the schematic of a TEA system. The trajectories of the scattered ions are bent by the TEA such that the scattered ions hit the microchannel plates, where secondary electrons are produced. These signals are then amplified to give charge clouds which exit the microchannel plates and impinge on the position sensitive detector (PSD), where they are energy and angle analyzed [9].

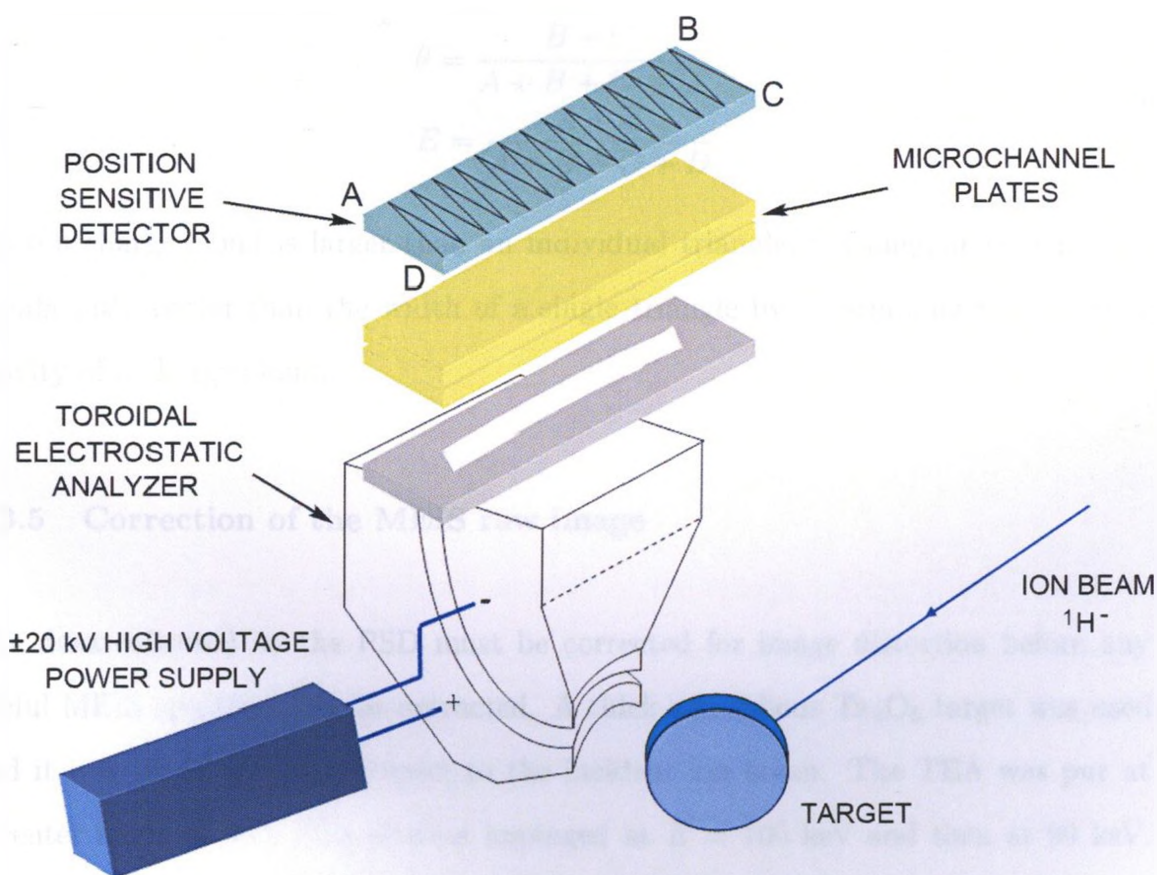


Figure 2.10: Schematic of the toroidal electrostatic analyzer system.

The PSD is a charge dividing collector shown schematically in Fig. 2.11. The charge dividing collector consists of two sets of triangular electrodes, one set pointing toward

the center and the other set pointing away. The two sets of electrodes are electrically isolated from one another. Neighbouring triangles in each set are coupled with a capacitor and a resistor. The two extreme triangles in each set are connected to charge sensitive preamplifiers. An electron cloud impinging from the microchannel plates on this set of electrodes will spread along the capacitor chains to the charge sensitive preamplifiers. The coordinates of the impinging position of the electrode cloud, and therefore the scattering angle and the energy of the scattered ion, are determined by the relative signal strength at the charge sensitive preamplifiers (denoted by A , B , C and D) [10, 11], as shown in the following Equations:

$$\begin{aligned}\theta &= \frac{B + C}{A + B + C + D} \\ E &= \frac{A + B}{A + B + C + D}.\end{aligned}\tag{2.20}$$

Since a charge cloud is larger than an individual triangle, the angular resolution is significantly better than the width of a single triangle by determining the center of gravity of a charge cloud.

2.3.5 Correction of the MEIS raw image

The data collected by the PSD must be corrected for image distortion before any useful MEIS spectrum can be extracted. A thick amorphous Ta_2O_5 target was used and it was tilted 45° with respect to the incident ion beam. The TEA was put at a center angle of 90° . The protons impinged at $E = 100$ keV and then at 99 keV. Thus, the protons were scattered with the energy kE , where the kinematic factor k is a function of scattering angle. The TEA voltage setting was chosen (96.1 keV) such that the Ta edge was contained in both raw data sets. Assuming there is no distortion along the angle direction, the angle data were compressed by a factor of 4.

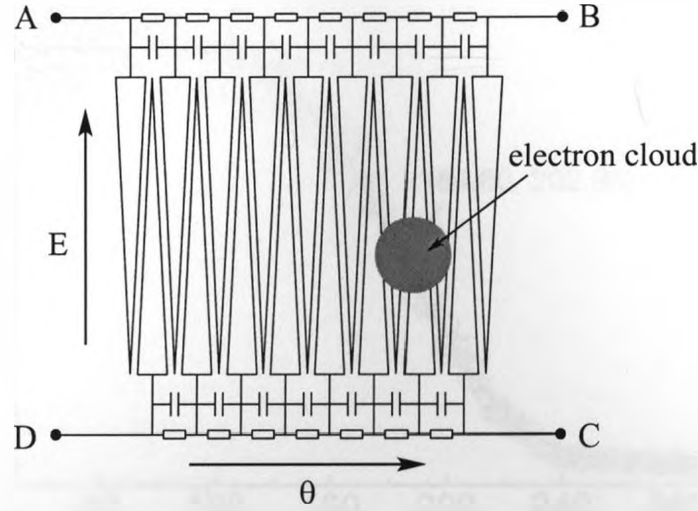


Figure 2.11: Schematic of the charge dividing collector. The electron cloud produced by the scattered ion impinging on the microchannel plates is analyzed. The charge is drained to four charge sensitive amplifiers A, B, C and D. The angle and energy of the scattered ion are determined by the relative values of the charges collected by amplifiers A, B, C and D.

In order to find the Ta edge, the RBS spectrum at each scattering angle channel was fitted with the equation

$$y = \frac{\lambda_1}{2} \left[1 + \operatorname{erf} \left(\frac{\lambda_2 - x}{\sqrt{2}\lambda_3} \right) \right] + \lambda_4, \quad (2.21)$$

where y is counts, x is the channel number in the energy direction and λ_1 , λ_2 , λ_3 and λ_4 are the fitting parameters. λ_2 is the channel number which corresponds to the half-height point and therefore defined as the Ta edge. In Equation 2.21, $\operatorname{erf}(x)$ is the error function which is defined as

$$\operatorname{erf}(x) = \frac{2}{\sqrt{\pi}} \int_0^x e^{-t^2} dt. \quad (2.22)$$

Figure 2.12 shows the fitting curve for the Ta edge corresponding to 100 keV incident protons at angle channel 120.

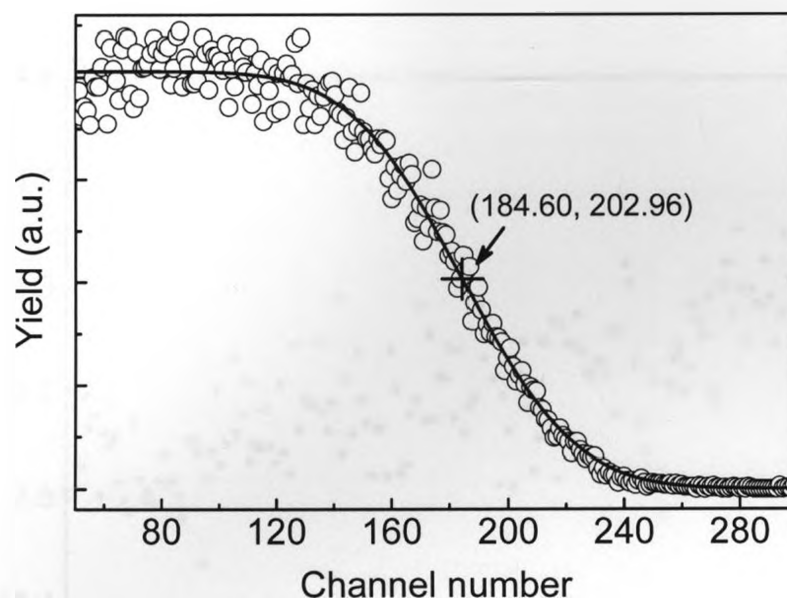


Figure 2.12: Ta edge for 100 keV incident protons at angle channel 120 fitted by an error function. The coordinates of the half-height point are shown.

Using linear interpolation of the data in the energy direction, one finds the derivative dE/dC (C is channel number) [eV/channel] for each angular position which is given by $1000k/(C_1 - C_2)$, where C_1 and C_2 are the channel numbers of the Ta edges for 100 keV and 99 keV incident protons, respectively. Figure 2.13 shows dE/dC values from channel 20 to 180. The constant energy position, which corresponds to 98.4 keV (the average energy of 100 keV and 99 keV protons scattered from Ta at scattering angle 90°) for each angle channel, is shown in Fig. 2.14.

2.3.6 TEA dead time measurement

When the TEA is set up to detect ions scattered from heavy elements, such as Hf, Ta and Au, the PSD count rate is high because of the large scattering cross sections for these heavy elements. It is important to run the PSD in a count rate range where the counting rate loss is insignificant. In order to calculate the detector dead time, count rates of protons scattered from Ta_2O_5 in the energy range 90–95 keV were measured

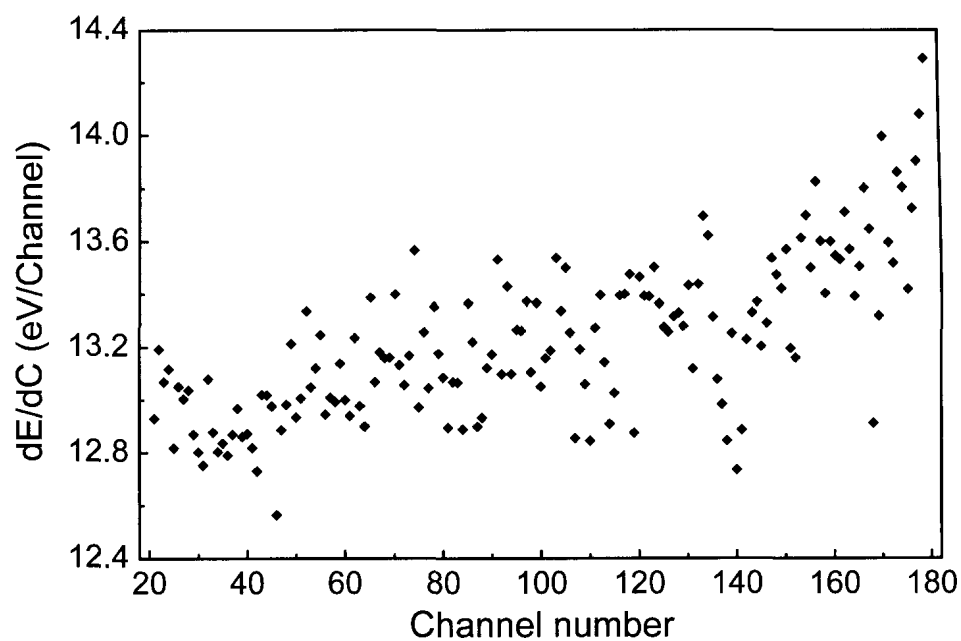


Figure 2.13: dE/dC for each angular position of the PSD.

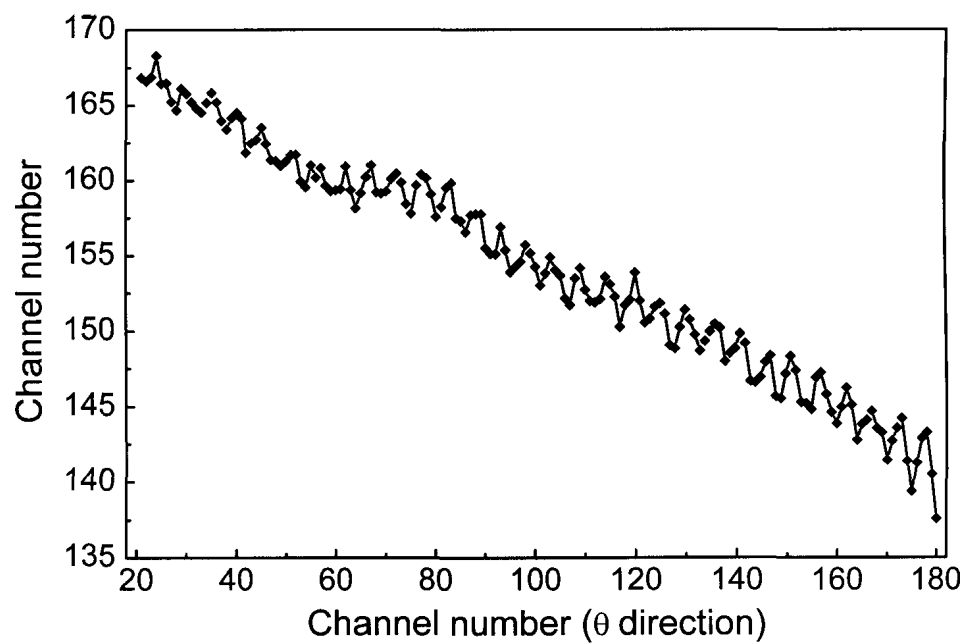


Figure 2.14: Channel position corresponding to 98.4 keV scattered protons for a TEA setting of 96.1 keV for each angular channel.

at different ion beam currents and the data are listed in Table 2.1.

Table 2.1: PSD output count rate for protons scattered from Ta_2O_5 in the energy range 95–99 keV for different ion beam current intensities.

Average beam current (nA)	TEA energy (keV)	Dose (μC)	Counts	Run time (s)	Output count rate (kHz)
47.17	95	3	1061159	60	17.686
	96	3	1066245	56	19.040
	97	3	848515	62	13.686
	98	3	392597	78	5.033
	99	3	21700	62	0.350
27.37	95	3	1205340	108	11.161
	96	3	1179506	104	11.341
	97	3	910234	112	8.128
	98	3	408617	112	3.648
	99	3	24574	112	0.219
13.86	95	3	1251687	218	5.742
	96	3	1231635	204	6.037
	97	3	972534	220	4.421
	98	3	452548	214	2.115
	99	3	34870	226	0.154
7.00	95	1.5	654366	214	3.058
	96	1.5	647024	214	3.023
	97	1.5	496556	210	2.365
	98	1.5	227928	214	1.065
	99	1.5	17496	220	0.080
3.42	95	0.75	335617	254	1.321
	96	0.75	329423	226	1.458
	97	0.75	258220	240	1.076
	98	0.75	112674	236	0.477
	99	0.75	7261	140	0.052

A reasonable assumption is that there are no count losses at low ion beam currents, i.e., at low count rates. The lowest beam current in this experiment is 3.42 nA. If we assume that there is no counting loss at a beam current of 3.42 nA and define m = the measured output count rate and n = true input count rate, then the ratio of m/n is equal to the ratio of measured total counts per unit dose of incident protons/measured total counts per unit dose of incident protons at the beam current

of 3.42 nm. Therefore the input count rates can be calculated from the measured output count rates and the results are shown in Fig. 2.15.

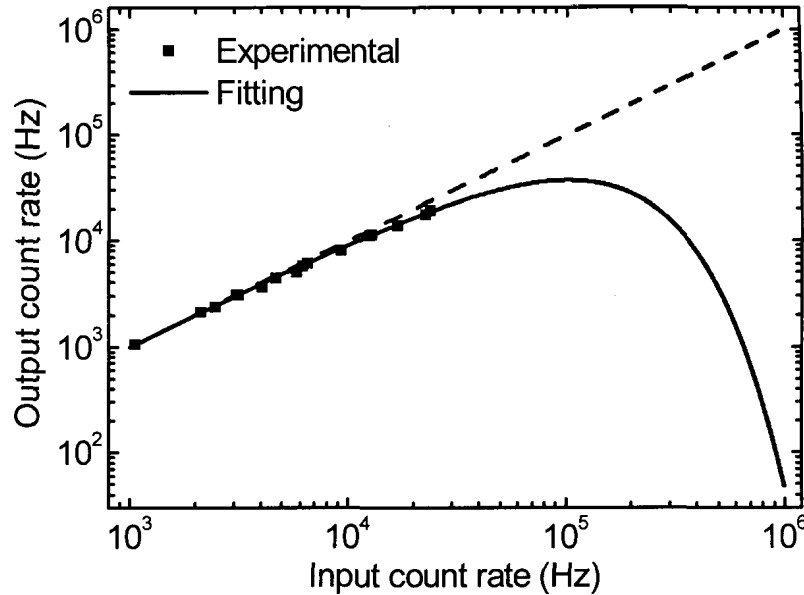


Figure 2.15: Output count rate versus input count rate for the TEA. The solid curve is a fit to a paralyzable model. The dashed line shows the simulation where the output count rate is equal to the input count rate.

There are two idealized models, paralyzable and non-paralyzable responses, which describe the dead time behaviour of counting systems [12]. The fundamental assumptions of the two models are shown in Fig. 2.16. Considering six randomly spaced events on the time scale, the dead time following each event is τ . In the paralyzable model, an event that occurs during the dead period is not counted but extends the dead time by another period τ following the lost event. In the example shown, only three counts are recorded for the six true events. In the non-paralyzable model, true events that occur during the dead period do not have any effect on the behaviour of the detector. Therefore the non-paralyzable detector would record four events for the six true events. The PSD (Quantar 2601B) used in the MEIS system at UWO is a paralyzable detector, for which the relationship between m and n is

described by the following Equation [12]:

$$m = ne^{-n\tau}. \quad (2.23)$$

Fitting the experimental data shown in Fig. 2.15 yields $\tau = 9.9 \mu\text{s}$, which is in very good agreement with the $10 \mu\text{s}$ dead time given by Quantar Technology for a 10-bit detector that we have at UWO.

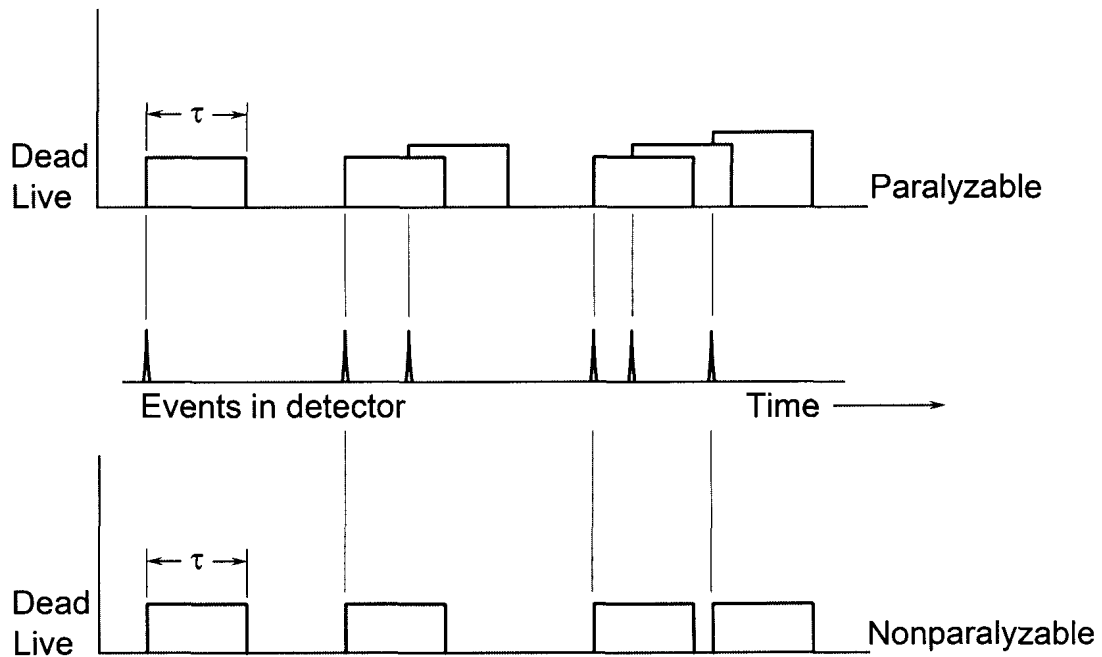


Figure 2.16: Illustration of two idealized models of dead time behaviour for radiation detectors. After Ref. [12].

2.3.7 MEIS measurement geometry and an example of a MEIS spectrum

In MEIS measurements, a double alignment geometry (i.e., channelling in and blocking out, Fig. 2.17) was used to reduce the flux of ions scattered from the substrate atoms. Figure 2.18 shows the 2-dimensional spectrum of a $\sim 4 \text{ nm}$ Hf silicate film on Si(100) substrate aligned in the geometry shown in Fig. 2.17. The incident ions

are 95 keV $^1\text{H}^-$. Note in the blocking direction, the background is greatly reduced. Figure 2.19 shows the energy versus angle spectrum at a scattering angle of 90° .

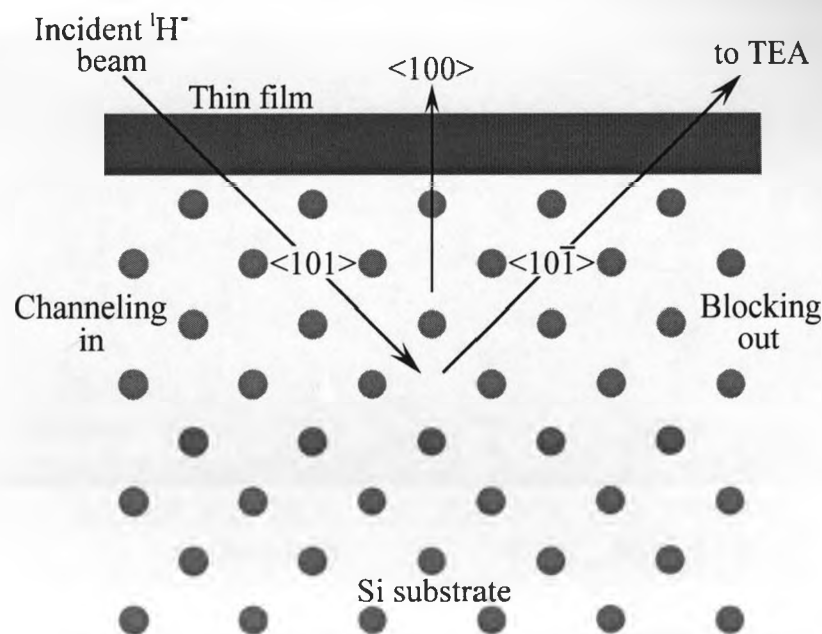


Figure 2.17: Schematic of MEIS measurement geometry. Thin films were grown on a Si(100) substrate. The incident beam was aligned to the $\langle 101 \rangle$ direction and the scattered ions towards the $\langle 10\bar{1} \rangle$ direction were detected by the TEA.

2.4 Transmission electron microscopy

Transmission electron microscopy (TEM) is a very important technique to study crystalline structure and morphology of materials. It works on the same basic principle as optical microscopy. The resolution of an optical microscope is limited by the wavelength of visible light, namely ~ 500 nm. In contrast, the electrons accelerated to 200 kV have a relativistic wavelength of 0.00251 nm, and thus allow us to “see” structures much smaller than for the case of visible light. In TEM, electromagnetic lenses are used to deflect electrons that interact with a specimen to form diffraction patterns or images. The specimen has to be thin enough (tens of nanometers) to allow electrons

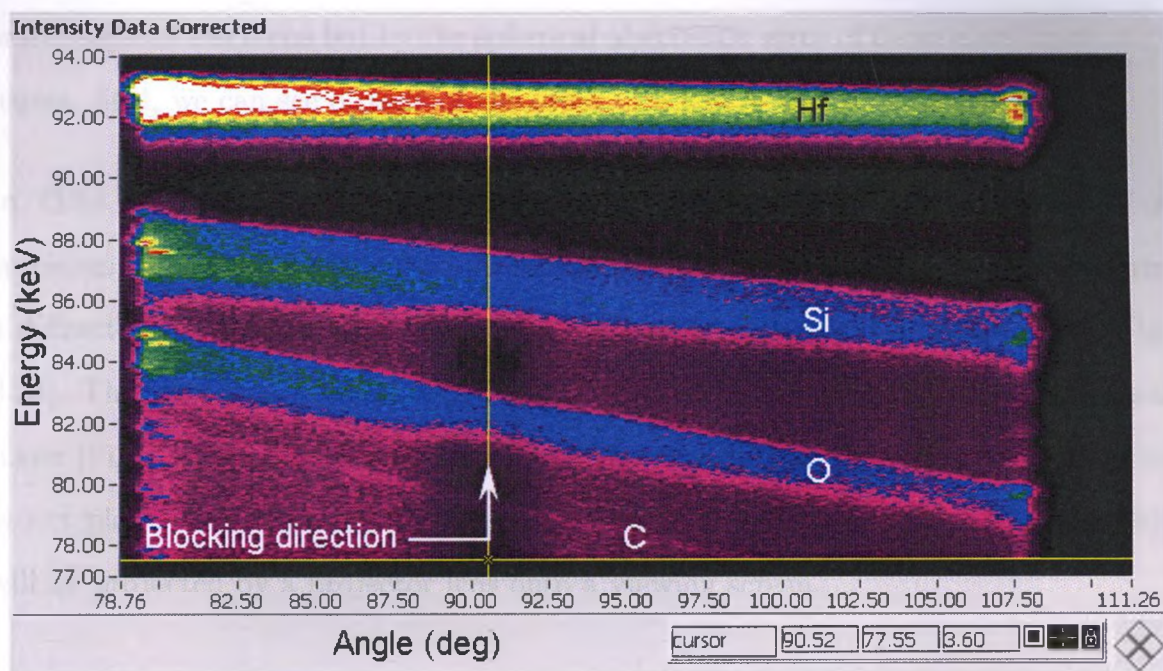


Figure 2.18: A 2-dimensional spectrum for a 4 nm Hf silicate film grown on Si(100). The incident beam is 95 keV $^1\text{H}^-$ ions and the sample is aligned in the geometry shown in Fig. 2.17.

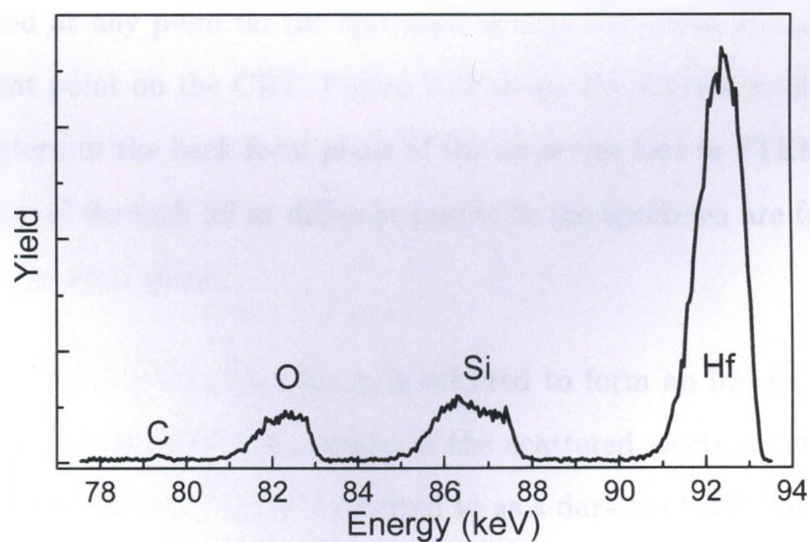


Figure 2.19: The RBS spectrum taken from Fig. 2.18 at scattering angle 90° .

to be transmitted through the sample. The resolution of TEM is not limited by the wavelength of electrons but by the spherical aberration error of those electromagnetic lenses. Still, we can see objects of the order of a few Å in size with TEM.

In TEM mode, a beam of monochromatic, coherent electrons are projected onto a specimen. The transmitted electrons are then dispersed by the objective lens to form a diffraction pattern in the back focal plane and an image in the image plane (Fig. 2.20). The focal length of the intermediate lens can be adjusted to use the back focal plane [Fig. 2.20(a)] or the image plane [Fig. 2.20(b)] of the objective lens as its object plane. Therefore the diffraction pattern [Fig. 2.20(a)] or image [Fig. 2.20(b)] will be projected by a projector lens onto a viewing screen.

In scanning transmission electron spectroscopy (STEM) mode, a convergent beam is used to scan the specimen. The translation of the electron beam onto the sample is realized by the use of scanning coils; these same coils are used to scan the cathode-ray tube (CRT) synchronously. The electron detector acts as the interface between the electrons coming from the specimen and the image viewed on the CRT. The STEM signal generated at any point on the specimen is recorded, amplified, and displayed at an equivalent point on the CRT. Figure 2.21 shows the schematic of a stationary diffraction pattern in the back focal plane of the objective lens in STEM mode. The electrons scattered through 2θ at different points in the specimen are focused at the same point in the focal plane.

In TEM, if the direct transmitted beam is selected to form an image, the resultant image is called a bright field (BF) image; if the scattered electrons other than the direct beam are selected, the image is referred to as a dark field (DF) image. To form a DF STEM image, an annular detector, which surrounds the BF detector, is usually used. To avoid Bragg scattering [13], electrons scattered through a semi-angle of $>50^\circ$

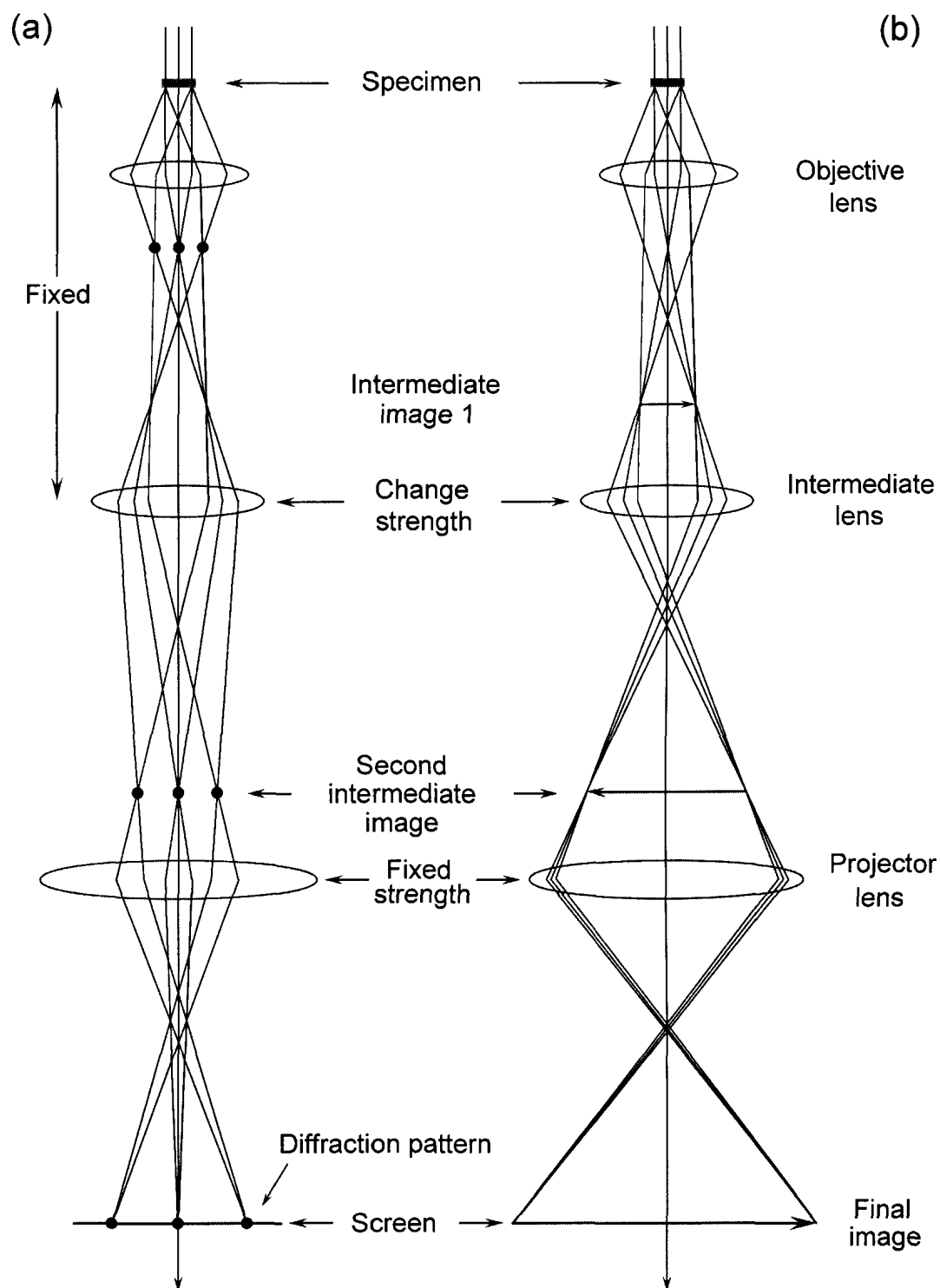


Figure 2.20: Schematic ray path for the two basic operations of a TEM imaging system: (a) projecting the diffraction pattern on the viewing screen and (b) projecting the image onto the viewing screen. After Ref. [13].

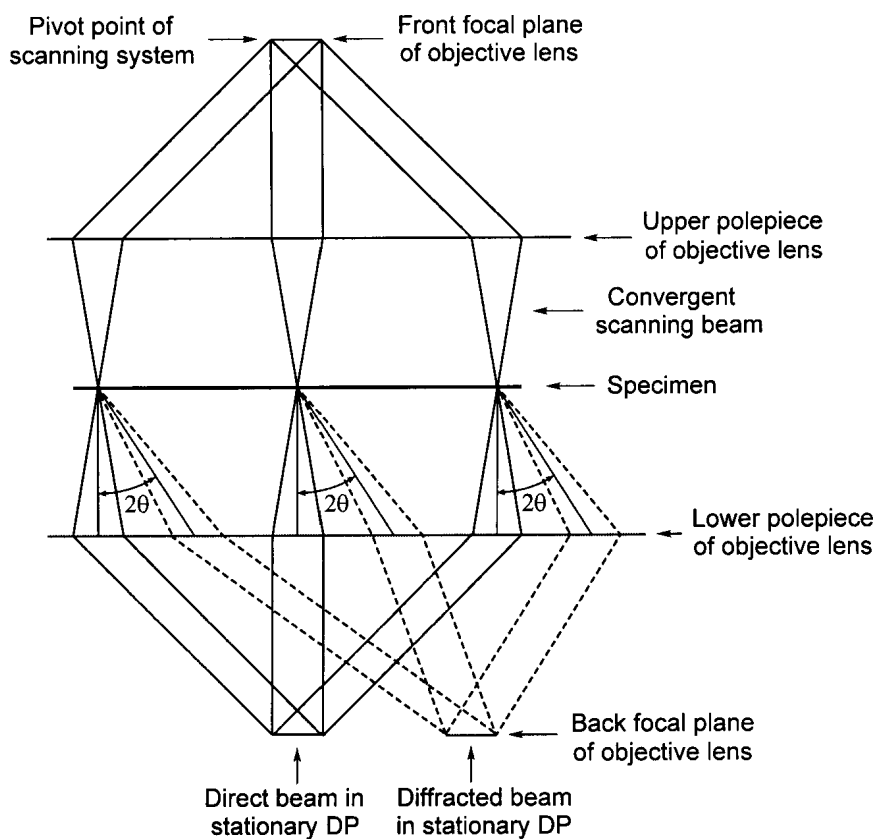


Figure 2.21: The creation of a stationary diffraction pattern in the back focal plane of the objective lens in STEM imaging. After Ref. [13].

mrads are collected by the so-called high-angle annular dark field (HAADF) detector (Fig. 2.22). The image contrast then depends on the average atomic number, Z , of the specimen, and thus the resultant image is referred to as a Z -contrast image.

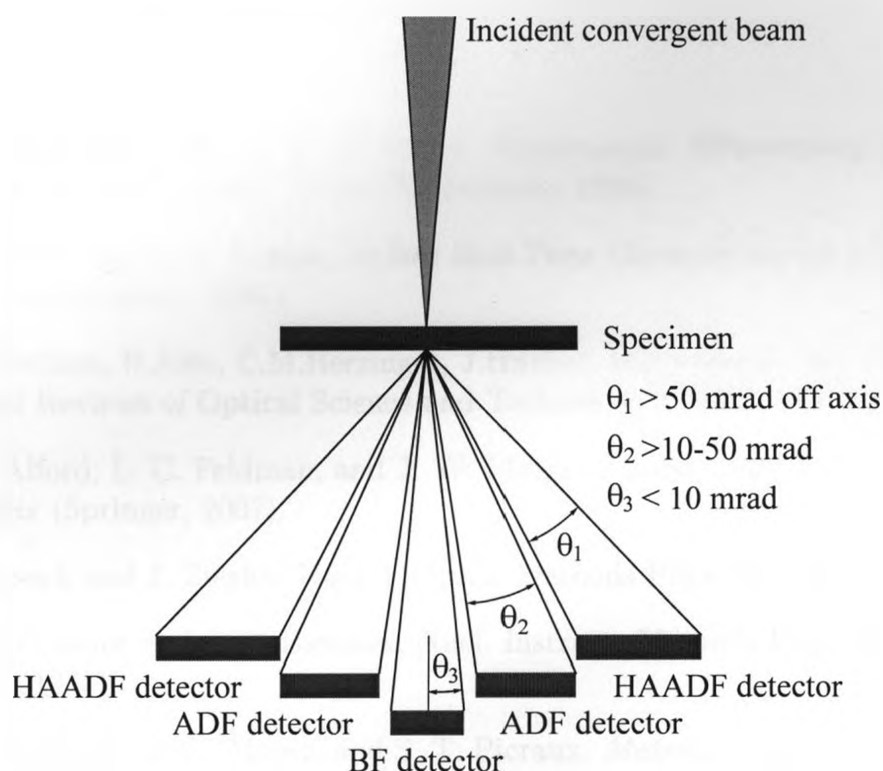


Figure 2.22: Schematic of the HAADF detector setup in a STEM. After Ref. [13].

In this thesis, to investigate the Hf depth profiles in both the as-grown and annealed films, $\langle 011 \rangle$ cross-sectional TEM samples were prepared using standard dimpling and ion milling procedures and characterized by high resolution TEM (HRTEM) and high angle annular dark field scanning transmission electron microscopy (HAADF-STEM) in a JEOL JEM-2100F TEM operating at 200 kV. The HRTEM and HAADF-STEM images are referred to as bright field (BF) and dark field (DF) images, respectively.

BIBLIOGRAPHY

- [1] H. G. Tompkins and W. A. McGahan, *Spectroscopic Ellipsometry and Reflectometry: A User's Guide* (Wiley-Interscience, 1999).
- [2] O. Auciello and A. R. Krauss, *In Situ Real-Time Characterization of Thin Films* (Wiley-Interscience, 2001).
- [3] J.A.Woollam, B.Johs, C.M.Herzinger, J.Hilfiker, R.Synowicki, and C.L.Bungay, Critical Reviews of Optical Science and Technology **CR72**, 1 (1999).
- [4] T. L. Alford, L. C. Feldman, and J. W. Mayer, *Fundamentals of Nanoscale Film Analysis* (Springer, 2007).
- [5] J. Biersack and J. Ziegler, Nucl. Instrum. Methods Phys. Res. **194**, 93 (1982).
- [6] D. J. O'connor and J. P. Biersack, Nucl. Instrum. Methods Phys. Res., Sect. B **15**, 14 (1986).
- [7] L. C. Feldman, J. W. Mayer, and S. T. Picraux, *Materials analysis by ion channeling : submicron crystallography* (Academic Press, New York, Toronto, 1982).
- [8] H. H. Andersen, F. Besenbacher, P. Loftager, and W. Möller, Phys. Rev. A **21**, 1891 (1980).
- [9] R. M. Tromp, M. Copel, M. C. Reuter, M. H. von Hoegen, J. Speidell, and R. Koudijs, Rev. Sci. Instrum. **62**, 2679 (1991).
- [10] R. W. van Resandt, H. den Harick, and J. Los, J. Phys. E **9**, 503 (1976).
- [11] R. Allemand and G. Thomas, Nucl. Instr. and Meth. **137**, 141 (1976).
- [12] G. F. Knoll, *Radiation detection and measurement* (Wiley, 1989).
- [13] D. B. Williams and C. B. Carter, *Transmission Electron Microscopy: A Textbook for Materials Science* (Springer, 1996).

CHAPTER 3

ATOMIC LAYER DEPOSITION OF Hf SILICATE FILMS¹

3.1 Atomic layer deposition

Atomic layer deposition (ALD) is a method for producing thin films one atomic layer at a time utilizing a self-control obtained through saturating surface reactions [1]. In ALD, films deposited on the substrate surface are strictly controlled by the self-saturation mechanism of the reaction between the gaseous precursor and the surface. Saturation of a surface reaction into a monolayer (ML) formation occurs when all available bonding sites on the surface are occupied and the surface species formed in the reaction do not produce new bonding sites for the precursor used. For the next saturated reaction the surface is exposed to a different precursor or is treated somehow in order to recreate the necessary bonding sites. Therefore, an ALD growth cycle can usually be divided into four steps:

1. exposure of the substrate surface to the pulse of the first precursor;
2. inert gas purge to remove the reaction by-products and unreacted precursor;

¹A version of this chapter has been published in a journal article. J. Liu, W. N. Lennard, L. V. Goncharova, D. Landheer, X. Wu, S. A. Rushworth, and A. C. Jones, *J. Electrochem. Soc.* **156**, G89 (2009)

3. introduction of the second precursor to react with the surface prepared by the first precursor to produce a thin film with desired composition;
4. inert gas purge.

It should be noted that only in the ideal case can a monolayer growth per cycle be realized. In practice, the growth rate can be only a fraction of monolayer due to the steric hindrance of the precursor ligands [2]. The temperature range within which the film growth proceeds in a self-controlled manner is called “ALD-window” [3, 4], which is shown in Fig. 3.1. Outside of the ALD-window, the growth is limited by precursor condensation, decomposition, and desorption or by insufficient reactivity. The self-limiting ALD mechanism is corroborated by the fact that the growth rate does not depend on the precursor pulse length provided the surface is saturated, i.e., all available surface sites are occupied by adsorbed precursor molecules.

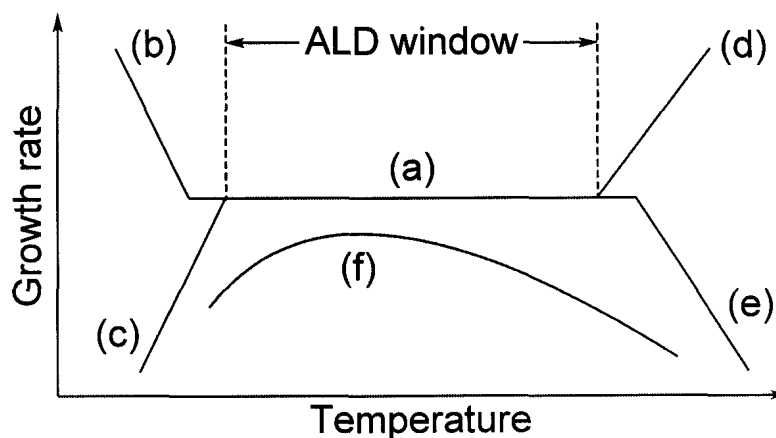


Figure 3.1: Scheme of (a) an ALD window limited by (b) precursor condensation, (c) insufficient reactivity, (d) precursor decomposition and (e) precursor desorption. If the decomposition rate is dependent on the number of available reactive sites as in (f), actual ALD window cannot be observed. After ref [5].

Because of the self-limiting reaction mechanism of ALD, its major advantages include:

1. accurate thickness control (within fraction of a monolayer);

2. large area uniformity;
3. excellent conformality;
4. low deposition temperature.

However, there are also some limiting factors in the application of ALD to film deposition, which include:

1. low growth rate;
2. limited available precursors for some elements.

In order to grow high quality thin films by ALD, there are some requirements for the precursors involved:

1. sufficient volatility at the deposition temperature;
2. do not decompose at the deposition temperature;
3. sufficient reactivity with the other precursor;
4. do not react with the film formed on the substrate surface;
5. reasonable price;
6. safe handling and preferably non-toxicity.

3.2 Precursor consideration

The most widely used Hf precursor for ALD is hafnium tetrachloride, HfCl_4 [6–11]. However, using HfCl_4 as Hf precursor in ALD has several disadvantages: (i) HfCl_4 is a

solid at room temperature and its vapour pressure is low ($\sim 1.57 \times 10^{-5}$ torr at 40°C); (ii) Cl impurities are often found in the resultant films [12]; (iii) corrosive halide byproducts can be detrimental both to the film and to the deposition equipment. Gordon *et al.* [13, 14] and Kukli *et al.* [15] have introduced the possibility of using Hf alkylamides, i.e., tetrakis(dimethylamido)hafnium ($\text{Hf}[\text{N}(\text{CH}_3)_2]_4$), tetrakis(ethylmethylamido)hafnium ($\text{Hf}[\text{N}(\text{C}_2\text{H}_5)(\text{CH}_3)]_4$) and tetrakis(diethylamido)hafnium ($\text{Hf}[\text{N}(\text{C}_2\text{H}_5)_2]_4$), as precursors for HfO_2 thin film ALD deposition. Metal amides should be more reactive toward a hydroxylated surface than metal halides because the metal-nitrogen bond is significantly weaker than the metal-halide bond which is weaker than the metal-oxygen bond [14]. A variety of Si precursors, e.g., silicon tetrachloride (SiCl_4) [16], tetrakis(ethylmethylamido)silicon ($\text{Si}[\text{N}(\text{C}_2\text{H}_5)(\text{CH}_3)]_4$) [17], tetra-*n*-butyl orthosilicate $[\text{Si}(\text{O}^n\text{Bu})_4]$ [18], $\text{SiH}[\text{N}(\text{CH}_3)_2]_3$ [19], etc., have been investigated for ALD of Hf silicate films. When using these Si precursors in combination with HfCl_4 or Hf alkylamides, additional oxygen sources, usually H_2O or O_3 , have to be used to provide oxygen. As a result a detectable amount of SiO_2 has been often found at the dielectric/Si interface upon completion of the film growth [16, 17]. Gordon *et al.* [13] investigated tris(tert-butoxy)silanol as both Si precursor and oxygen source in ALD growth of Hf silicate films and found excellent properties of the resulting films which include smooth surface, abrupt interface with the Si substrate and low carbon impurity concentration. In this work, tetrakis(diethylamido)hafnium (TDEAH) is used as Hf precursor while tris(2-methyl-2-butoxy)silanol (TMBS), $[\text{CH}_3\text{CH}_2\text{C}(\text{CH}_3)_2\text{O}]_3\text{SiOH}$, is used both as an oxygen source and a Si precursor. The schematic molecular structures and vapour pressures as a function of temperature for TDEAH and TMBS are shown in Figs. 3.2 and 3.3, respectively.

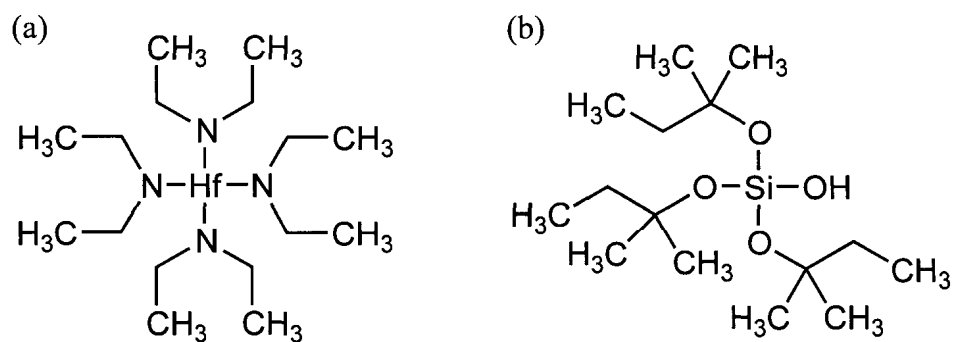


Figure 3.2: Schematic molecular structures of (a) TDEAH and (b) TMBS.

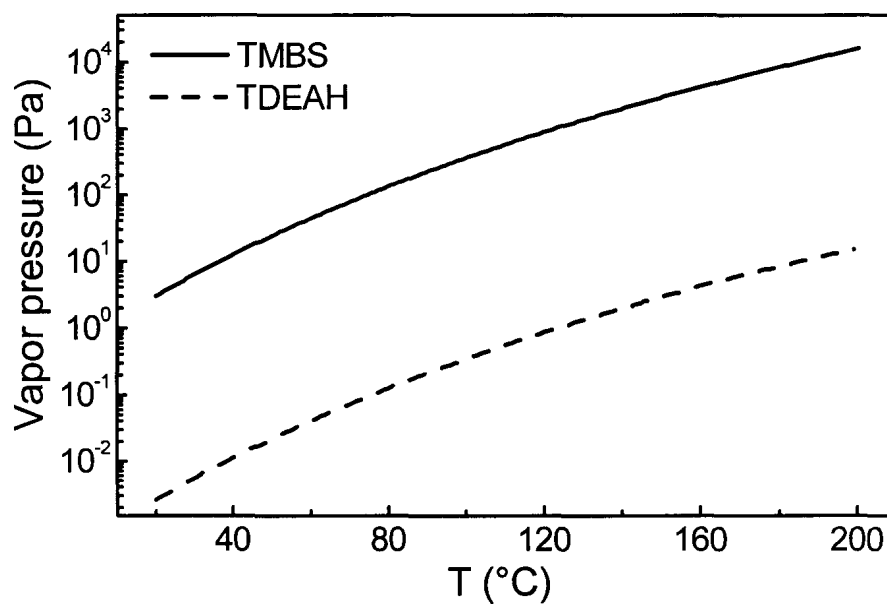


Figure 3.3: Vapour pressures of TDEAH and TMBS.

3.3 Deposition of Hf silicate films by ALD

3.3.1 ALD facility and preparation of silicon substrate

The Hf silicate films were deposited at the in situ processing (ISP) facility at the Institute for Microstructural Sciences (IMS) in National Research Council of Canada (NRCC). Figure 3.4 shows the diagram of the ISP facility, which has a base vacuum of 10^{-10} Torr. The 4-inch Si wafer is loaded from the Load-lock chamber and can be transferred through the tunnel to other chambers for processing. After deposition, in situ annealing and XPS analysis can be done without breaking vacuum.

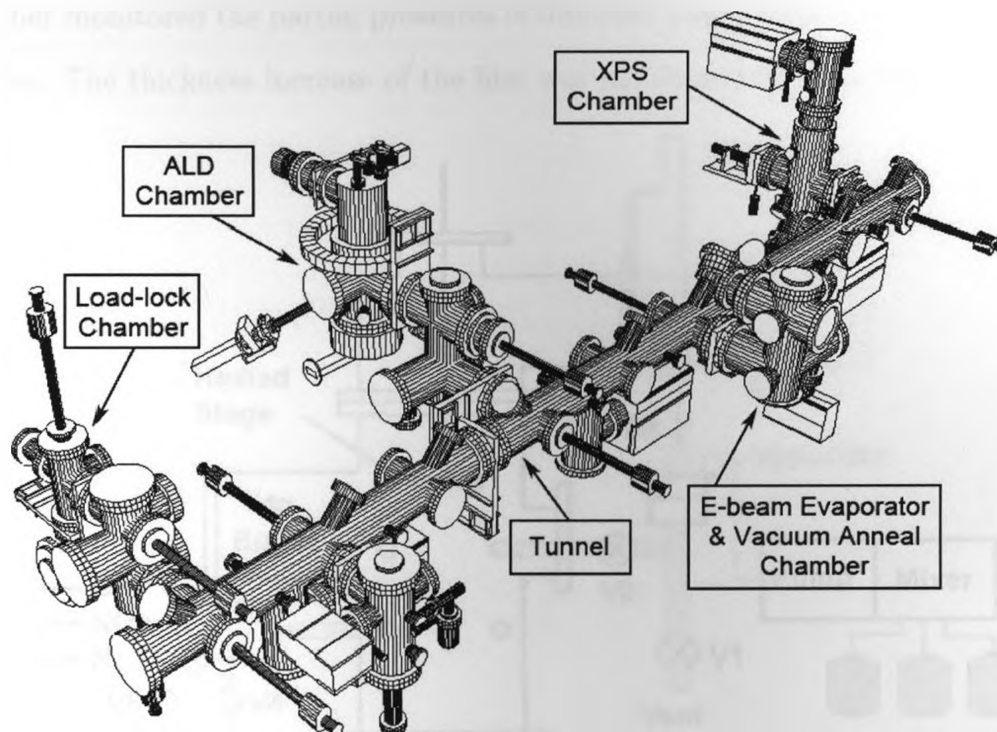


Figure 3.4: ISP processing facility for 4-inch wafer at NRCC-IMS.

Figure 3.5 shows the schematic structure of the ALD system. The ALD chamber wall was heated to $<100^{\circ}\text{C}$. The TDEAH precursor was dissolved in octane with the concentration of 0.1 M. A liquid injection pump delivered TDEAH into a vapourizer

which was heated to 140°C. Normally, valve V1 is open and V2 is closed. The vapourized Hf precursor was vented out. During the Hf precursor pulse, V2 was open and V1 was closed, and the Hf precursor was introduced into the deposition chamber via Ar carrier gas with a flow rate of 50 standard cubic centimeters per minute (sccm). The silicon precursor was stored in a bubbler which was heated to 50°C before deposition. N₂ was flowing at all times. Normally V3 was open and V5 and V4 were closed. During Si precursor pulse, V3 was closed and V5 and V4 were open. N₂ then flowed through the bubbler and carried Si precursor into the deposition chamber. In this study, the substrate temperature (T_{sub}) was varied in the range 200–350°C. A residual gas analyzer (RGA) connected to the deposition chamber monitored the partial pressures of different gases involved in the film growth process. The thickness increase of the film was monitored by an in situ ellipsometer.

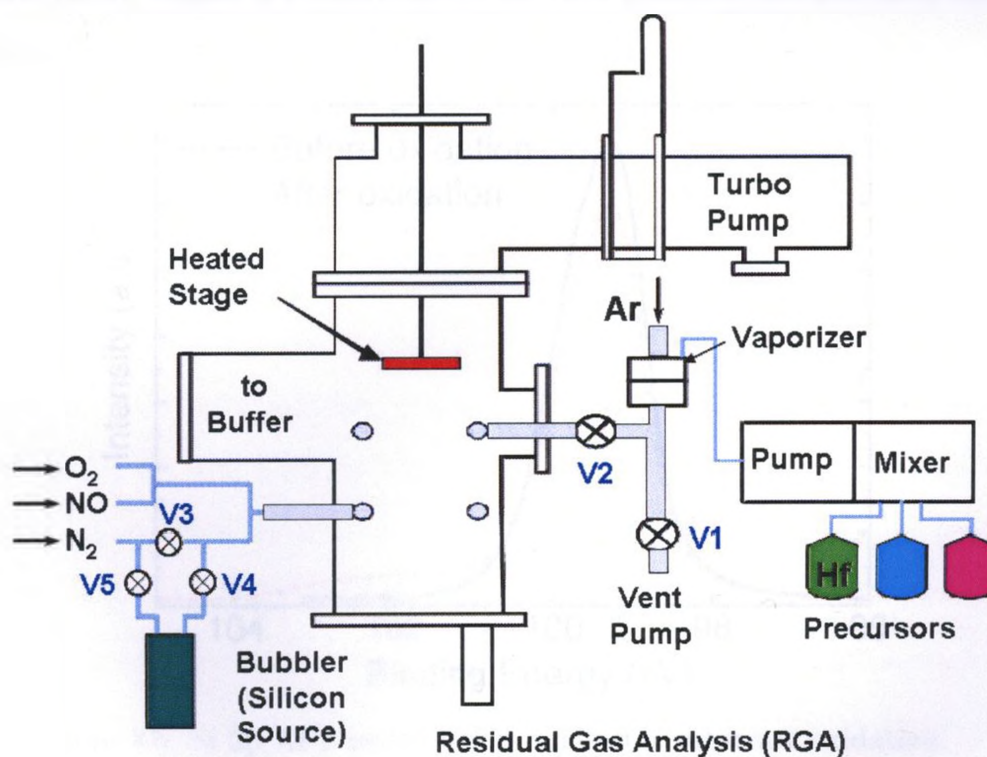


Figure 3.5: Schematic of the ALD system at NRCC-IMS.

Table 3.1 lists the steps of a typical deposition cycle.

Table 3.1: A typical film deposition cycle.

Step	Process	Time (s)
1	N ₂ (20 sccm) purge	33
2	TDEAH (0.2 ml/min) + Ar (50 sccm) + N ₂ (20 sccm)	18
3	N ₂ (20 sccm) purge	23
4	N ₂ (20 sccm) through TMBS bubbler	33

The p-type Si(001) wafers were cleaned by the Radio Corporation of America (RCA) method with a HF dip as the last step and mounted in ALD setup. Before deposition, the substrates were oxidized for 300 s in oxygen at 500 °C to eliminate the -H terminated surface. In situ XPS measurements were performed using Mg $K\alpha$ (1253.6 eV) x rays before and after substrate oxidation to estimate the thickness of the thermal oxide layer. Figure 3.6 shows the Si 2p XPS peaks before and after substrate oxidation.

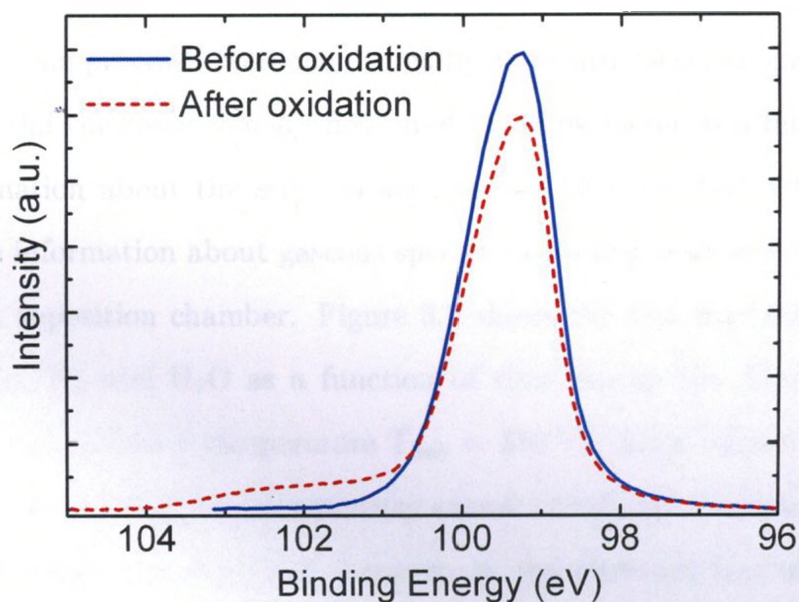


Figure 3.6: Si 2p XPS peaks before and after substrate oxidation.

The oxide layer thickness can be calculated using Equation [20]:

$$I = I_0 e^{-d/(\lambda_f \sin \theta)} \quad (3.1)$$

where I is the intensity of the substrate peak of a sample covered with a film of thickness d , I_0 is the corresponding peak from an oxide-free (hydrogen-passivated) substrate, λ_f is the attenuation length (AL) for the photoelectrons in the thin film and θ is the photoelectron takeoff angle. If we use 2.5 nm as the AL of photoelectrons excited by Mg $K\alpha$ x rays in SiO_2 film [21], the thickness of the thermal oxide layer can be determined to be $d = 0.35$ nm, using the ratio of the Si 2p peak intensities after and before substrate oxidation (Fig. 3.6).

3.3.2 ALD growth process of Hf silicate films

The film deposition processes were monitored by an in situ spectroscopic ellipsometer and a RGA. Film thickness changes measured by ellipsometer as a function of time provide information about the self-limiting reaction between TDEAH and TMBS. RGA provides information about gaseous species (including reactants and products) present in the deposition chamber. Figure 3.7 shows the film thickness and partial pressures of Ar, N_2 and H_2O as a function of time during the ALD growth of a Hf silicate film at substrate temperature $T_{\text{sub}} = 350^\circ\text{C}$. Since refractive indices for ultrathin films are not available, ellipsometry cannot accurately measure the thickness for films of thickness <10 nm [18]. However, in the ultrathin film regime, in situ ellipsometry can still be used to monitor changes in film thickness as the growth proceeds: therefore a relative uncertainty of $\pm 10\%$ is assigned to film thickness values from ellipsometry. The pressure values (shown on the vertical axis at the right) are approximately four orders of magnitude lower than the true partial pressures inside

the deposition chamber due to the presence of an orifice between the chamber and the RGA filament.

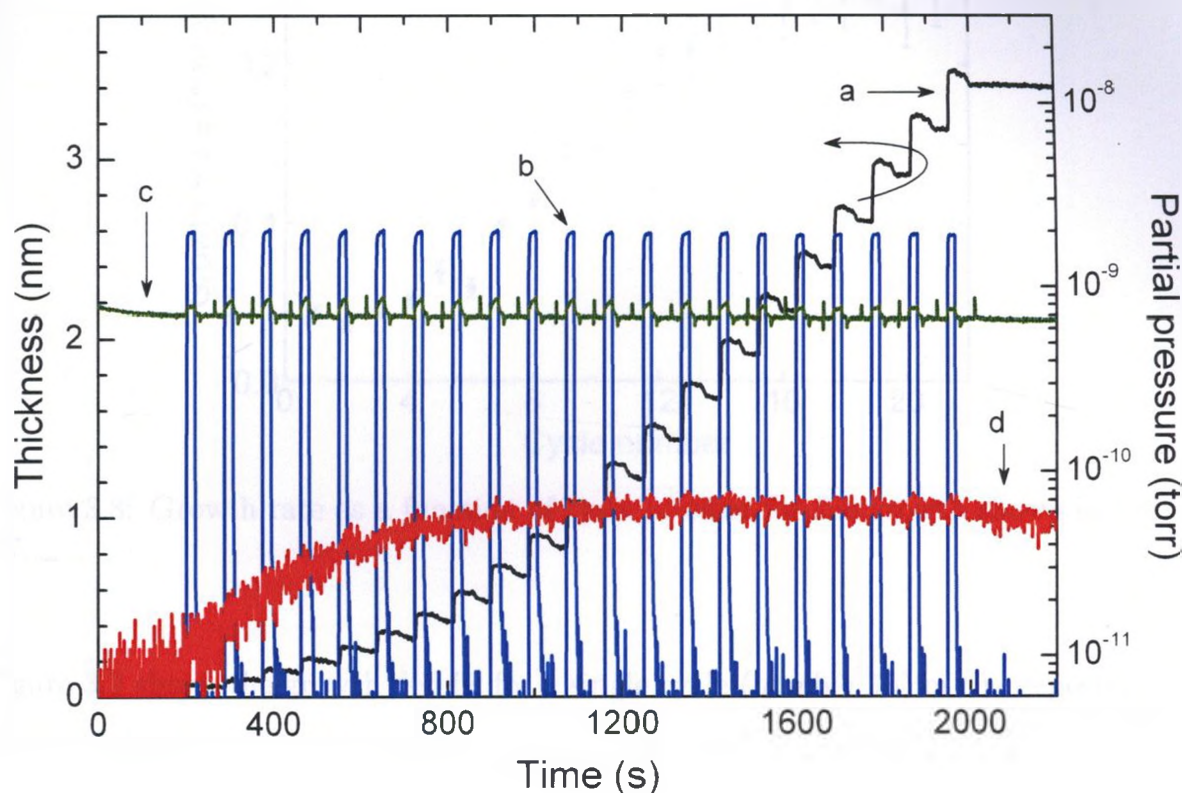


Figure 3.7: Growth process of a film deposited at 350 °C: a – film thickness measured by ellipsometry; b – Ar partial pressure; c – N₂ partial pressure; d – H₂O partial pressure.

Figure 3.8 shows the growth rate as a function of cycle number: the growth rate of the first several cycles is small, specifically ~ 0.05 nm/cycle initially as the film thickness increases approximately parabolically with cycle number. This behaviour indicates that there is an effective barrier for TDEAH and TMBS to adsorb onto the initial silicon suboxide surface. The growth rate increases gradually with cycle number and finally reaches a stable value after ~ 14 cycles. Figure 3.7 shows a concomitant increase in water pressure after the commencement of film deposition. Therefore, H₂O is a reaction product since no water source is involved in the reaction between TDEAH and TMBS.

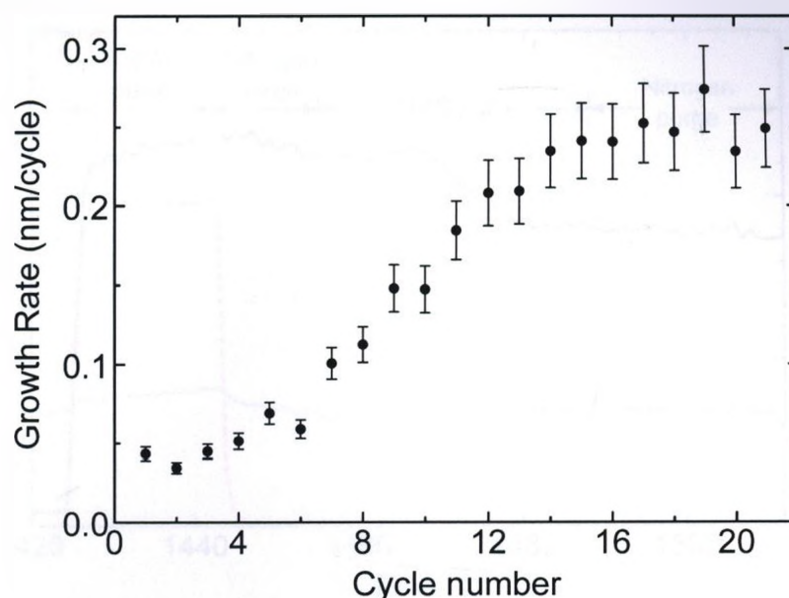


Figure 3.8: Growth rate as a function of cycle number for the growth shown in Fig. 3.7.

Figure 3.9 shows the growth details for a single cycle (number 15) of the deposition, corresponding to the linear range of the growth curve shown in Fig. 3.7 (thickness from ellipsometry). After the introduction of TDEAH into the growth chamber, TDEAH molecules saturate the surface quickly (within $\sim 3\text{--}4$ s). It was observed that additional exposure to the TDEAH precursor using a longer pulse time results in no further growth of the film. However, it takes a finite time for the Si precursor, TMBS, to react with the surface. Figure 3.9 shows that the thickness of the film has equilibrated (i.e., ceases to change) after ~ 20 s exposure to TMBS even though TMBS vapour is still present and available in the chamber. The ellipsometry trace in Fig. 3.9 clearly shows the self-limiting behaviour of both the TDEAH and TMBS precursors corresponding to the 15th growth cycle.

In order to confirm that the ellipsometric data provided a valid metric for film thickness, several samples were prepared following a specific number of cycles, and the samples were then examined via HRTEM to establish an independent measure of

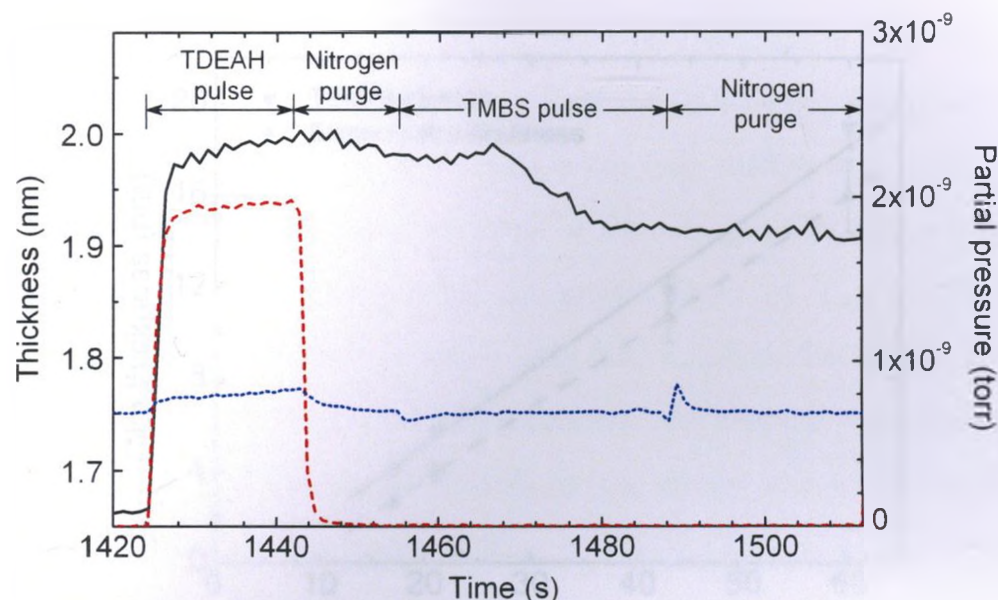


Figure 3.9: Details of the variation of the film thickness and gaseous partial pressures during the 15th growth cycle of the deposition (at 350 °C) shown in Fig. 3.7: film thickness (solid curve) measured by ellipsometry; Ar partial pressure (dashed curve); N₂ partial pressure (dotted curve). Note that TDEAH is delivered by argon, while TMBS is delivered by nitrogen.

film thickness. Figure 3.10 shows film thicknesses determined from both TEM (uncertainty estimated to be 5%) and ellipsometry (uncertainty estimated to be 10%) as a function of the number of cycles at substrate temperature 350 °C. Linear fits to both sets of data produce a positive abscissa intercept which confirms the initial non-linear behaviour described earlier. As well, the slopes are in agreement within 10%: specifically 0.33 ± 0.02 nm/cycle for the TEM data and 0.31 ± 0.03 nm/cycle for the ellipsometric data.

Figure 3.11 shows a portion of the growth cycle for $T_{\text{sub}} = 200$ °C. Here, even after ~ 100 s of TMBS exposure, the reaction between the precursors is not yet complete as the film thickness is still changing.

Figure 3.12 shows the growth rate as a function of TMBS pulse time at three different substrate temperatures in the range 250–350 °C. At $T_{\text{sub}} = 350$ °C, ~ 20 s of TMBS

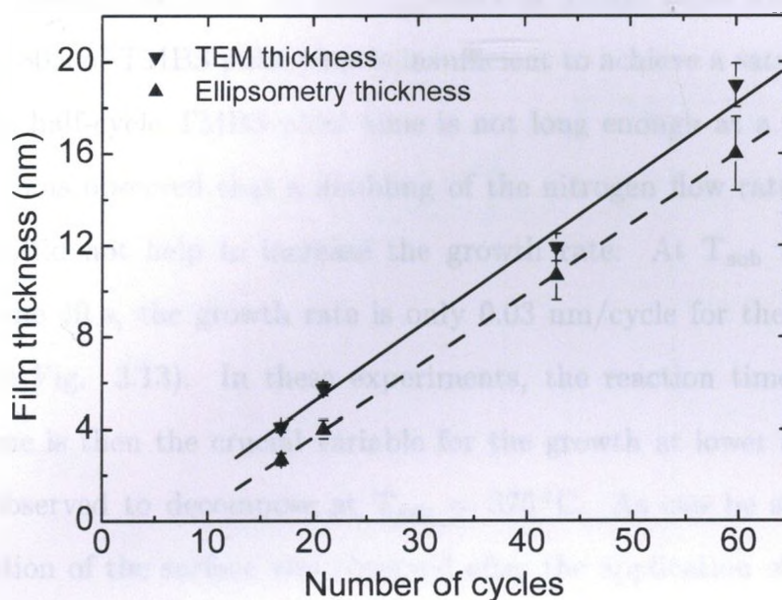


Figure 3.10: Film thickness as a function of the number of cycles at $T_{\text{sub}} = 350^\circ\text{C}$. Slope of linear fit (solid line) to TEM data = 0.33 ± 0.02 nm/cycle; slope of linear fit (dashed line) to ellipsometry data = 0.31 ± 0.03 nm/cycle.

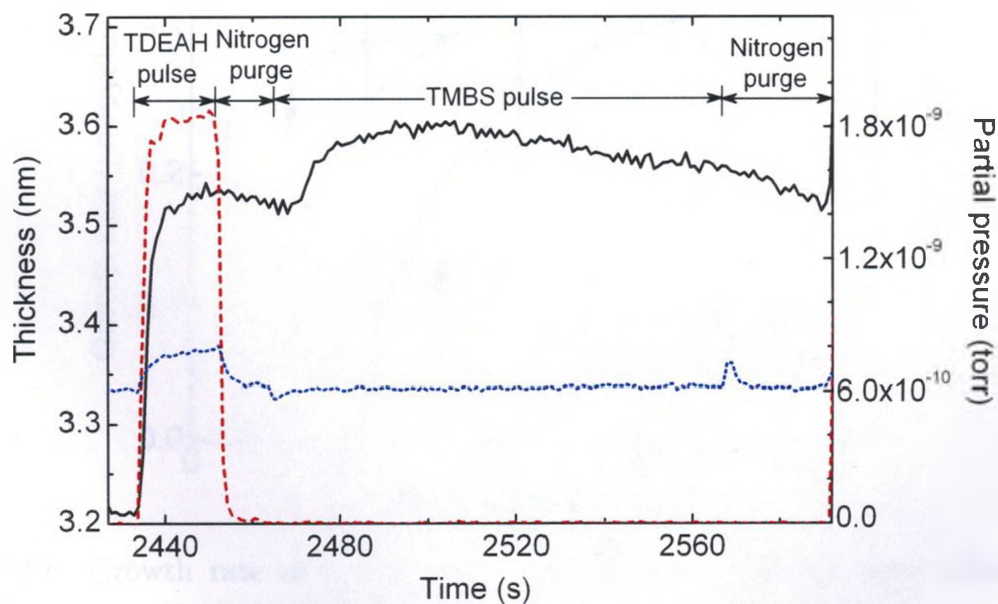


Figure 3.11: One of the growth cycles at $T_{\text{sub}} = 200^\circ\text{C}$: film thickness (solid curve) measured by ellipsometry; Ar partial pressure (dashed curve); N_2 partial pressure (dotted curve).

pulse time saturates the surface. At 300 °C, ~ 40 s of TMBS pulse time is required. At 250 °C, even 80 s of TMBS pulse time is insufficient to achieve a saturated growth rate. When the half-cycle TMBS pulse time is not long enough at a low substrate temperature, it was observed that a doubling of the nitrogen flow rate through the TMBS bubbler did not help to increase the growth rate. At $T_{\text{sub}} = 200$ °C and TMBS pulse time 40 s, the growth rate is only 0.03 nm/cycle for the N_2 flow rate of 40 sccm (see Fig. 3.13). In these experiments, the reaction time rather than precursor volume is then the crucial variable for the growth at lower temperatures. TDEAH was observed to decompose at $T_{\text{sub}} = 375$ °C. As can be seen from Fig. 3.14, no saturation of the surface was observed after the application of the TDEAH pulse. Therefore, the temperature window to achieve reproducible ALD growth is 250–350 °C using the precursors TDEAH and TMBS at a reasonable precursor pulse time.

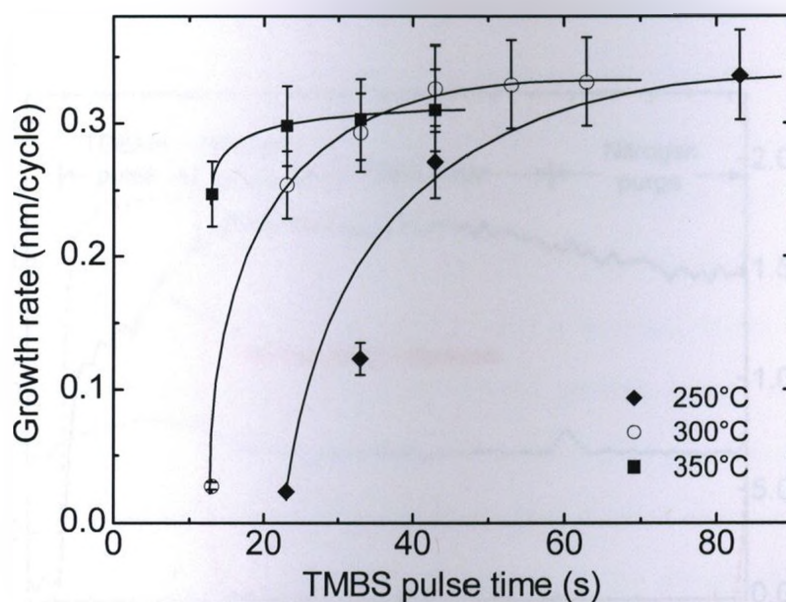


Figure 3.12: Growth rate as a function of TMBS pulse time for three substrate temperatures (curves are to guide the eye).

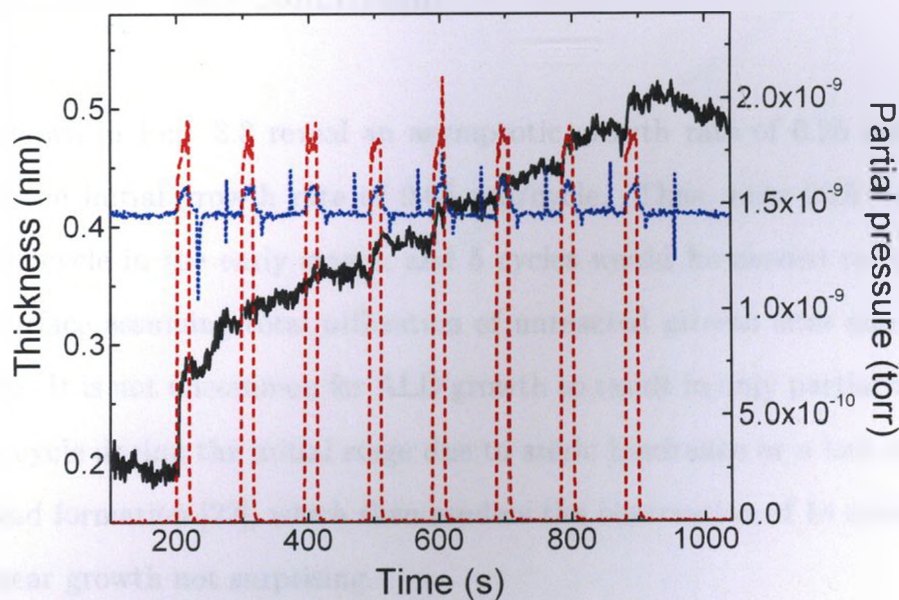


Figure 3.13: Film deposition at $T_{\text{sub}} = 200\text{ }^{\circ}\text{C}$ and N_2 flow rate 40 sccm: film thickness (solid curve) measured by ellipsometry; Ar partial pressure (dashed curve); N_2 partial pressure (dotted curve).

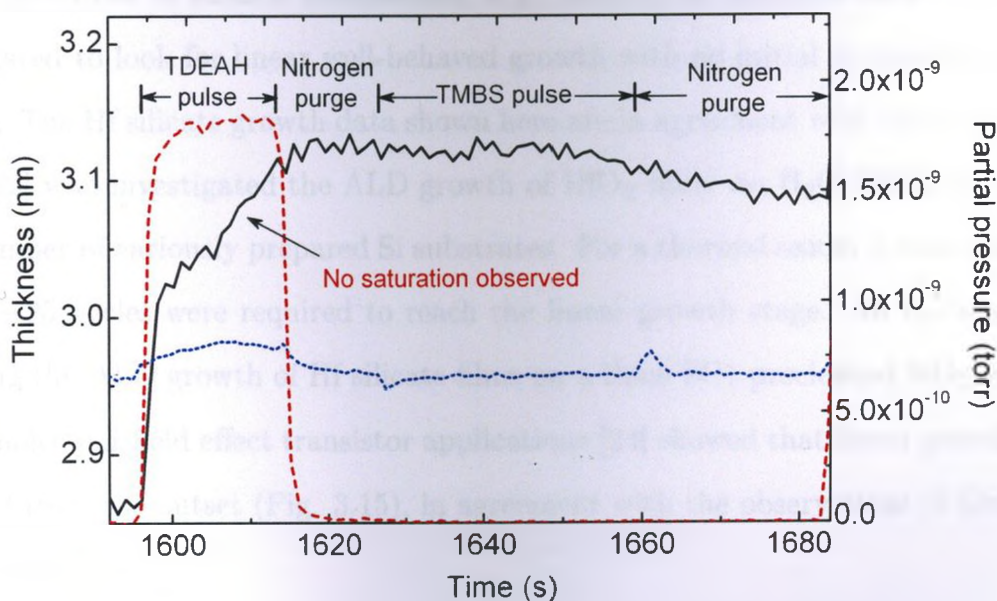


Figure 3.14: One of the growth cycles at $T_{\text{sub}} = 375\text{ }^{\circ}\text{C}$: film thickness (solid curve) measured by ellipsometry; Ar partial pressure (dashed curve); N_2 partial pressure (dotted curve).

3.4 Discussion and conclusion

The data shown in Fig. 3.8 reveal an asymptotic growth rate of 0.25 nm/cycle in contrast to the initial growth rate of 0.05 nm/cycle. Thus, only 20% coverage is achieved per cycle in the early stages, and 5 cycles would be needed to completely cover the surface assuming total utilization of unreacted growth sites and layer-by-layer growth. It is not uncommon for ALD growth to result in only partial monolayer growth per cycle during the initial stage due to steric hindrance or a lack of reactive sites or island formation [22], which then renders the observation of 14 cycles needed to reach linear growth not surprising.

For future technology applications using high- κ dielectrics, the thicknesses required will be $\sim 3\text{--}4$ nm, and well-controlled growth rates are preferable for thicknesses $< 3\text{--}5$ nm. Given the small gate thicknesses required, the present data suggest that a different initial Si surface composition, e.g., SiO_xN_y or chemical oxide should be investigated to look for linear well-behaved growth with no initial nucleation barrier [22, 23]. The Hf silicate growth data shown here are in agreement with those of Green *et al.* [22] who investigated the ALD growth of HfO_2 films via $\text{H}_2\text{O}/\text{HfCl}_4$ chemistry on a number of variously prepared Si substrates. For a thermal oxide, it was observed that 15–25 cycles were required to reach the linear growth stage. An investigation involving the ALD growth of Hf silicate films on a thick SC1 precleaned SiO_2 surface for biomolecular field effect transistor applications [24] showed that linear growth was achieved from the outset (Fig. 3.15), in agreement with the observations of Green *et al.* [22] for HfO_2 .

It can be concluded from the in situ spectroscopic ellipsometry data that in the temperature range $200\text{--}350^\circ\text{C}$ the reaction between TDEAH and TMBS is self-limited. The TDEAH pulse saturates the surface in a short time, $\sim 3\text{--}4$ s (Figs. 3.9

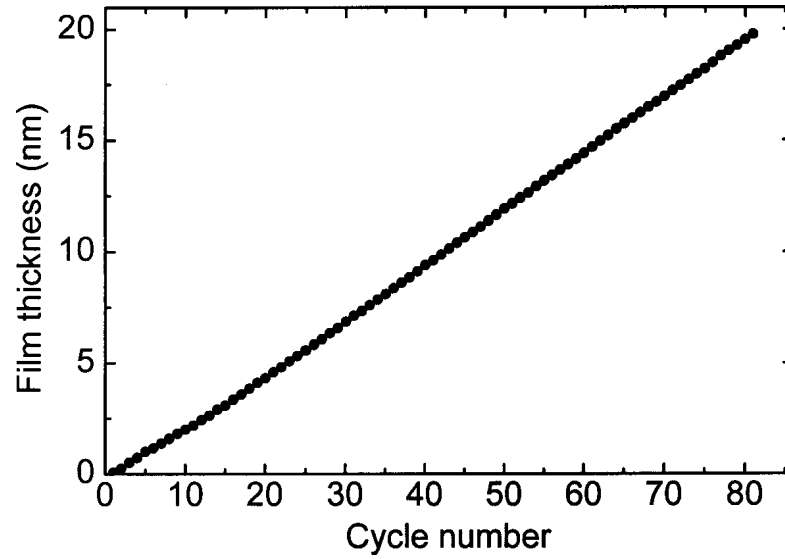


Figure 3.15: Film thickness as function of cycle number measured by ellipsometry for a film deposited on SC1 cleaned SiO_2 surface at $T_{\text{sub}} = 350^\circ\text{C}$.

and 3.11), at all temperatures in the above range. The growth rate mainly depends on substrate temperature and TMBS pulse time. At lower temperature, it takes longer time for TMBS to saturate the surface, i.e., to reach a self-limiting growth rate. If the TMBS pulse time is long enough to saturate the surface, the growth rate varies within $\sim 8\%$ at different substrate temperatures, see Fig. 3.12.

BIBLIOGRAPHY

- [1] T. Suntola, Mater. Sci. Rep. **4**, 261 (1989).
- [2] M. Ylilammi, Thin Solid Films **279**, 124 (1996).
- [3] T. S. Suntola, A. J. Pakkala, and S. G. Lindfors, *Us patent 4413022* (1983).
- [4] R. L. Puurunen, Chem. Vapor Depos. **9**, 249 (2003).
- [5] L. Niinistö, J. Päiväsaari, J. Niinistö, M. Putkonen, and M. Nieminen, Phys. Status Solidi A **201**, 1443 (2004).
- [6] H. Zhang and R. Solanki, J. Electrochem. Soc. **148**, F63 (2001).
- [7] K. Kukli, M. Ritala, M. Leskel, T. Sajavaara, J. Keinonen, D. C. Gilmer, and P. J. Tobin, Mater. Sci. Eng. B **109**, 2 (2004).
- [8] W.-K. Kim, S.-W. Rhee, N.-I. Lee, J.-H. Lee, and H.-K. Kang, J. Vac. Sci. Technol. A **22**, 1285 (2004).
- [9] Z. M. Rittersma, F. Roozeboom, M. A. Verheijen, J. G. M. van Berkum, T. Dao, J. H. M. Snijders, E. Vainonen-Ahlgren, E. Tois, M. Tuominen, and S. Haukka, J. Electrochem. Soc. **151**, C716 (2004).
- [10] M. A. Alam and M. L. Green, J. Appl. Phys. **94**, 3403 (2003).
- [11] R. L. Puurunen, J. Appl. Phys. **95**, 4777 (2004).
- [12] M. Ritala, K. Kukli, A. Rahtu, P. I. Räisänen, M. Leskelä, T. Sajavaara, and J. Keinonen, Science **288**, 319 (2000).
- [13] R. G. Gordon, J. Becker, D. Hausmann, and S. Suh, Chem. Mater. **13**, 2463 (2001).
- [14] D. M. Hausmann, E. Kim, J. Becker, and R. G. Gordon, Chem. Mater. **14**, 4350 (2002).
- [15] K. Kukli, M. Ritala, T. Sajavaara, J. Keinonen, and M. Leskel, Chem. Vapor Depos. **8**, 199 (2002).

- [16] T. C. Chen, C. Y. Peng, C. H. Tseng, M. H. Liao, M. H. Chen, C. I. Wu, M. Y. Chern, P. J. Tzeng, and C. W. Liu, *IEEE Trans. Electron Devices* **54**, 759 (2007).
- [17] Y. Senzaki, S. Park, H. Chatham, L. Bartholomew, and W. Nieveen, *J. Vac. Sci. Technol. A* **22**, 1175 (2004).
- [18] J. Kim and K. Yong, *J. Electrochem. Soc.* **152**, F45 (2005).
- [19] S. Kamiyama, T. Miura, Y. Nara, and T. Arikado, *Electrochem. Solid State Lett.* **8**, G215 (2005).
- [20] T. L. Alford, L. C. Feldman, and J. W. Mayer, *Fundamentals of Nanoscale Film Analysis* (Springer, 2007).
- [21] R. Flitsch and S. I. Raider, *J. Vac. Sci. Technol.* **12**, 305 (1975).
- [22] M. L. Green, M.-Y. Ho, B. Busch, G. D. Wilk, T. Sorsch, T. Conard, B. Brijs, W. Vandervorst, P. I. Raisanen, D. Muller, et al., *J. Appl. Phys.* **92**, 7168 (2002).
- [23] M. M. Frank, Y. J. Chabal, M. L. Green, A. Delabie, B. Brijs, G. D. Wilk, M.-Y. Ho, E. B. O. da Rosa, I. J. R. Baumvol, and F. C. Stedile, *Appl. Phys. Lett.* **83**, 740 (2003).
- [24] W. Jiang, D. Landheer, G. Lopinski, W. R. McKinnon, A. Rankin, E. Ghias-Begloo, R. Griffin, N. G. Tarr, N. Tait, J. Liu, et al., *ECS Trans.* **16**, 441 (2008).

CHAPTER 4

FILM COMPOSITION AND REACTION MECHANISM BETWEEN TDEAH AND TMBS¹

The compositions of $\text{Hf}_x\text{Si}_{1-x}\text{O}_2$ films grown by ALD were measured by XPS and MEIS. The nitrogen impurity was also probed by nuclear reaction analysis (NRA). In this chapter, the film composition is discussed and a possible reaction mechanism between TDEAH and TMBS is proposed.

4.1 Film composition

4.1.1 XPS analysis

The in situ XPS data were taken by a PHI 5000 instrument with a non-monochromatic Mg $K\alpha$ x-ray ($h\nu = 1253.6$ eV) source in the standard 54° geometry (x-ray source 9° off normal and the electron spectrometer 45° off normal). The pass energy for

¹A version of this chapter has been published in a journal article. J. Liu, W. N. Lennard, L. V. Goncharova, D. Landheer, X. Wu, S. A. Rushworth, and A. C. Jones, J. Electrochem. Soc. **156**, G89 (2009)

multiplex is 23.50 eV. After being removed from the chamber, the films were also analyzed ex situ by PHI 5500 system with a monochromatic Al $K\alpha$ x-ray ($h\nu = 1486.6$ eV) source in standard 90° geometry (both the x-ray source and electron spectrometer 45° off normal). The pass energy for ex situ multiplex scan is 11.75 eV.

For Si 2p photoelectrons excited by Mg $K\alpha$ x ray and Al $K\alpha$ x ray, the mean free paths (λ) in SiO_2 are ~ 2.5 nm [1] and ~ 3.0 nm [2], respectively. It is expected that the λ -value of Si 2p photoelectrons in Hf silicate films is approximately the same as in SiO_2 . In an XPS spectrum, $\sim 95\%$ of the photoelectron yield arises from a depth of $\sim 3\lambda$. Considering the 45° photoelectron takeoff angle, the sampling depth in our XPS analyses is therefore ~ 5.8 nm. The thicknesses of Hf silicate films in this study are in the range 4–5 nm. Therefore, the XPS data measure the photoelectron yield from the entire film. In the analysis of the XPS data, the Si $2p_{3/2}$ peak at 99.3 eV was used as the reference.

Figure 4.1 shows the ex situ XPS Si 2p, Hf 4f and O 1s peaks for a Hf silicate film grown at 350°C . In Fig. 4.1(b), the separation between the Hf $4f_{5/2}$ and Hf $4f_{7/2}$ peaks is 1.66 eV, in good agreement with results of Ulrich *et al.* [3]. The binding energy and full width at half maximum (FWHM) of the Hf $4f_{7/2}$ peak are 18.4 eV and 1.26 eV, respectively. Considering the composition of the specific film [$\text{Hf}/(\text{Si}+\text{Hf}) = 0.25$] studied here, both values agree very well with results of Ref. [3] for $\text{Hf}_x\text{Si}_{1-x}\text{O}_2$ films with $x = 0.25$. No Hf silicide bonding at binding energy (BE) = 14.3 eV or HfO_2 bonding at BE = 17.7 eV [4] was observed.

For the O 1s peaks [Fig. 4.1(c)], it is believed that the peaks at BE of 533.0 eV and 531.8 eV correspond to Si–O–Si and Si–O–Hf bonds [5], respectively. Their separation is 1.28 eV, in agreement with O'Connor *et al.* [6]. Lao *et al.* [7] observed an O 1s peak at 535.0 eV in plasma-enhanced ALD HfO_2 films which they attributed

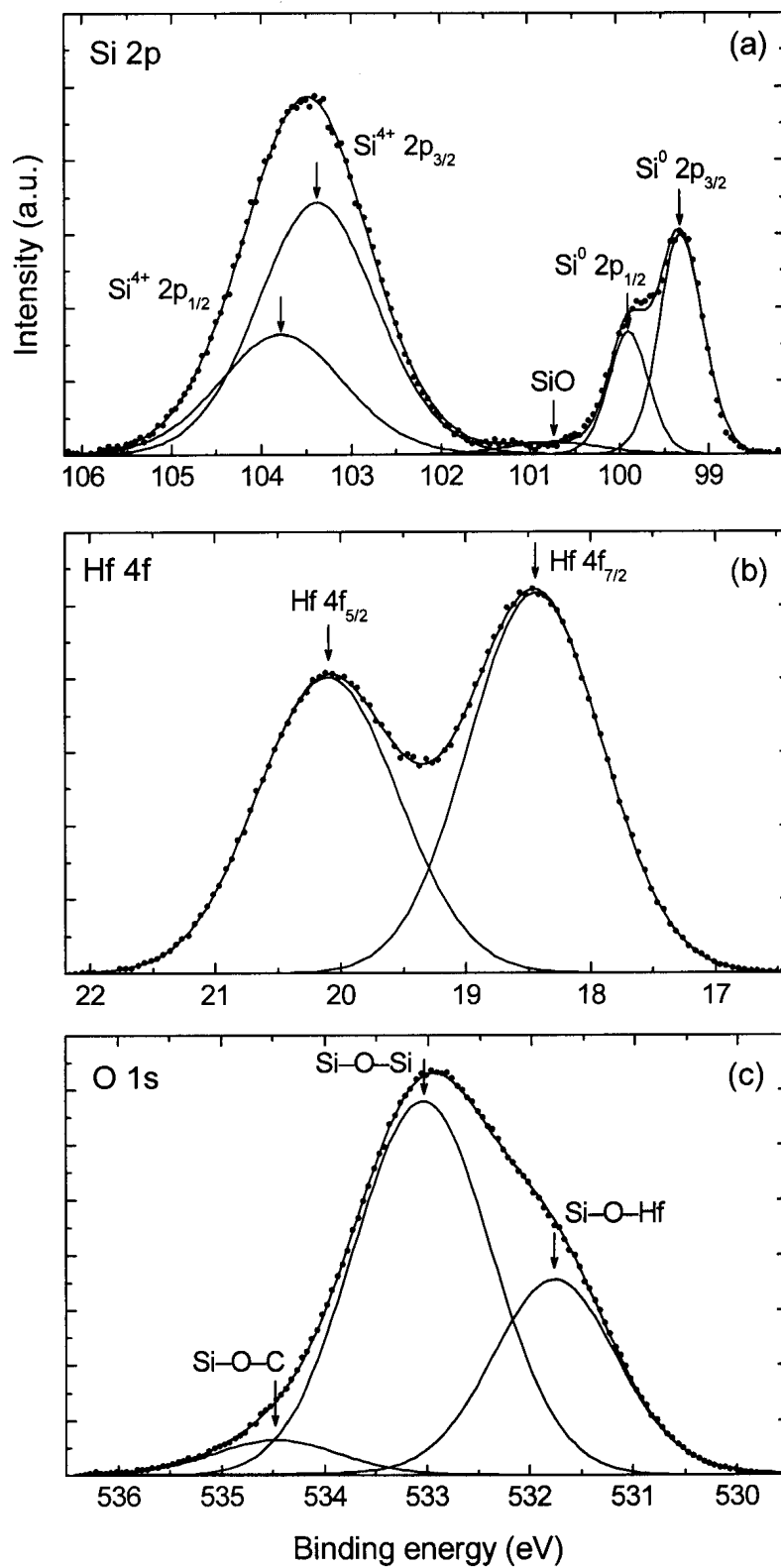


Figure 4.1: Ex situ XPS peaks of a film deposited at 350 °C: (a) Si 2p, (b) Hf 4f, and (c) O 1s peaks.

to the Hf–O–C bond. In this study, the O 1s peak at 534.5 eV should originate from the Si–O–C bond, considering the composition of our films and the precursor chemistry.

Figure 4.2 shows the Si 2p, Hf 4f and O 1s XPS peaks of a film before and after in situ anneal at 800 °C for ~2 s. The intensities of Si 2p, Hf 4f and O 1s slightly increase after annealing due to the decomposition and evaporation of the unreacted precursors left on the surface after film deposition. The Si⁴⁺ 2p peak and Hf 4f peaks shift slightly to higher energy. This is probably due to an inner shell electron BE increase resulting from the decrease of the distance between atoms in the films which occurs in the densification process during annealing. The intensity of O 1s peak corresponding to Si–O–H bond [8] decreases slightly after annealing. The Si–O–H bonds were left on the film surface after the last TMBS pulse in the film deposition process, as will be discussed later. The decomposition of surface –OH bonds occurs via the reaction:

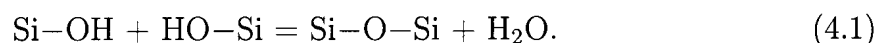


Figure 4.3 shows the in situ and ex situ C 1s XPS peaks for an as-grown film deposited at 350 °C. In the in situ spectrum [Fig. 4.3(a)], C 1s peaks at 286.85 and 285.45 eV are assigned to C–O and C–C bonds, respectively. The peak at BE = 281.0 eV is attributed to the C–Hf bond [9]. After atmospheric exposure, the C–Hf bond disappeared [Fig. 4.3(b)], indicating that the Hf carbide was oxidized upon exposure to air. Thus, the observation of the C=O or O–C–O [10] bond and the greatly increased C–C bond in the ex situ XPS spectrum is due to carbon contamination which is again caused by exposure to air. The slight shift (0.05 eV) between the C–C peaks from in situ and ex situ spectra is probably due to a small calibration difference for the two XPS systems since the observed 1.4 eV separation of the C–O and C–C peaks is the same for both the in situ and ex situ spectra.

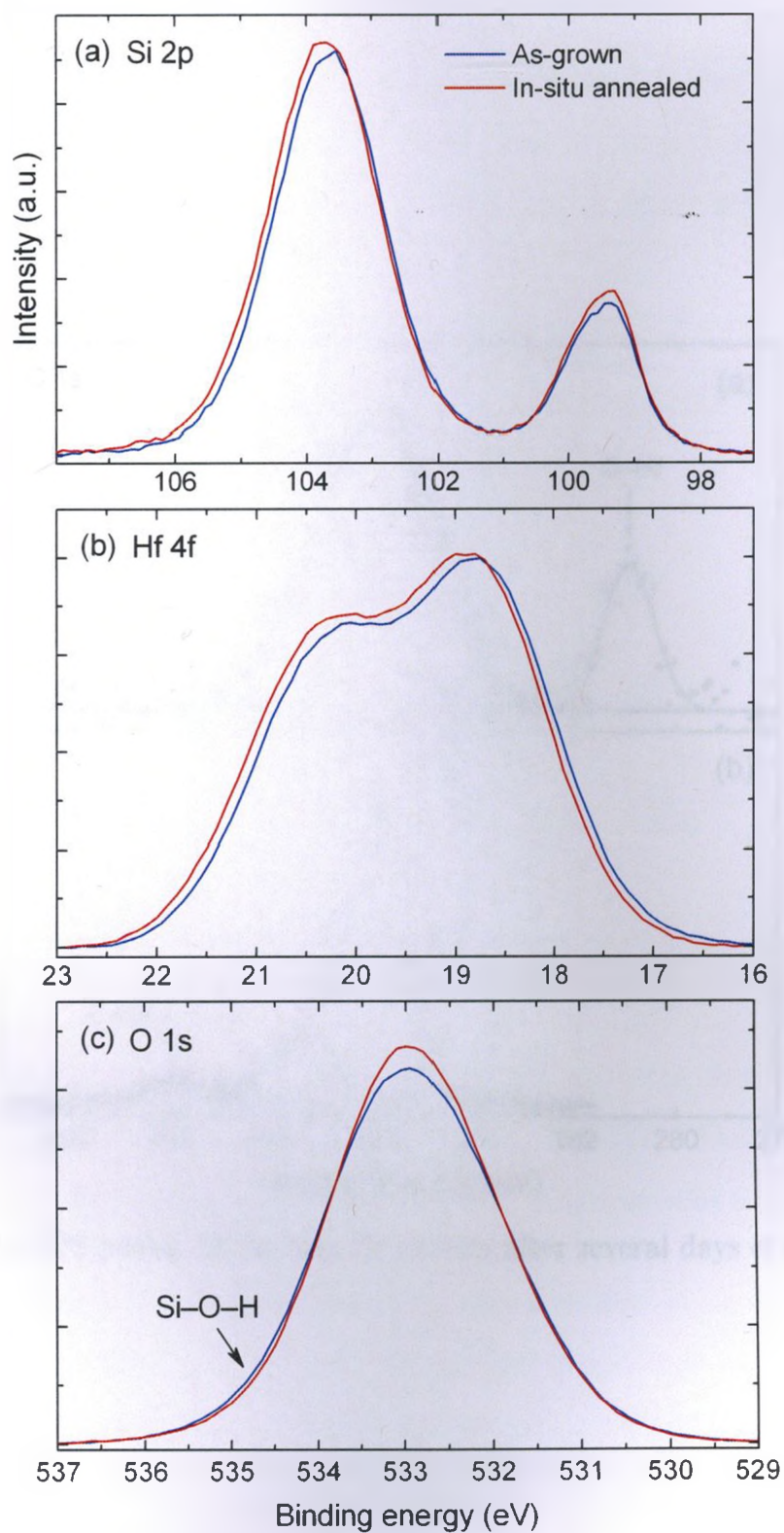


Figure 4.2: XPS peaks of a film before and after in situ anneal at 800°C for ~2 s: (a) Si 2p, (b) Hf 4f and (c) O 1s peaks.

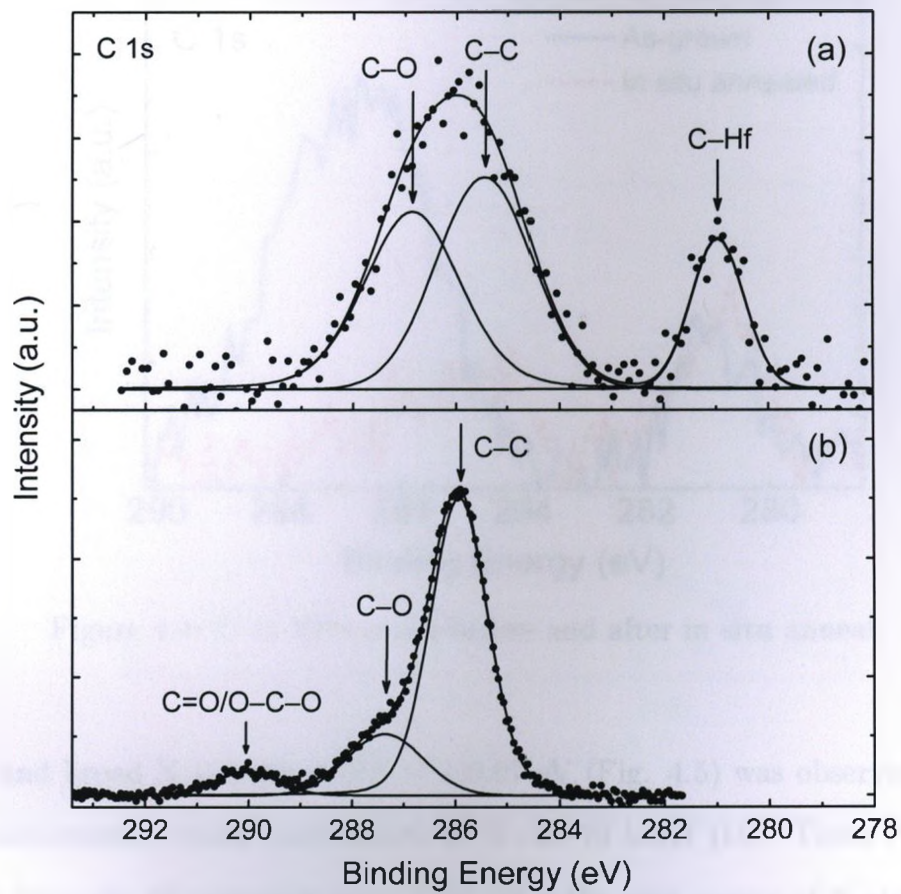


Figure 4.3: C 1s XPS peaks: (a) in situ, (b) ex situ after several days of exposure to air.

Figure 4.4 shows the C 1s peaks for a film grown at 250 °C before and after in situ anneal at 800 °C for ~2 s. The C 1s peaks which correspond to the C–C and C–O bonds were greatly reduced after in situ anneal. This is due to the decomposition of unreacted precursor left after film deposition as already mentioned. After in situ anneal, the C contamination can be reduced to ~1%.

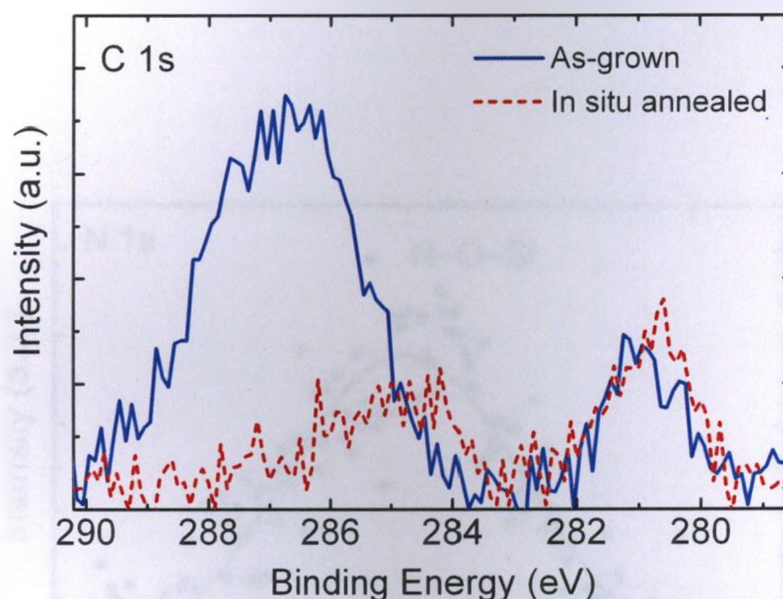


Figure 4.4: C 1s XPS peaks before and after in situ anneal.

A weak and broad N 1s peak at BE = 400.07 eV (Fig. 4.5) was observed by in situ XPS measurement, which corresponds to N–O–Si bond [11]. These N impurities were left from the Hf precursor since TDEAH is the only source of N atoms.

The film composition can be calculated from the intensities of in situ XPS peaks using Equation 2.9. Table 4.1 lists the as-grown film composition extracted from in situ XPS data at different substrate temperatures and TMBS pulse times.

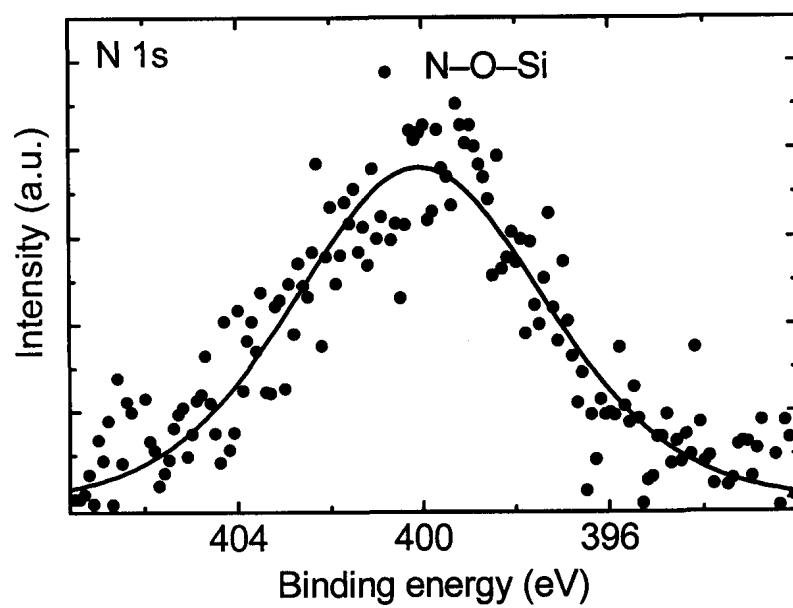


Figure 4.5: in situ N 1s XPS peak for a film deposited at 350 °C.

Table 4.1: As-grown film composition calculated from in situ XPS data and MEIS data.

Sample No.	T_{sub} [°C]	TMBS pulse time per cycle [s]	Composition [at.%) (MEIS)					Composition [at.%) (in situ XPS)					
			Hf	Si	O	C	Hf/(Hf+Si)	Hf	Si	O	C	N	Hf/(Hf+Si)
1368	350	13	9.7	21	62	6.7	0.31	7.1	21	67	3.8	1.1	0.25
1369	350	23	8.9	22	64	4.3	0.29	6.6	21	68	3.4	1.0	0.24
1371	350	33	8.9	23	66	2.9	0.28	6.9	22	67	3.3	1.0	0.24
1370	350	43	8.8	23	65	3.9	0.28	6.3	22	68	2.8	0.93	0.22
1373	300	23	9.4	22	63	4.8	0.29	6.8	20	67	4.4	1.4	0.25
1372	300	33	8.9	22	64	4.8	0.29	6.4	21	67	5.0	1.2	0.24
1374	300	43	8.2	22	60	9.5	0.27	6.2	21	68	3.8	1.0	0.23
1351	300	53	8.5	23	65	4.0	0.27	6.4	22	68	2.8	0.92	0.22
1352	300	63	8.3	23	63	5.7	0.26	6.2	22	68	3.2	0.96	0.22
1362	250	33	11	18	60	11	0.37	7.5	18	63	9.1	1.9	0.29
1366	250	43	11	20	64	4.7	0.35	8.1	19	66	5.7	1.4	0.30
1356	250	83	9.5	21	63	5.8	0.31	7.0	20	67	4.5	1.1	0.26
1367	200	103	12	19	62	6.0	0.38	8.2	18	65	7.1	1.4	0.31

4.1.2 MEIS analysis

Figure 4.6 shows the MEIS experimental data and simulation results for a film deposited at 350°C. The simulations are provided by a computer fitting program (derived from the QUARK-series [12] of elastic scattering simulations) where separate discrete layers are assumed to have abrupt boundaries. The arrows indicate the surface edge positions of Hf, Si, O and C, respectively, since elastic scattering surface energies are dependent only on the scattering angle and the mass ratio, M_2/M_1 ($M_1 = 1$ for protons). Figure 4.6(b) shows the composition profile extracted from the simulation and Table 4.2 lists the parameters used for each layer in the MEIS model. The top layer, considering its thickness, is believed to be just adventitious carbon contamination either from atmospheric exposure prior to the MEIS experiments or resulting from ion beam-induced hydrocarbon cracking even in an UHV environment. The second layer is the Hf silicate layer. The third layer is a Si suboxide layer containing a small Hf concentration. However, the detailed composition of this layer is still an open question, because it is not easy for MEIS to differentiate the Si atoms located at the bottom of the film from those Si atoms located in the substrate surface region.

Table 4.2: Parameters derived from a fit to the MEIS spectrum shown in Fig. 4.6(a).

MEIS model						
Layer	Thickness [nm]	Density [g/cm ³]	Concentration [at. %]			
			C	Hf	Si	O
1	0.12	2.7	55	0	23	22
2	3.08	3.6	1.0	10	22	66
3	1.50	2.3	0.10	3.9	46	50

In the MEIS experiment, a nitrogen ($M = 14$) peak is not observed, which indicates that N has a low concentration in the film. It should be noted that because of the

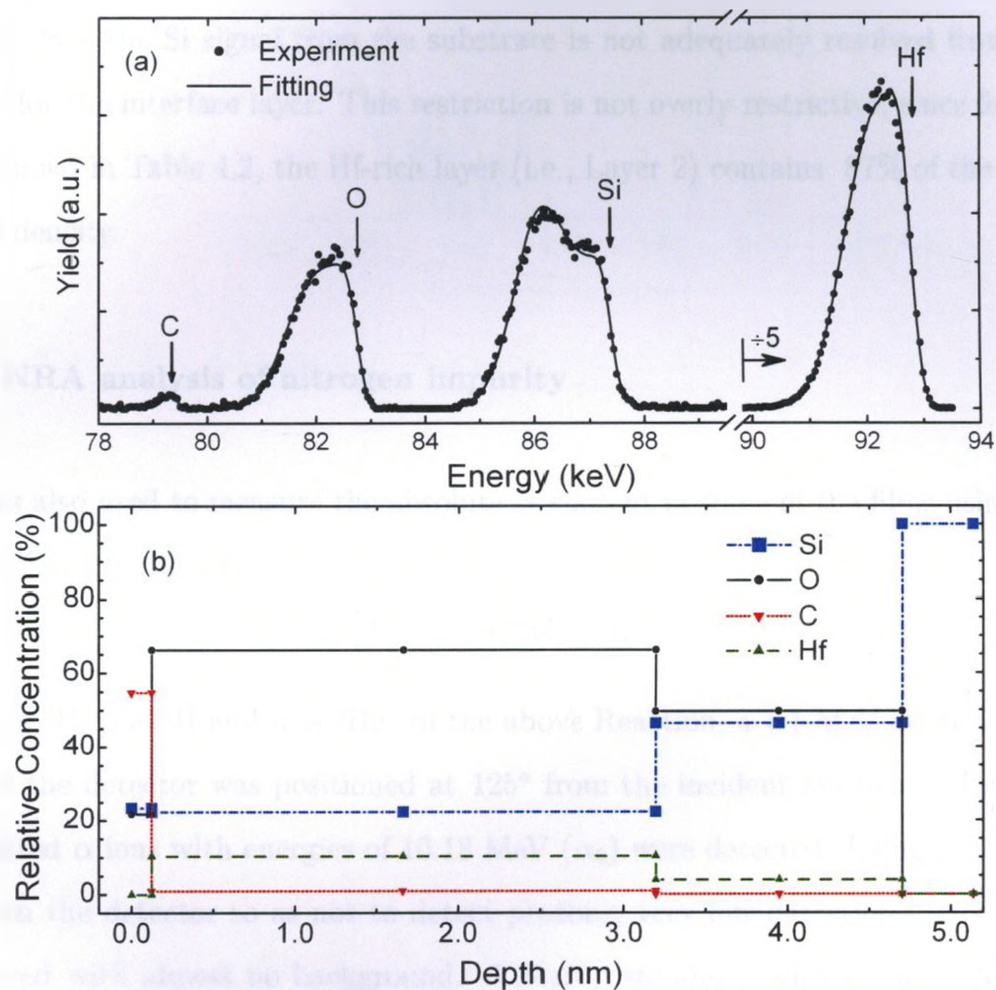


Figure 4.6: (a) MEIS spectrum for the sample deposited at 350 °C. The arrows indicate the positions of surface edges of Hf, Si, O and C, respectively. (b) The depth profiles of Hf, Si, O and C extracted from a fit to the spectrum shown in (a).

extensive energy width of the oxygen ($M = 16$) peak, signals from N atoms located at the surface and O atoms located at some depth into the film will overlap.

The film composition calculated from MEIS measurements is also listed in Table 4.1. When calculating the film composition from the MEIS data, the Hf-deficient layer is excluded since the Si signal from the substrate is not adequately resolved from the Si signal for the interface layer. This restriction is not overly restrictive, since for the results shown in Table 4.2, the Hf-rich layer (i.e., Layer 2) contains 87% of the total Hf areal density.

4.1.3 NRA analysis of nitrogen impurity

NRA was also used to measure the absolute N content in some of the films using the reaction $^{14}\text{N}(\text{d},\alpha)^{12}\text{C}$, i.e.,



where d is ^2H , p is ^1H and α is ^4He . In the above Reaction, a 1.1 MeV d^+ beam was used and the detector was positioned at 125° from the incident ion beam direction. The emitted α ions with energies of 10.18 MeV (α_0) were detected. Using a low bias voltage on the detector so as not to detect protons, very low detection limits could be achieved with almost no background. A Si_3N_4 'standard' with known ^{14}N areal density of $1.052 \times 10^{18} \pm 5\% \text{ cm}^{-2}$ was used to calculate the N content in the Hf silicate films. Figure 4.7 shows the NRA spectra for N measurements. A bare Si sample was measured as background.

The description of samples and the experimental results are listed in Table 4.3 and 4.4, respectively. An in situ anneal was performed at 800°C for ~ 2 s. The range of 1.1 MeV d^+ ions in the Si substrate is $\sim 14 \mu\text{m}$. The thickest film (including Si cap

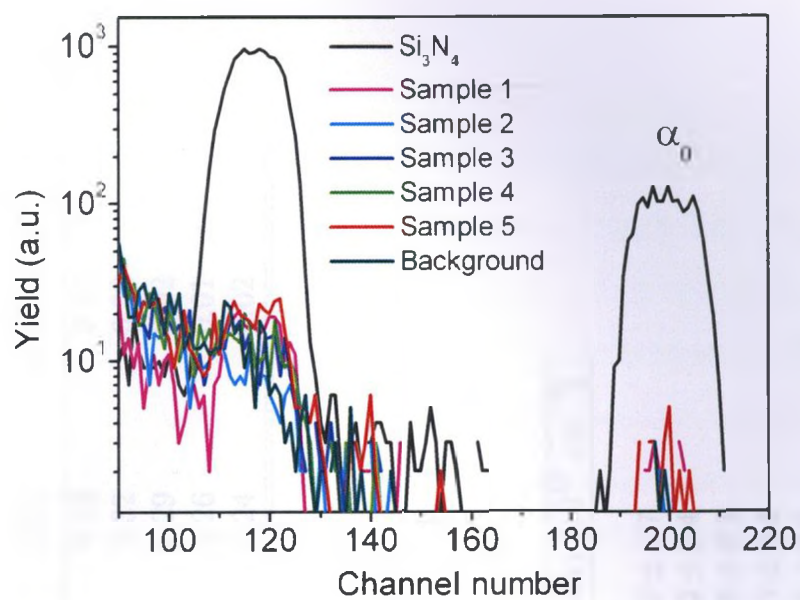


Figure 4.7: NRA measurements of N content in Hf silicate films.

layer) used for NRA analysis is ~ 32 nm. Therefore, the sampling depth of the NRA signal includes the entire film.

Table 4.3: Details of the samples used for NRA.

Sample	Sample description				Composition by in situ XPS	
	T_{sub} [°C]	Thickness [nm]	In situ anneal	Si cap layer thickness [nm]	$\frac{\text{Hf}}{\text{Hf}+\text{Si}}$	$\frac{\text{N}}{\text{Hf}+\text{Si}+\text{O}+\text{N}}$
Sample 1	250	4.5	No	-	0.33	0.03
Sample 2	250	4.7	Yes	20	0.32	0.02
Sample 3	250	11.5	Yes	20	0.29	0.02
Sample 4	250	2.3	Yes	12	0.26	0.01
Sample 5	250	2.3	No	12	0.24	0.02

Table 4.4: N areal density measured by NRA.

Sample	d^+ ions dose [μC]	α_0 yield	N areal density [10^{14} cm^{-2}]
Si_3N_4	1.6	1630	
Sample 1	80	30	3.9 ± 0.7
Sample 2	80	9	1.2 ± 0.4
Sample 3	80	6	0.8 ± 0.3
Sample 4	80	10	1.3 ± 0.4
Sample 5	80	20	2.6 ± 0.6
Background	80	14	1.8 ± 0.5

4.1.4 Discussion

Table 4.1 lists film composition as a function of deposition temperature and TMBS pulse time measured by in situ XPS and MEIS for a variety of films. For all samples shown in Table 4.1, the TDEAH absorption half-cycle is long enough to saturate the surface. The Hf/(Si+Hf) ratios derived from MEIS measurements are 3–5% higher than those measured by XPS, which probably results from the exclusion of the Hf-deficient layer from the MEIS values. The film composition depends mainly on the deposition temperature and only slightly on the TMBS pulse time in the temperature range 250–350 °C. As the substrate temperature increases, the Hf concentration depends only weakly on temperature in a non-monotonic manner. The Hf/(Si+Hf) ratio can be adjusted in the limited range 0.22 – 0.30 by varying both temperature and TMBS pulse time and the films were stoichiometric in all cases based on XPS and MEIS data, i.e., $O/(Hf+Si) \cong 2$.

From the XPS data, the C content is highest at lower temperatures, amounting to a few percent in all cases. At all temperatures, the in situ XPS data show that the C content decreases slightly with increasing TMBS pulse times, thereby demonstrating that C contamination in the film can be minimized by assuring that the self-limiting condition is achieved for the silanol precursor. An in situ anneal at 800 °C for ~2 s can reduce C contamination to ~1%.

The concentration of N in the film can only arise from the TDEAH precursor. The N concentrations observed by XPS are all ~1 atom% so long as the TMBS pulse times exceed the saturated value at that T_{sub} . This observation is expected since the N–Hf bond can be easily broken by the –OH functional group [13] as will be discussed in Section 4.2. The N content measured by NRA is of the same order as the background, see Table 4.4, i.e., $(1.80 \pm 0.27) \times 10^{14} \text{ cm}^{-2}$ for all the films except

Sample 1. A monolayer of Si(110) surface has an areal density of $9.59 \times 10^{14} \text{ cm}^{-2}$. Therefore, the N content in the films is lower than 1/6 of a monolayer, which is below the MEIS detection limit. It should be pointed out that XPS is very surface sensitive and the photoelectron yield decreases exponentially with depth. The N measured by XPS is probably left from unreacted precursor molecules and mostly located at the film surface.

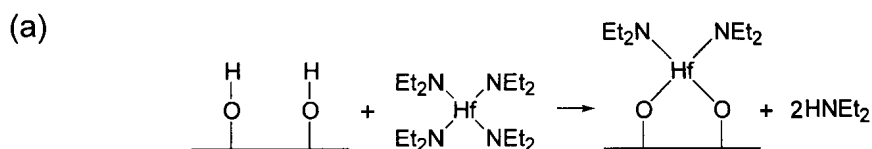
4.2 Reaction mechanism between TDEAH and TMBS

The starting surface of the Si substrate is SiO_x bonded after oxidation. It is not easy for TDEAH or TMBS to adsorb on an oxygen-terminated Si surface due to a dearth of $-\text{OH}$ sites. Thus the growth rate for the first several cycles is low (Fig. 3.8). When the film growth enters a stable regime, after the introduction of the Hf precursor, each TDEAH molecule reacts with two surface hydroxyl groups and eliminates two diethylamine molecules [Fig. 4.8(a)], which is the same reaction mechanism between hafnium alkylamide and surface hydroxyl groups proposed by Liu *et al.* [14]. The TMBS molecule contains a hydroxyl group. In the subsequent half-cycle TMBS pulse, the hydroxyl group in the TMBS molecule cleaves the Hf–N bond on the chemisorbed TDEAH and produces diethylamine molecules as a byproduct [Fig. 4.8(b)]. This reaction step is similar to the reaction between surface chemisorbed tetrakis(ethylmethyldamido)hafnium (TEMAH) and water [14]. Therefore after application of the TMBS precursor, each Hf atom on the surface can bond to two Si atoms via oxygen atoms since there is only one hydroxyl group in each TMBS molecule. Additional TMBS molecules can diffuse down to the surface and insert into the Hf–O bonds by eliminating 2-methyl-2-butanol molecules [Fig. 4.8(c)], because the catalytic activity of Hf atoms lowers the activation energy of this reaction [15]. This reaction may repeat itself as long as the TMBS molecules can

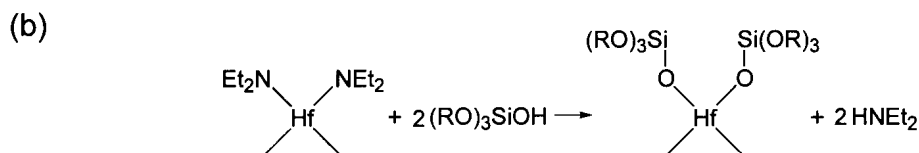
diffuse through the precursor ligands and reach the Hf—O bonds at the surface [Fig. 4.8(d)].

The self-limiting mechanism is achieved by the cross-linking of the Si atoms through O atoms. The 2-methyl-butan-2-olate groups bonded to Si atoms on the surface undergoes thermal decomposition through β -hydrogen elimination of 2-methyl-1-butene [Fig. 4.8(e)], leaving hydroxyl groups on the silicon (similar to Scheme 1E, Ref. [15]). Alternatively, the C—C bond in the 2-methyl-butan-2-olate group can break instead of the C—O bond. As a result, C will be left in the films as an impurity. This explanation is supported by the observed O 1s XPS peak which corresponds to Si—O—C bonding [Fig. 4.1(c)]. A newly formed hydroxyl group may react with a nearby 2-methyl-butan-2-olate group by eliminating a 2-methyl-2-butanol molecule and link the silicon atoms by an oxygen atom [Fig. 4.8(f)] (similar to Scheme 1F, Ref. [15]). The cross-linking between silicon atoms may also be achieved by elimination of H₂O between two adjacent hydroxyl groups [Fig. 4.8(g)] (similar to Scheme 1G, Ref. [15]). The increase of water pressure observed by the RGA shown in Fig. 3.7 confirms this reaction step. In the ideal case, given a sufficiently long time interval following the application of TMBS, all the 2-methyl-butan-2-olate groups either decompose to leave hydroxyl groups on the surface, or react with the near surface hydroxyl groups and eliminate 2-methyl-2-butanol molecules. Therefore when the surface is stabilized following a TMBS pulse, it should be terminated with hydroxyl groups as shown in Fig. 4.8(h).

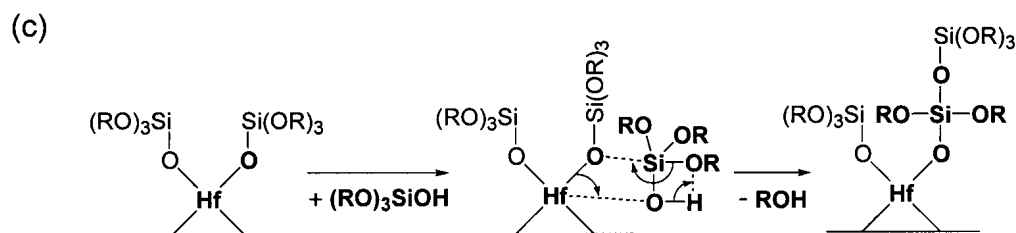
The linear growth rate (after several initial cycles) observed for the films grown in this study is high, 0.33 (± 0.02) nm/cycle according to TEM thickness calibration. Using the relation that $1 \text{ ML} \equiv (N_0 \rho / \text{MW})^{-1/3}$ where N_0 = Avogadro's number, MW = molecular weight and ρ = film density, it was found that $1 \text{ ML} \equiv 0.365 \text{ nm}$ for $\rho = 3.6 \text{ g/cm}^3$ and $\text{Hf}/(\text{Si} + \text{Hf}) = 0.3$. Thus, the linear growth rate shown in Fig. 3.10



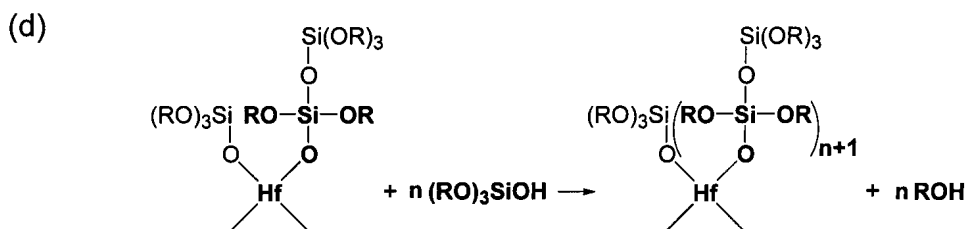
Before TDEAH exposure, the Si surface is terminated with -OH functional groups. After the TDEAH precursor is introduced into the chamber, one TDEAH molecule interacts with two -OH fragments and two diethylamine molecules are eliminated.



After the introduction of the TMBS precursor, the -OH functional group in the TMBS molecule cleaves the N-Hf bond on the film surface. The Si atom in the TMBS molecule is bonded to Hf through an O atom and a diethylamine molecule is eliminated.

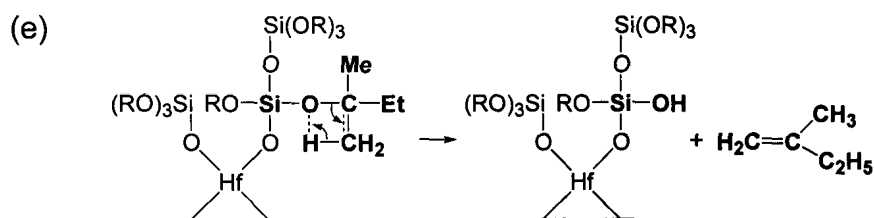


Additional TMBS molecules may diffuse down to the surface and insert into the Hf-O bonds.

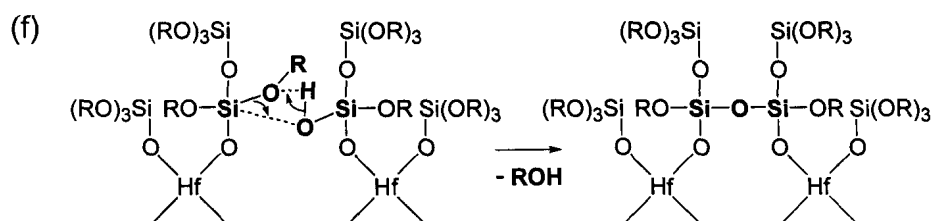


The insertion of a TMBS molecule into the Hf-O bond depicted in (c) may repeat itself until a self-limiting mechanism stops this process.

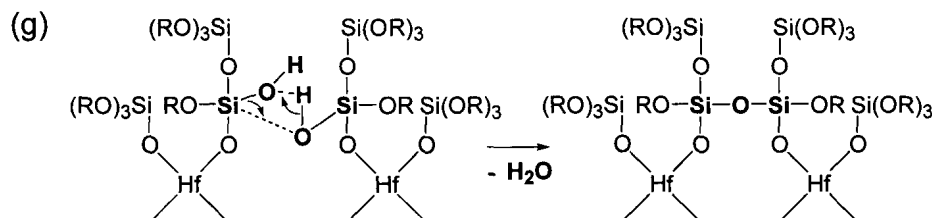
Figure 4.8: Proposed reaction mechanism between TDEAH and TMBS. Me \leftrightarrow $[-CH_3]$ group; Et \leftrightarrow $[-C_2H_5]$ group; R \leftrightarrow $[-C(CH_3)_2C_2H_5]$ group.



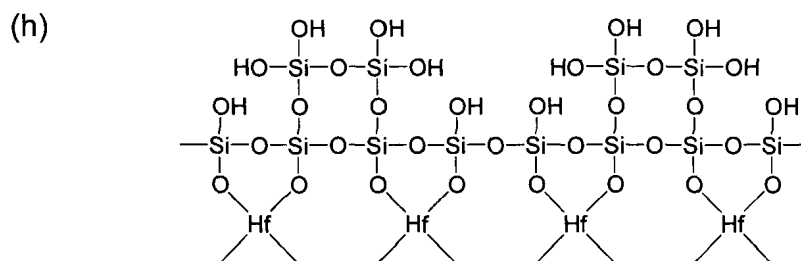
The 2-methyl-but-2-olate group bonded to a Si atom on the film surface thermally decomposes through β -hydrogen elimination of 2-methyl-1-butene, leaving a hydroxyl group on the Si.



A newly-formed hydroxyl group may react with a nearby 2-methyl-but-2-olate group by eliminating a 2-methyl-butanol molecule and linking the Si atoms by an O atom.



The two nearby hydroxyl groups may also react to eliminate a H_2O molecule.



In the ideal case when the possible reactions on the film surface are completed following the application of the TMBS precursor, the surface is once again terminated with hydroxyl groups.

Figure 4.8: Proposed reaction mechanism between TDEAH and TMBS. Me \leftrightarrow $[-\text{CH}_3]$ group; Et \leftrightarrow $[-\text{C}_2\text{H}_5]$ group; R \leftrightarrow $[-\text{C}(\text{CH}_3)_2\text{C}_2\text{H}_5]$ group. (cont.)

corresponds to 1 ML per cycle within experimental uncertainty. This high growth rate cannot be explained by the traditional ALD theory, wherein the growth rate is usually a fraction of a monolayer per cycle due to steric hindrance of the precursor ligands. The above steps describing the diffusion and insertion of silanol precursor into the Hf–O bond mechanism [Figs. 4.8(c) and 4.8(d)] during the application of the silanol precursor can explain the high growth rate observed in this study. This reaction mechanism was first proposed by Hausmann *et al.* [15], who observed abnormally high growth rates (12 nm/cycle) when using trimethylaluminum (Me_3Al) and tris(tert-butoxy)silanol $[(\text{Bu}^t\text{O})_3\text{SiOH}]$ to grow $(\text{Al}_2\text{O}_3)_x\text{--}(\text{SiO}_2)_y$ films by ALD. They conclude that it is the presence of Al atoms that make the catalytic reaction between the surface Al–O bonds and the silanol precursor $(\text{Bu}^t\text{O})_3\text{SiOH}$ possible. Therefore, many Si–O layers can be deposited in one $(\text{Bu}^t\text{O})_3\text{SiOH}$ precursor pulse, resulting in an extremely high growth rate. They also suggest that other metals, such as La, Zr and Hf, should have a similar catalytic activity. Actually, they pointed out that the high growth rate (0.3–0.4 nm/cycle) in their earlier ALD experiment using $\text{Hf}(\text{NMe}_2)_4$ and $(\text{Bu}^t\text{O})_3\text{SiOH}$ to grow Hf silicate films may be due to the same reaction mechanism [16]. The Hf and Si precursors used in Ref. [16] are similar to those used in this study, but those used here are bulkier. The growth rate and the resulting film composition in Ref. [16] are also similar to this study. Although the growth rate of ALD process using TDEAH and TMBS is much higher than that of the traditional ALD, it is much lower than that observed in Ref. [15]. This result is probably because the volume of the TMBS molecule is larger than that of the Si precursor, i.e., $(\text{Bu}^t\text{O})_3\text{SiOH}$, used in Ref. [15]. The bulkier ligands make the diffusion of TMBS molecules [Fig. 4.8(c) and 4.8(d)] more difficult than the diffusion of $(\text{Bu}^t\text{O})_3\text{SiOH}$.

The total film thickness for the growth shown in Fig. 3.7 is 3.4 nm (from ellipsometry). The asymptotic linear growth rate shown in Fig. 3.8 (also based on ellipsometry) is

0.25 nm/cycle. If the film growth were linear from the outset, then it can be calculated that $3.4/0.25 \approx 14$ cycles would be needed to achieve the final thickness. The MEIS data for this same film shown in Table 4.2 can be used to determine that the absolute total Hf areal density [where $\text{Hf}/(\text{Si}+\text{Hf}) = 0.3$ and Layers 2 and 3 were counted] has a value 2.2×10^{15} Hf atoms/cm², or 1.6×10^{14} Hf atoms/cm²/cycle for each of the 14 cycles. If each Hf atom is bonded to two surface $-\text{OH}$ groups, then the surface concentration of those groups is 3.2×10^{14} cm⁻². For the SiO_x thin layer, we can approximate the surface Si atom and therefore $-\text{OH}$ group [in Fig. 4.8(h)] areal densities using $(N_0\rho/\text{MW})^{2/3}$ where we assume SiO_2 ($\text{MW} = 60$) and $\rho = 2.3$ g/cm³, resulting in 4.65×10^{14} cm⁻² – a value in close agreement with that calculated from the observed thickness and growth rate. This calculation lends support to Fig. 4.8 of the proposed reaction mechanism.

The reaction between the Hf precursor, TDEAH, and the hydroxyl group occurs rapidly – an observation that explains the sharp thickness increase following the application of TDEAH evident in both Figs. 3.9 and 3.11. This reaction step is little affected by substrate temperature since it is easy for an $-\text{OH}$ group to break the Hf–N bond. The time needed for TDEAH to saturate an $-\text{OH}$ group terminated surface can be estimated from the partial pressure of TDEAH. When introducing TDEAH into the deposition chamber, the total pressure is 0.43 Pa. The Ar and N₂ flow rates are 50 sccm and 20 sccm, respectively. TDEAH is dissolved in Octane and has a concentration of 0.1 M. The flow rate of Octane is 0.2 ml/min. Therefore the Hf precursor partial pressure is 1.93×10^{-3} Pa. The number of molecules crossing a plane from one side per unit area and unit time, or impingement flux (J), can be calculated from Equation:

$$J = \frac{P}{\sqrt{2\pi mkT}}, \quad (4.3)$$

where P , m , k , and T are the pressure, mass of the molecule, Boltzmann constant and

temperature, respectively. The mass of the TDEAH molecule is 7.754×10^{-25} kg and the chamber temperature is ~ 370 K. Equation 4.3 thus gives $J = 1.2 \times 10^{15} \text{ cm}^{-2} \text{ s}^{-1}$. There are $3.2 \times 10^{14} \text{ cm}^{-2}$ surface $-\text{OH}$ groups that react with TDEAH molecules in one precursor pulse. Gordon *et al.* found that the reaction probability for TDEAH on $-\text{OH}$ surface is at least 7% [17]. Therefore the time needed for TDEAH to saturate the $-\text{OH}$ surface in this study is 3.8 s, which is in good agreement with ellipsometry results.

As already discussed in Chapter 3, the time needed for the TMBS to completely react with the surface is temperature dependent (Fig. 3.12). Obviously, a higher substrate temperature will contribute to a decrease in the reaction time. At lower temperature, an increase in TMBS partial pressure does not help to increase the growth rate (Fig. 3.13). This observation is probably because the decomposition of 2-methyl-butan-2-olate groups [Fig. 4.8(e)] and cross-linking of Si atoms by elimination of 2-methyl-2-butanol molecules [Fig. 4.8(f)] occur faster at higher temperature.

4.3 Summary

A growth rate of ~ 1 ML per cycle was observed in the ALD growth of Hf silicate films using precursors TDEAH and TMBS. This growth rate is much higher than the growth rate normally observed in ALD, which can be explained by the catalytic reaction between the Hf–O bonds and silanol precursors.

The composition of Hf silicate films grown by ALD were measured by XPS and MEIS. The nitrogen impurity was also investigated by NRA. The film composition, i.e., Hf/(Hf+Si) value, can be varied only in a small range (0.22–0.30) because of the self-limiting mechanism of ALD. Carbon contamination can be reduced to $< 1\%$

by performing an in situ anneal at 800°C for ~ 2 s according to the in situ XPS data. The small amount of Hf carbide impurities can be oxidized in atmosphere at room temperature. The concentration of nitrogen impurities is quite small, $\sim 1/6$ ML, because the Hf–N bonds in the TDEAH precursor can be easily broken by –OH functional group. In the case of film growth by ALD using TDEAH and TMBS, the impurities can be controlled within a reasonably small range.

BIBLIOGRAPHY

- [1] R. Flitsch and S. I. Raider, *J. Vac. Sci. Technol.* **12**, 305 (1975).
- [2] Z. H. Lu, J. P. McCaffrey, B. Brar, G. D. Wilk, R. M. Wallace, L. C. Feldman, and S. P. Tay, *Appl. Phys. Lett.* **71**, 2764 (1997).
- [3] M. D. Ulrich, J. G. Hong, J. E. Rowe, G. Lucovsky, A. S.-Y. Chan, and T. E. Madey, *J. Vac. Sci. Technol. B* **21**, 1777 (2003).
- [4] M.-H. Cho, Y. S. Roh, C. N. Whang, K. Jeong, S. W. Nahm, D.-H. Ko, J. H. Lee, N. I. Lee, and K. Fujihara, *Appl. Phys. Lett.* **81**, 472 (2002).
- [5] H. D. Kim, Y. Roh, Y. Lee, J. E. Lee, D. Jung, and N.-E. Lee, *J. Vac. Sci. Technol. A* **22**, 1347 (2004).
- [6] R. O'Connor, G. Hughes, P.-A. Glans, T. Learmonth, and K. Smith, *Appl. Surf. Sci.* **253**, 2770 (2006).
- [7] S. X. Lao, R. M. Martin, and J. P. Chang, *J. Vac. Sci. Technol. A* **23**, 488 (2005).
- [8] R. Hofman, J. G. F. Westheim, I. Pouwel, T. Fransen, and P. J. Gellings, *Surf. Interface Anal.* **24**, 1 (1996).
- [9] L. Ramqvist, K. Hamrin, G. Johansson, A. Fahlman, and C. Nordling, *J. Phys. Chem. Solids* **30**, 1835 (1969).
- [10] B.-O. Cho, S. Lao, L. Sha, and J. P. Chang, *J. Vac. Sci. Technol. A* **19**, 2751 (2001).
- [11] N. Barrett, O. Renault, P. Besson, Y. L. Tiec, F. Martin, and F. Calvat, *Microelectron. Eng.* **84**, 2302 (2007).
- [12] The QUARK simulation for elastic scattering is available at the website of W. N. Lennard: www.uwo.ca/isw/people.
- [13] D. M. Hausmann, E. Kim, J. Becker, and R. G. Gordon, *Chem. Mater.* **14**, 4350 (2002).
- [14] X. Liu, S. Ramanathan, A. Longdergan, A. Srivastava, E. Lee, T. E. Seidel, J. T. Barton, D. Pang, and R. G. Gordon, *J. Electrochem. Soc.* **152**, G213 (2005).

- [15] D. Hausmann, J. Becker, S. Wang, and R. G. Gordon, *Science* **298**, 402 (2002).
- [16] R. G. Gordon, J. Becker, D. Hausmann, and S. Suh, *Chem. Mater.* **13**, 2463 (2001).
- [17] R. G. Gordon, D. Hausmann, E. Kim, and J. Shepard, *Chem. Vapor Depos.* **9**, 73 (2003).

CHAPTER 5

FILM STRUCTURE¹

The dielectric properties of a thin film are dependent on the film structure. As already pointed out, amorphous uniform thin films are desired in CMOS transistors because the grain boundaries in polycrystalline structures can serve as charge conduction paths [1]. However, it has been reported that phase separation occurs in the $(\text{HfO}_2)_x(\text{SiO}_2)_{1-x}$ and $(\text{ZrO}_2)_x(\text{SiO}_2)_{1-x}$ systems with $x = 15\text{--}80\%$ during the typical dopant activation temperature with the attendant crystallization of ZrO_2 or HfO_2 [2–4]. Simulations for thermodynamic properties were carried out for the $\text{ZrO}_2\text{--SiO}_2$ system because of the wealth of experimental data that exists for this system [3, 5]. It is expected that the simulation results are qualitatively applicable to the $\text{HfO}_2\text{--SiO}_2$ system due to the similarity of the chemical properties of Hf and Zr silicates. Kim and McIntyre calculated the metastable extensions of the miscibility gap and spinodal of the $\text{ZrO}_2\text{--SiO}_2$ system based on the available phase diagrams, and predicted that, upon rapid thermal annealing at conventional device processing temperatures, the $(\text{ZrO}_2)_x(\text{SiO}_2)_{1-x}$ system with composition in the spinodal ($x = 0.1\text{--}0.6$) will phase separate into two phases having compositions given by the metastable extensions of

¹A version of this chapter has been published. J. Liu, X. Wu, W. N. Lennard and D. Landheer, Phys. Rev. B **80**, 041403 (2009)

the miscibility gap [5]. They further simulated the effect of the interface between the Si substrate and the $(\text{ZrO}_2)_x(\text{SiO}_2)_{1-x}$ films on the spinodal decomposition, and predicted a composition wave normal to the substrate surface. This composition wave then decays when propagating into the bulk of the film. However, such a spinodal composition wave in solid films has never been reported by other groups. In this chapter, the observation of surface-directed spinodal decomposition in $(\text{HfO}_2)_x(\text{SiO}_2)_{1-x}$ films, with $x \approx 0.25$ which is in the predicted spinodal range of the $\text{Zr}(\text{Hf})\text{O}_2\text{-SiO}_2$ system, will be discussed.

5.1 Surface-directed spinodal decomposition

Considering a homogeneous binary mixture $A_{1-x}B_x$, Figure 5.1 shows its molar free energy, G_m , as a function of composition at three different temperatures, $T_1 < T_C < T_2$. At T_1 , the inflection points, P and Q , at which $\partial^2 G_m / \partial x^2 = 0$, separate the regions of stability and instability (with respect to small composition fluctuations) and are called spinodal points. When passing through the spinodal points, the curvature of the free energy curve changes from positive to negative or from negative to positive. In the range $x_P < x < x_Q$, $\partial^2 G_m / \partial x^2 < 0$ and the system is not stable since any small fluctuation results in a lower system free energy. Thus the system would decompose spontaneously through diffusion until the lowest free energy is achieved. The resulting system is a two-phase mixture with compositions given by the common tangent (points M and N in Fig. 5.1) [6]. This decomposition of a homogeneous solution resulting from infinitesimal fluctuations is called spinodal decomposition [7]. As the temperature increases from T_1 to T_2 , the region of instability shrinks until it vanishes at a temperature which is called the critical temperature T_C . At this temperature, $\partial^3 G_m / \partial x^3 = \partial^2 G_m / \partial x^2 = 0$ and all four points M , N , P and Q merge into a single critical point, C [7]. A curve connecting the spinodal points at differ-

ent temperatures is called the spinodal line (Fig. 5.2). The miscibility gap defines the stable phases at each temperature. Phase separation of a binary mixture with composition in the spinodal range, $x_P < x < x_Q$ at T_1 in Fig. 5.2, occurs via the spinodal mechanism while for a system with composition in the metastable region, $x_M < x < x_P$ and $x_Q < x < x_N$ at T_1 , phase separation occurs via a nucleation and growth mechanism [6].

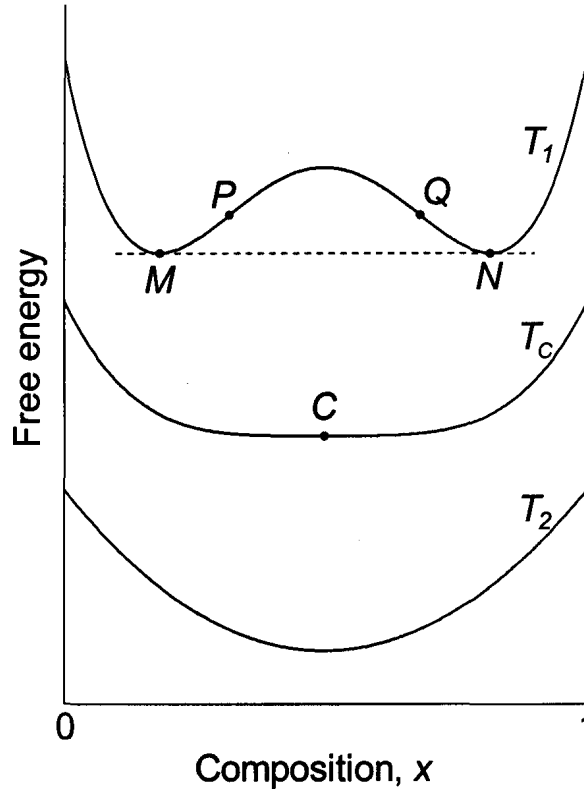


Figure 5.1: Typical temperature dependence of the free energy of a system presenting a miscibility gap ($T_1 < T_c < T_2$).

Spinodal decomposition has been widely investigated [6, 8–11]. In the bulk of a binary mixture which experiences spinodal decomposition, the composition fluctuation results in a random, isotropic microstructure comprised of phase regions enriched in either component [8–10]. The average size of the single-phase domains then grows with time, which corresponds to the coarsening of the structure [9, 10, 12]. Recently, it has been recognized that in thin films where the translational and rotational sym-

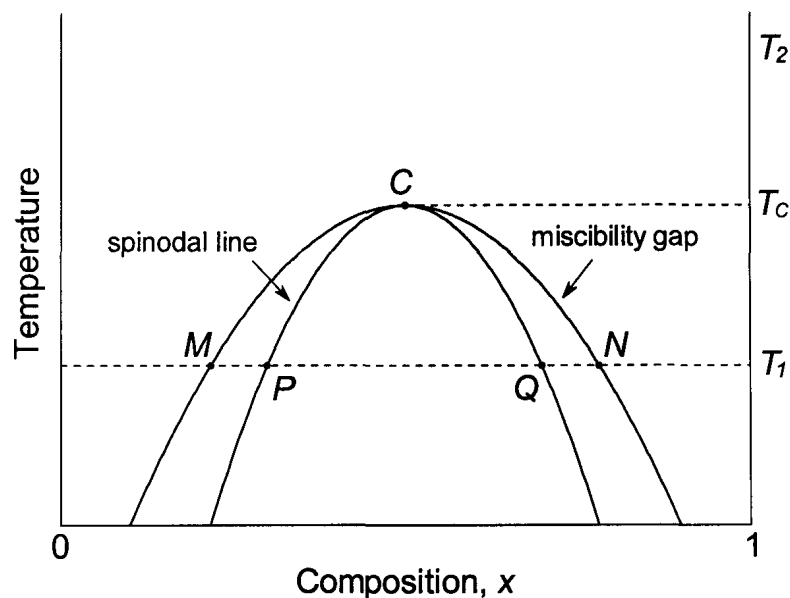


Figure 5.2: Example of a miscibility gap and a spinodal line.

metries are broken due to the presence of interfaces or free surfaces, spinodal decomposition may interact with wetting phenomena resulting in a very different structure at the film boundaries compared to the bulk behaviour, which has been referred to as surface-directed spinodal decomposition (SDSD) [13–18]. The SDSD simulations [13, 18–20] show that a composition wave perpendicular to the surface forms at the surface due to the preferential attraction of the surface to one of the two components. This wave then propagates into the bulk of the film and decays because of thermal noise [21]. Most experimental studies in SDSD have been carried out in polymer mixtures where the associated phase diagrams can be tailored and a small self-diffusion coefficient slows the spinodal decomposition dynamics [15–17]. While it is predicted that spinodal decomposition could occur generally in any two-component system whose phase diagram shows a miscibility gap, such as $\text{ZrO}_2\text{-SiO}_2$, $\text{HfO}_2\text{-SiO}_2$, $\text{La}_2\text{O}_3\text{-SiO}_2$, $\text{Y}_2\text{O}_3\text{-SiO}_2$ [5] and $\text{Al}_2\text{O}_3\text{-SiO}_2$, few observations of SDSD in these systems have been reported.

5.2 Surface-directed spinodal decomposition in Hf silicate films

In this study, films with thicknesses in the range 4–20 nm were grown at 350 °C. The time required to grow a film varied in the range 0.5–2 hours depending on the ultimate film thickness. The Hf profiles in both the as-grown and annealed films were characterized by HRTEM and HAADF-STEM. The HRTEM and HAADF-STEM images are referred to as bright field (BF) and dark field (DF) images, respectively. Film compositions near the surface were investigated by ARXPS using monochromatic Al $K\alpha$ x rays. The MEIS studies were also performed to study the Hf profile in the as-grown and annealed thin films. An ex situ rapid thermal anneal (RTA) was subsequently performed in N₂ at 800 °C for 6 seconds.

5.2.1 Structure of the as-grown films

Figures 5.3(a) and 5.3(c) show the BF and DF images of a 5.3 nm as-grown film. In Fig. 5.3(a), the darker area near the surface indicates a region of higher Hf concentration relative to the brighter area close to the substrate. The contrast in Fig. 5.3(c) is reversed relative to 5.3(a) such that the DF image is more sensitive to the atomic number of the constituent atoms. Both images confirm the Hf-rich top region and the Hf-deficient (i.e., Si-rich) bottom region of the film. Figure 5.3(b) shows the line intensity profile integrated over the width of the rectangle shown in 5.3(a). This profile represents the Hf distribution in the direction normal to the substrate surface. A lower intensity region in Fig. 5.3(b) corresponds to a higher Hf concentration. Figure 5.3(b) clearly shows a wave like Hf distribution throughout the film. The 5.3 nm film separates into two layers with the layer closer to the substrate Si-rich and the layer closer to the surface Hf-rich. This observation is qualitatively in agreement with the MEIS simulation results [Fig. 4.6(b)]. The TEM images of

thinner as-grown films (4 nm) show a similar structure, see Fig. 5.4.

Figures 5.5(a) and 5.5(c) show the BF and DF images of a 6.1 nm as-grown film. Figure 5.5(b) shows the line intensity profile integrated over the width of the rectangle shown in 5.5(a). As can be seen from Figs. 5.5(a) and 5.5(b), the 6.1 nm as-grown film separates into four layers, starting from the substrate: Si-rich, Hf-rich, Si-rich and Hf-rich. The line intensity profile for this film [Fig. 5.3(b)] shows that the Hf-rich layer closer to the substrate has lower Hf concentration than the Hf-rich layer closer to the film surface. The Hf concentration difference in these two layers cannot be resolved from the DF image [Fig. 5.5(c)].

As the film thickness increases to 12.5 nm, the layered structure can hardly be identified in the BF image [Fig. 5.6(a)]. The line intensity profile [Fig. 5.6(b)] shows that there are Hf-rich layers close to the surface and the interface. The DF image of this film [Fig. 5.6(c)] shows that there is a Si-rich layer on the substrate. This layer is followed by a Hf-rich layer. The layer at the surface is Hf rich. In the center of the film, Hf-rich clusters are mixed with Si-rich clusters.

The distances of the first Hf-rich layers from the substrates in Figs. 5.4(b), 5.3(b), 5.5(b) and 5.6(b) are 3, 3.5, 1.9 and 1.5 nm, respectively. It can be concluded that as the film thickens beyond 5 nm, some of the Hf atoms in the Hf-rich layer closer to the film surface diffuse toward the substrate. As already specified, the interface Si thermal oxide is <0.5 nm thick. Therefore, the Hf-deficient layer close to the substrate in Figs. 5.3 and 5.4 is not all thermal SiO₂ since its thickness is too large, i.e., significantly >0.5 nm, and it is a Si-rich layer of the film.

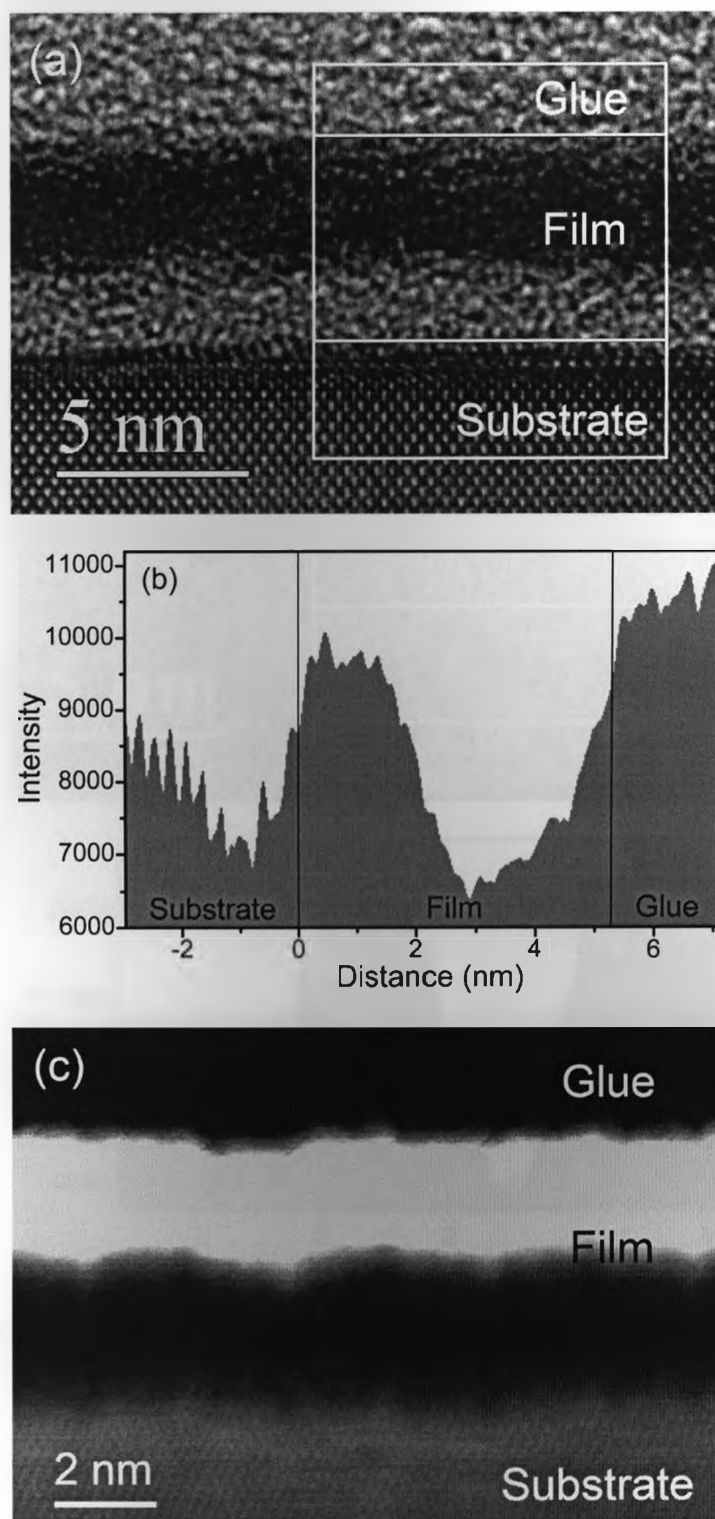


Figure 5.3: (a) BF image of a 5.3 nm as-grown film; (b) line intensity profile integrated over the width of the rectangle shown in (a); (c) DF image of the 5.3 nm as-grown film.

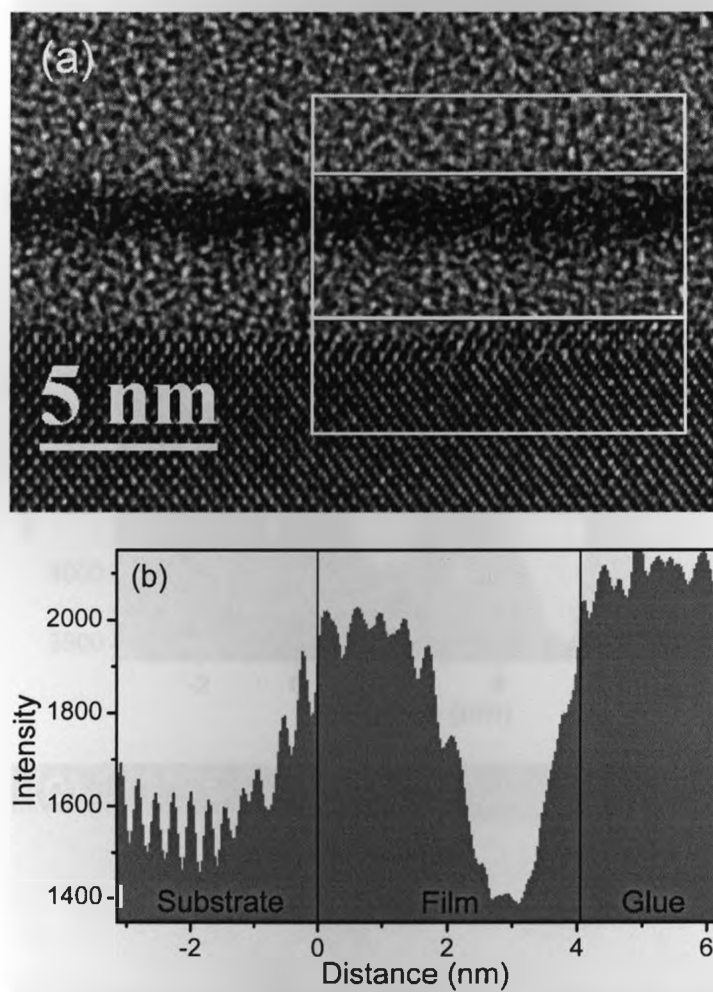


Figure 5.4: (a) BF image of a 4 nm as-grown film; (b) line intensity profile integrated over the width of the rectangle shown in (a).

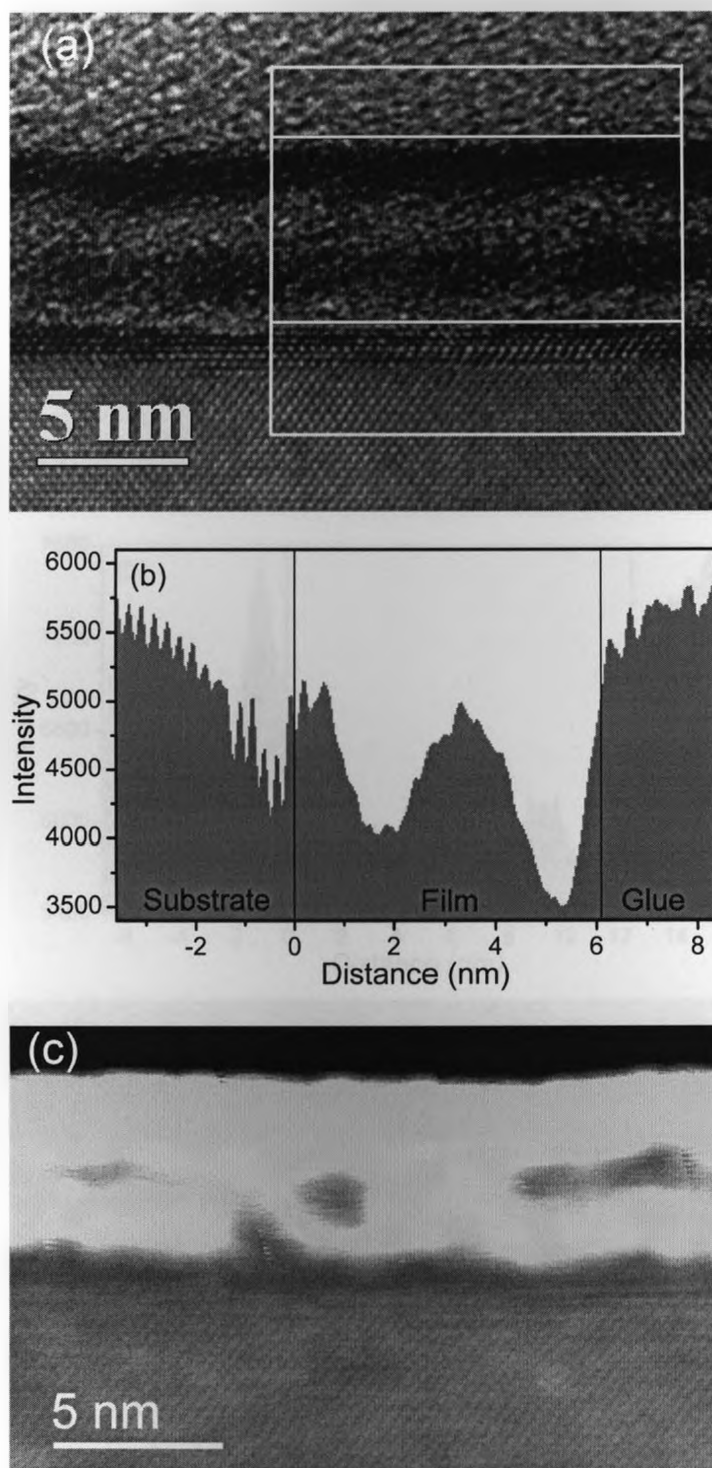


Figure 5.5: (a) BF image of a 6.1 nm as-grown film; (b) line intensity profile integrated over the width of the rectangle shown in (a); (c) DF image of the 6.1 nm as-grown film.

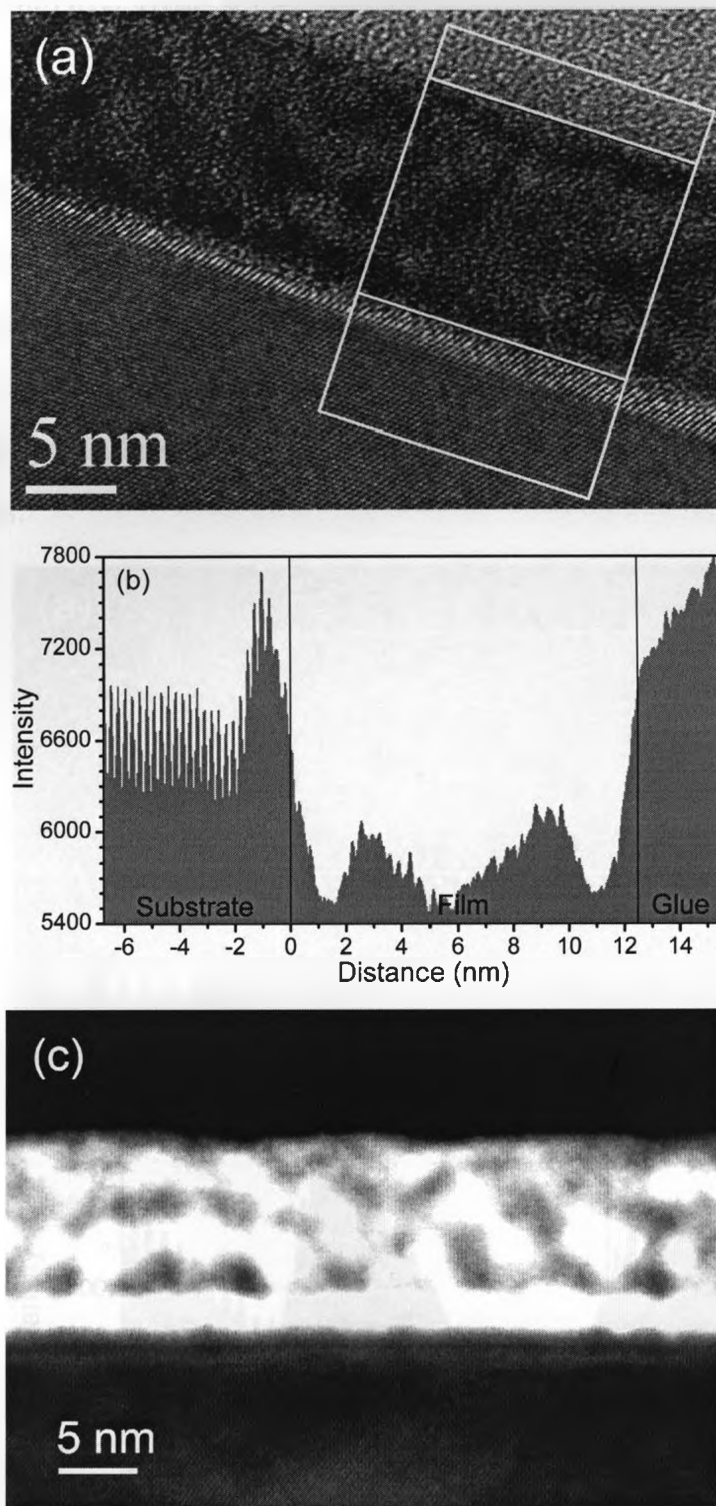


Figure 5.6: (a) BF image of a 12.5 nm as-grown film; (b) line intensity profile integrated over the width of the rectangle shown in (a); (c) DF image of the 12.5 nm as-grown film.

5.2.2 Film structure after RTA

Figures 5.7(a) and 5.7(c) show the BF and DF images of the 5.3 nm film shown in Fig. 5.3 after RTA. The thickness of this film decreases slightly after annealing due to the densification process during annealing. Still the film is comprised of two layers with the layer closer to the substrate Si-rich. The line intensity profile [Fig. 5.7(b)] shows a change of Hf distribution with respect to the profile shown in [Fig. 5.3(b)] for the as-grown film, indicating an interdiffusion of the Hf and Si atoms during the annealing process.

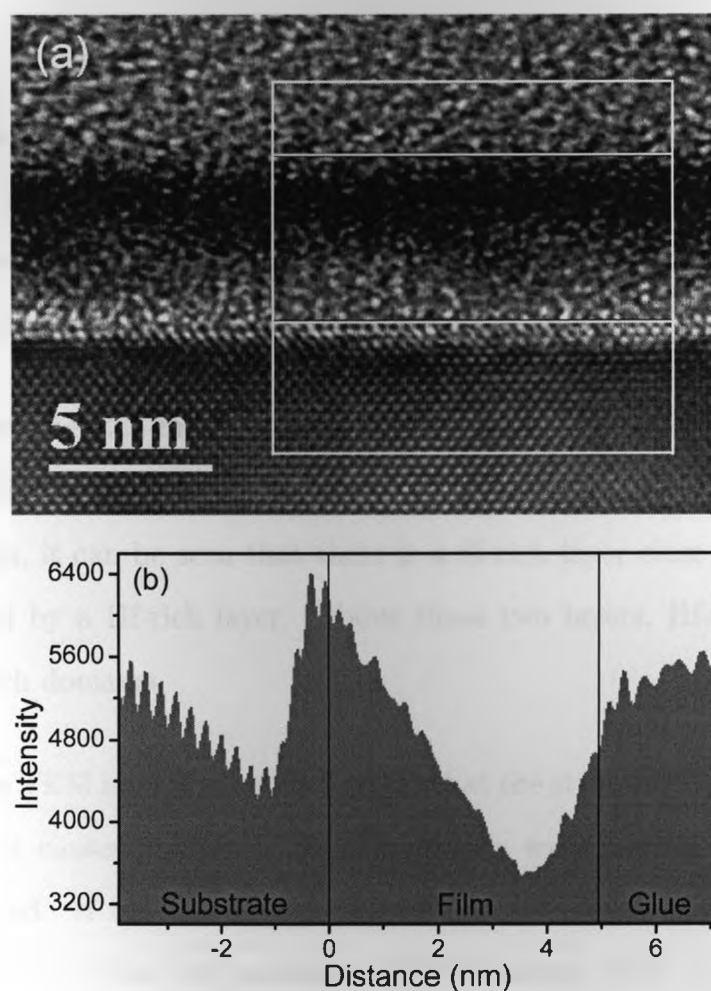


Figure 5.7: (a) BF image of the 5.3 nm film after RTA; (b) line intensity profile integrated over the width of the rectangle shown in (a).

Figures 5.8(a) and 5.8(c) show the BF and DF images of the 6.1 nm film (Fig. 5.5) after RTA. Figure 5.8(b) shows the line intensity profile integrated over the rectangle shown in 5.8(a). Comparing Fig. 5.8 to Fig. 5.5, it can be concluded that after RTA: (i) the film thickness decreases to 5.9 nm due to densification, (ii) some of the Hf atoms in the Hf-rich layer closer to the film surface diffuse to the Hf-rich layer closer to the substrate after RTA, and (iii) the distance between the first Hf-rich layer and the substrate decreases. After RTA, the 6.1 nm film separates into three layers: a Si-rich layer sandwiched between two Hf-rich layers. It is believed that the 0.5 nm thick interface layer in Fig. 5.8 is Si thermal oxide formed during the substrate oxidation process.

Figures 5.9(a) and 5.9(b) show the BF image and the corresponding line intensity profile of a film after RTA. This film is 6.9 nm thick after RTA, 1 nm thicker than the film shown in Fig. 5.8 and it consists of four layers, starting from the substrate: Si-rich, Hf-rich, Si-rich and Hf-rich layers.

Figure 5.10 shows the 12.5 nm film (Fig. 5.6) after RTA. The layered structure can hardly be identified in Figs. 5.10(a) and 5.10(b). From Fig. 5.10(c) showing the DF image of this film, it can be seen that there is a Si-rich layer close to the substrate, which is followed by a Hf-rich layer. Above these two layers, Hf-rich domains are mixed with Si-rich domains.

The above shown TEM images strongly suggest that the structure of these $(\text{HfO}_2)_{0.25}$ - $(\text{SiO}_2)_{0.75}$ films is caused by SDS. A composition wave normal to the substrate surface is observed. If the composition wavelength, λ_C , is defined as the distance between the centers of the two successive Hf-rich layers, then λ_C measured from TEM images [Figs. 5.8(b) and 5.9(b)] is ~ 4 nm. If the film is thinner than 8 nm (i.e., $2\lambda_C$), a layered structure is observed via TEM throughout the entire film: the

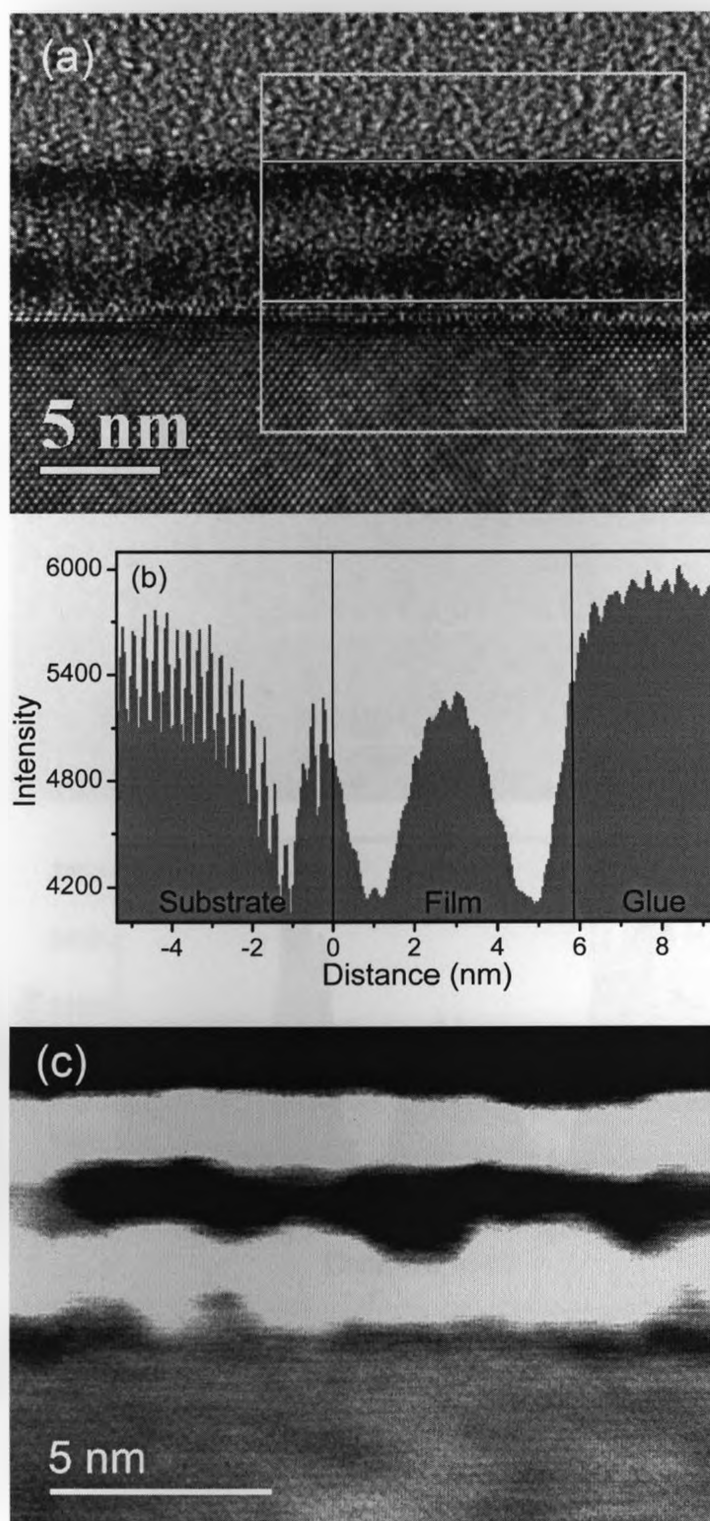


Figure 5.8: (a) BF image of the 6.1 nm film after RTA; (b) line intensity profile integrated over the width of the rectangle shown in (a); (c) DF image of the 6.1 nm film after RTA.

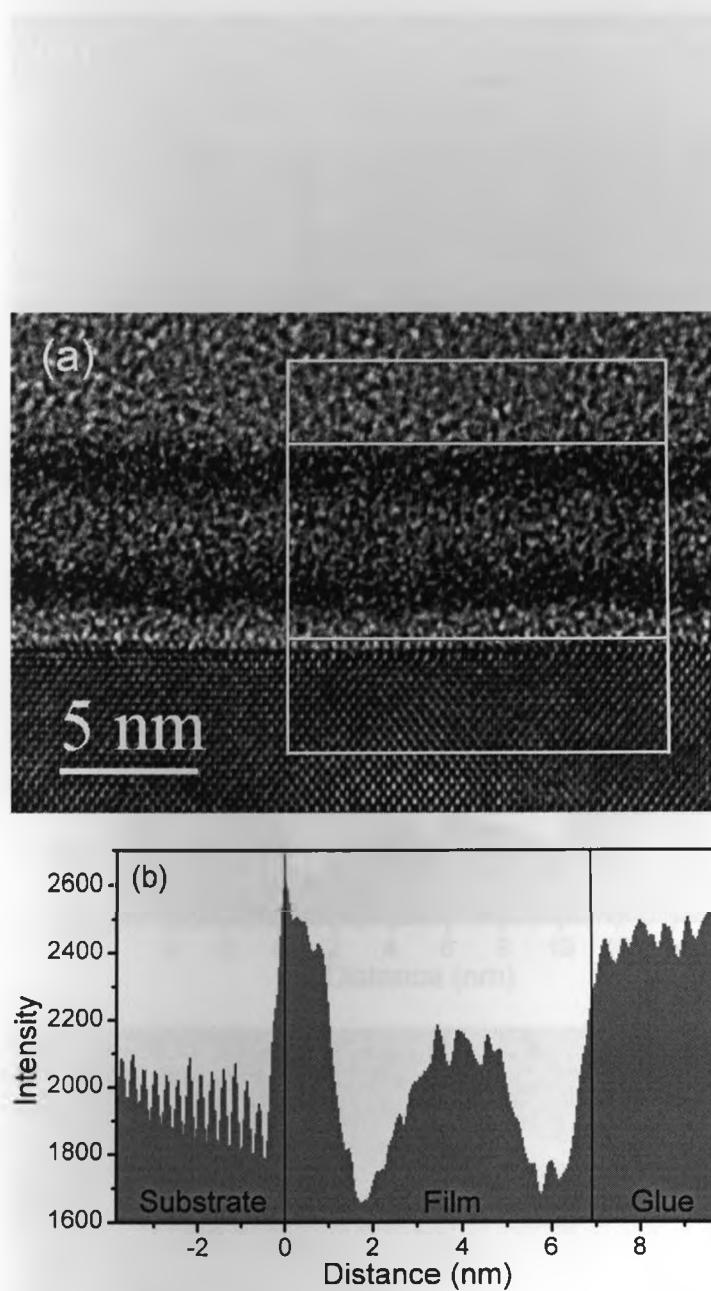


Figure 5.9: (a) BF image of a ~ 6.9 nm film after RTA; (b) line intensity profile integrated over the width of the rectangle shown in (a).

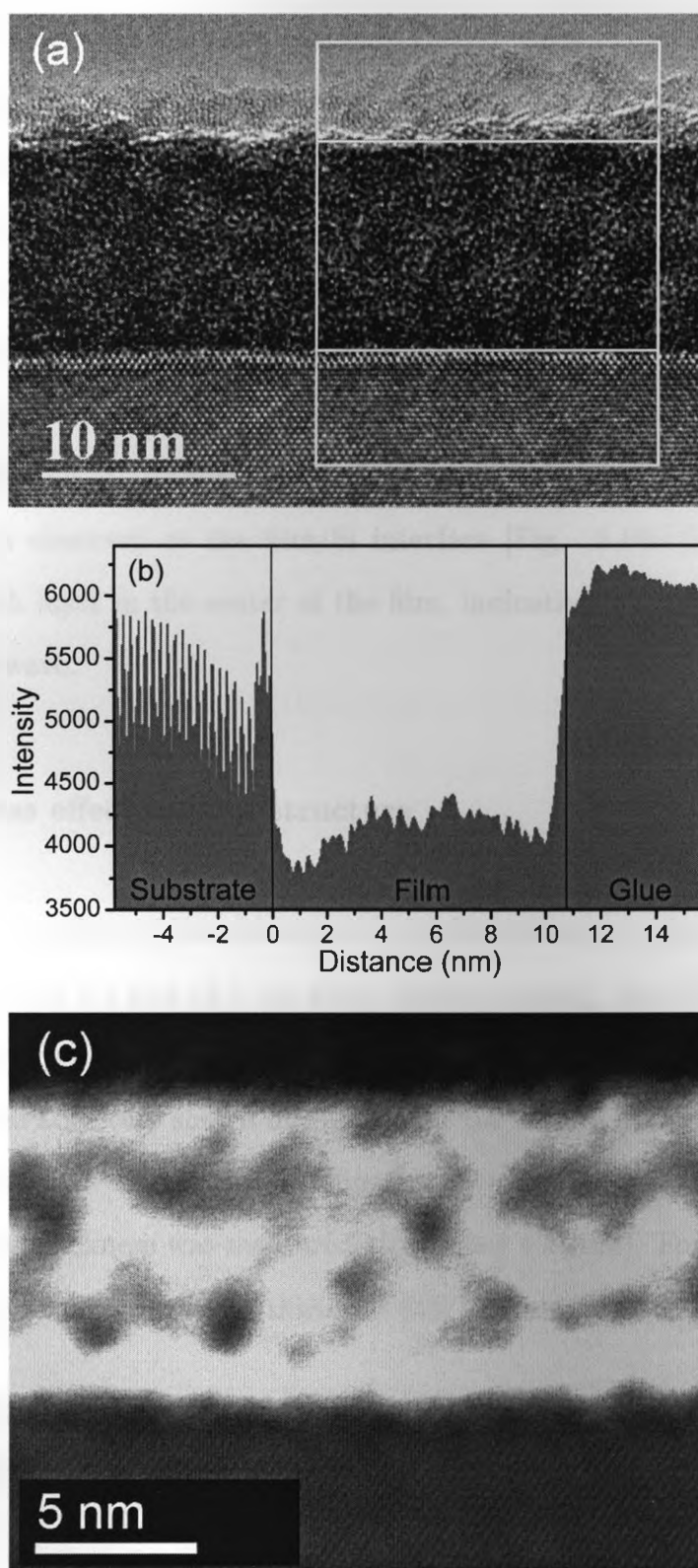


Figure 5.10: (a) BF image of the 12.5 nm film after RTA; (b) line intensity profile integrated over the width of the rectangle shown in (a); (c) DF image of the 12.5 nm film after RTA.

surface layer is Hf rich and the layer closest to the interface Si oxide can be Si rich or Hf rich depending on the film thickness. If the film thickness is λ_C or $2\lambda_C$, the layer closest to the interface is Si rich. If the film thickness is $1.5\lambda_C$, the layer closest to the interface is Hf rich. This result is rather surprising because the $(\text{HfO}_2)_{0.25}(\text{SiO}_2)_{0.75}$ films were grown on a very thin layer of Si thermal oxide. The Si-rich component in these films should have a lower interface energy with the interfacial Si thermal oxide layer. Therefore, it was expected that the film layer closest to the interface should always be a Si-rich layer. As the film thickens to $>2\lambda_C$, a Si-rich layer followed by a Hf-rich layer is observed at the film/Si interface [Fig. 5.10(c)] and there is no continuous Hf-rich layer in the center of the film, indicating a tendency for decay of the composition wave.

5.2.3 Thickness effect on film structure

To further study the effect of film thickness on the film structure, dilute HF (0.4%) was used to etch back the 6.1 and 12.5 nm films. Before etching, the $(\text{HfO}_2)_{0.25}(\text{SiO}_2)_{0.75}$ films were subjected to the usual RTA process to reduce the etching rate [22] and to achieve the layered structure shown in Fig. 5.8 for the 6.1 nm film. After etching, the RTA step was repeated. Spectroscopic ellipsometry was used to monitor the etching rate, (i.e., the film thickness was measured after every 4 s etch). For the 6.1 nm film, XPS was also used to measure film thickness [23] before and after HF etch.

The overlayer Si oxide thickness d on the Si substrate can be calculated by measuring the Si 2p intensity ratio [24]:

$$d = \lambda_f \sin \theta \ln \left[\frac{I_f}{\beta I_s} + 1 \right] \quad (5.1)$$

where λ_f is the photoelectron attenuation length in the oxide film, θ is the photoelec-

tron takeoff angle, β is the ratio of the Si 2p intensities from the infinitely thick oxide and substrate, and I_f and I_s are the Si 2p intensity from the film and the substrate, respectively. Using Equation 5.1, the ratio of the film thicknesses before and after HF etch can be calculated without the knowledge of λ_f :

$$\frac{d_{before\ etch}}{d_{after\ etch}} = \frac{\ln[I_f/(\beta I_s) + 1]_{before\ etch}}{\ln[I_f/(\beta I_s) + 1]_{after\ etch}}. \quad (5.2)$$

Using the above equation, the ratio of film thicknesses before and after RTA can also be calculated. The Si 2p XPS intensities of the annealed 6.1 nm film before and after HF etch are shown in Fig. 5.11. Figure 5.12 shows the Si 2p peaks of the HF etched film before and after RTA. The intensities of the Si 2p signals from the films and substrates are listed in Table 5.1. Substituting the intensities into Equation 5.2, the ratio of the film thicknesses before and after HF etching is $d_{before\ etch}/d_{after\ etch} = 1.5$. The film thickness measured from the TEM image before etch is 6.1 nm. Therefore, the film is 4 nm thick after etch. The ratio of film thicknesses before and after RTA is $d_{before\ RTA}/d_{after\ RTA} = 0.84$. From Fig. 5.13(a), the thickness of the etched film after RTA is 5 nm. Therefore, the thickness of the film before RTA can be calculated as 4.2 nm, which is in good agreement with the calculated thickness after HF etch. In the above calculation, $\beta = 0.7$ is assumed. Values for β reported in the literature vary from 0.67 to 0.87 for a SiO₂ film [25]. Varying β from 0.5 to 0.8 results in a ratio difference of $\sim 1\%$ in Equation 5.2. Therefore, the assumption is valid.

Table 5.1: Si 2p XPS peak intensities.

Sample	XPS peak intensity	
	Si ⁴⁺ 2p	Si ⁰ 2p
Before HF etch	5431.9	2084.6
After HF etch	4782.2	3724.6
Before RTA	19972.8	6979.8
After RTA	17609.4	4284.8

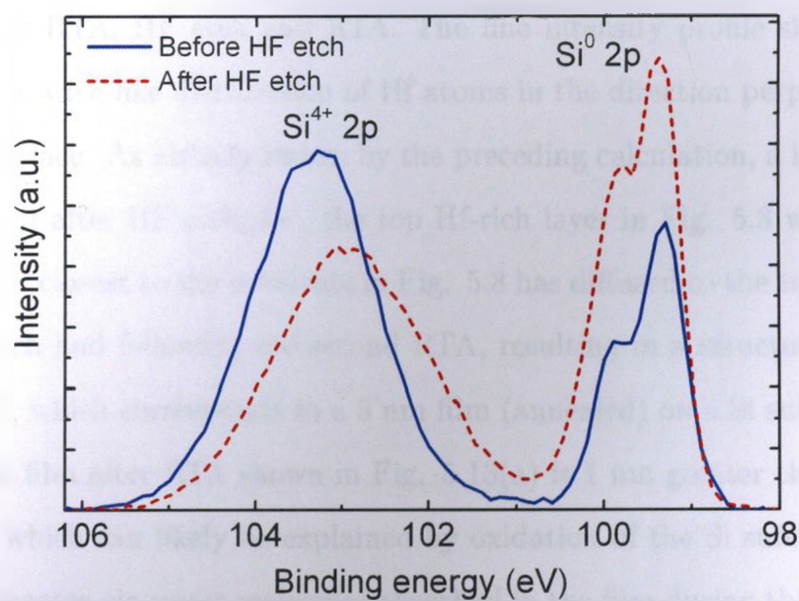


Figure 5.11: Si 2p XPS peaks of the 6.1 nm film before and after HF etch.

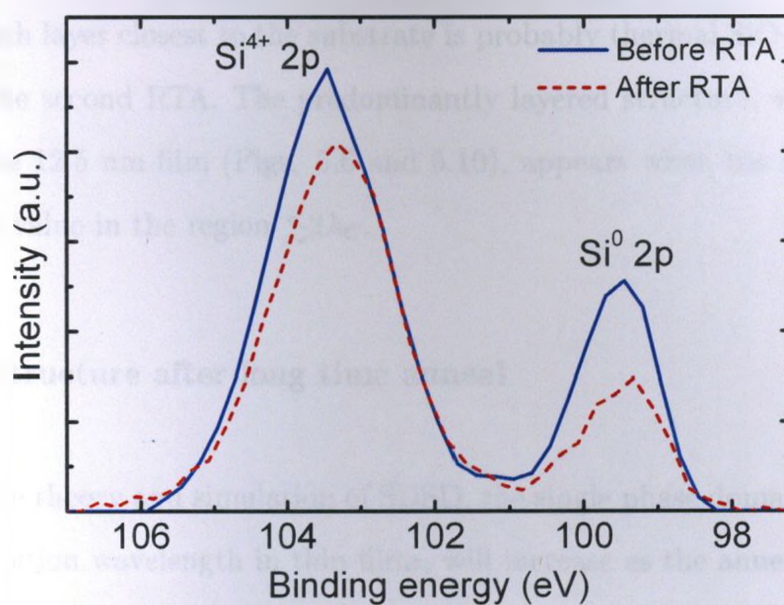


Figure 5.12: Si 2p XPS peaks of the HF etched 6.1 nm film (Fig. 5.11) before and after RTA.

Figures 5.13(a) and 5.13(c) show the BF and DF images of the 6.1 nm film shown in Fig. 5.5 after RTA, HF etch and RTA. The line intensity profile shown in Fig. 5.13(b) reveals a wave-like distribution of Hf atoms in the direction perpendicular to the substrate surface. As already shown by the preceding calculation, a layer of 2 nm film was removed after HF etch, i.e., the top Hf-rich layer in Fig. 5.8 was removed. The Hf-rich layer closest to the substrate in Fig. 5.8 has diffused to the top of the film after the HF etch and following the second RTA, resulting in a structure similar to that in Fig. 5.7, which corresponds to a 5 nm film (annealed) on a Si substrate. The thickness of the film after RTA shown in Fig. 5.13(a) is 1 nm greater than expected after HF etch, which can likely be explained by oxidation of the Si substrate during the annealing process via water molecules absorbed in the film during the HF etching process.

Figures 5.14(a) and 5.14(b) show the BF image and the corresponding line intensity profile for the 12.5 nm film (Fig. 5.6) after RTA, HF etch (removing ~ 6 nm) and RTA. The Si-rich layer closest to the substrate is probably thermal SiO_2 formed after HF etch and the second RTA. The predominantly layered structure, which was not observed for the 12.5 nm film (Figs. 5.6 and 5.10), appears when the film thickness is reduced to a value in the region $\lesssim 2\lambda_C$.

5.2.4 Film structure after long time anneal

According to the theory and simulation of SDSD, the single phase domain, and therefore the composition wavelength in thin films, will increase as the annealing time increases, which corresponds to a coarsening of the phase separated structures [5, 26]. In order to search for this phenomenon in Hf silicate films, longer time anneals were performed for the 6.1 nm and 12.5 nm films. Figure 5.15 shows the BF image, line

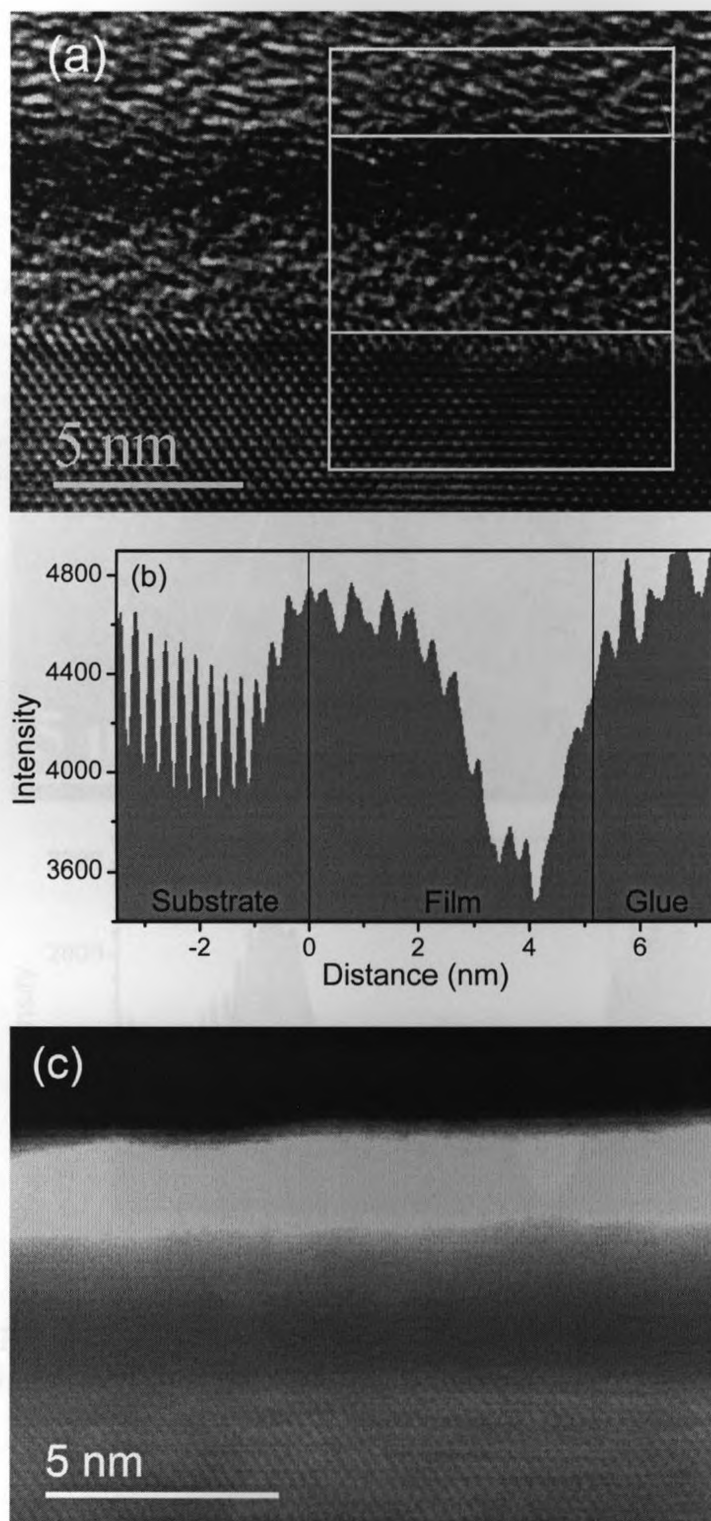


Figure 5.13: (a) BF image of the 6.1 nm film after RTA, HF etch and RTA; (b) line intensity profile integrated over the width of the rectangle shown in (a); (c) DF image of the 6.1 nm film after RTA, HF etch and RTA.

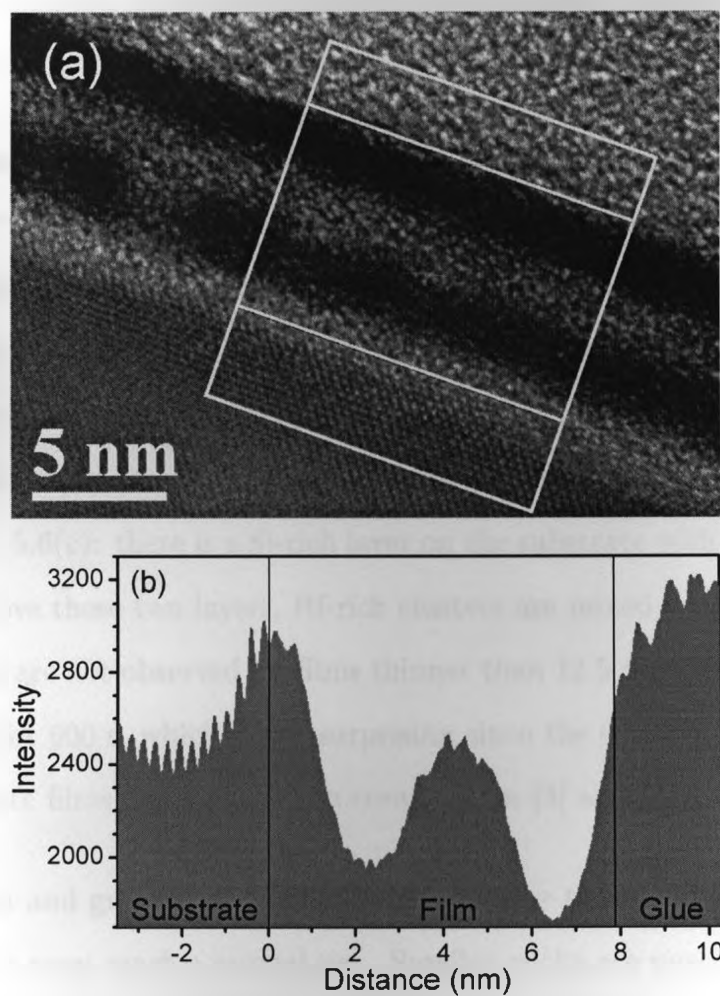


Figure 5.14: (a) BF image of the 12.5 nm film after RTA, HF etch and RTA; (b) line intensity profile integrated over the width of the rectangle shown in (a).

intensity profile and DF image of the 6.1 nm film after a 600 s anneal at 800 °C in N₂. Only one Hf-rich layer and one Si-rich layer are observed in Fig. 5.15 indicating a growth of single-phase regions during a longer time anneal. The thickness of this film has increased by ~2 nm compared to the thickness after RTA (Fig. 5.8) as a result of diffusion of the O₂ impurity in N₂ to the interface where oxidation of the substrate occurs [27].

Figure 5.16 shows the BF and DF images of the 12.5 nm films (Fig. 5.6) after 600 s anneal at 800 °C in N₂. Comparing to the film thickness after RTA (Fig. 5.10), it can be concluded that a ~3 nm thick layer of thermal SiO₂, i.e., almost all the Si-rich layer close to the substrate in Fig. 5.16(a), has grown during the 600 s anneal. HfO₂ crystallites were observed in this film indicating that nucleation and growth occurred after spinodal decomposition during the annealing process. The DF image of this film is similar to Fig. 5.6(c): there is a Si-rich layer on the substrate with a ~2 nm Hf-rich layer on top; above these two layers, Hf-rich clusters are mixed with Si-rich clusters. HfO₂ crystallites are not observed for films thinner than 12.5 nm even after an anneal at 800 °C in N₂ for 600 s, which is not surprising since the onset of crystallization of HfO₂ in Hf silicate films depends on film composition [3] and thickness [28].

In the nucleation and growth mechanism, for a nucleus to be stable with respect to further growth, it must reach a critical size. Smaller nuclei are unstable and may dissolve because of surface energy effects and their large surface to volume ratio. Therefore the nucleation and growth process is suppressed in thinner films and a higher temperature is needed for crystallization to occur [28]. In contrast, HfO₂ crystallites with dimension of 5–8 nm were observed in a 20 nm as-grown film [Fig. 5.17(a)], which suggests that the nucleation and growth mechanism follows the spinodal decomposition during the film deposition process at 350 °C. Figure 5.17(b) shows the line intensity profile integrated over the width of the rectangle in 5.17(a), which is

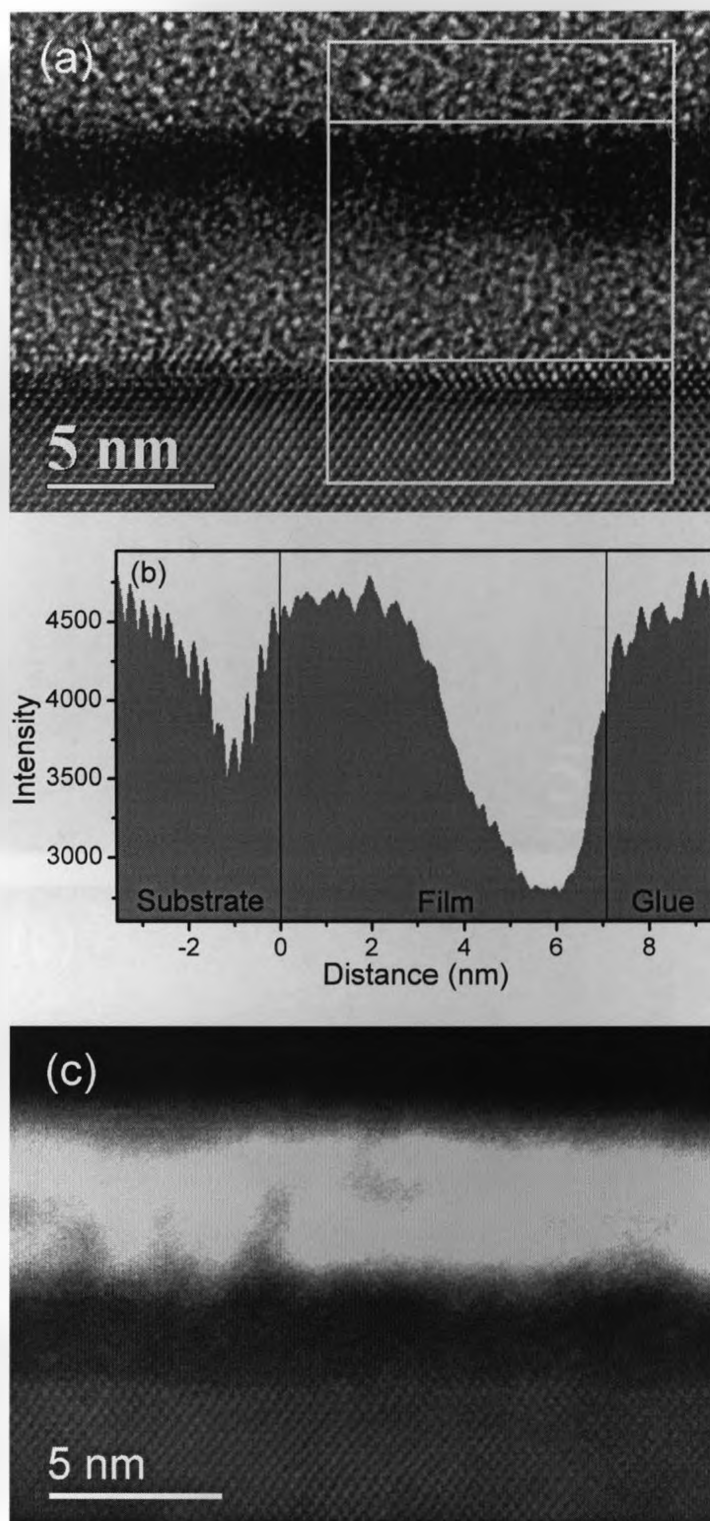


Figure 5.15: (a) BF image of the 6.1 nm film after 600 s anneal at 800 °C in N₂; (b) line intensity profile integrated over the width of the rectangle shown in (a); (c) DF image of the 6.1 nm film after 600 s anneal at 800 °C in N₂.

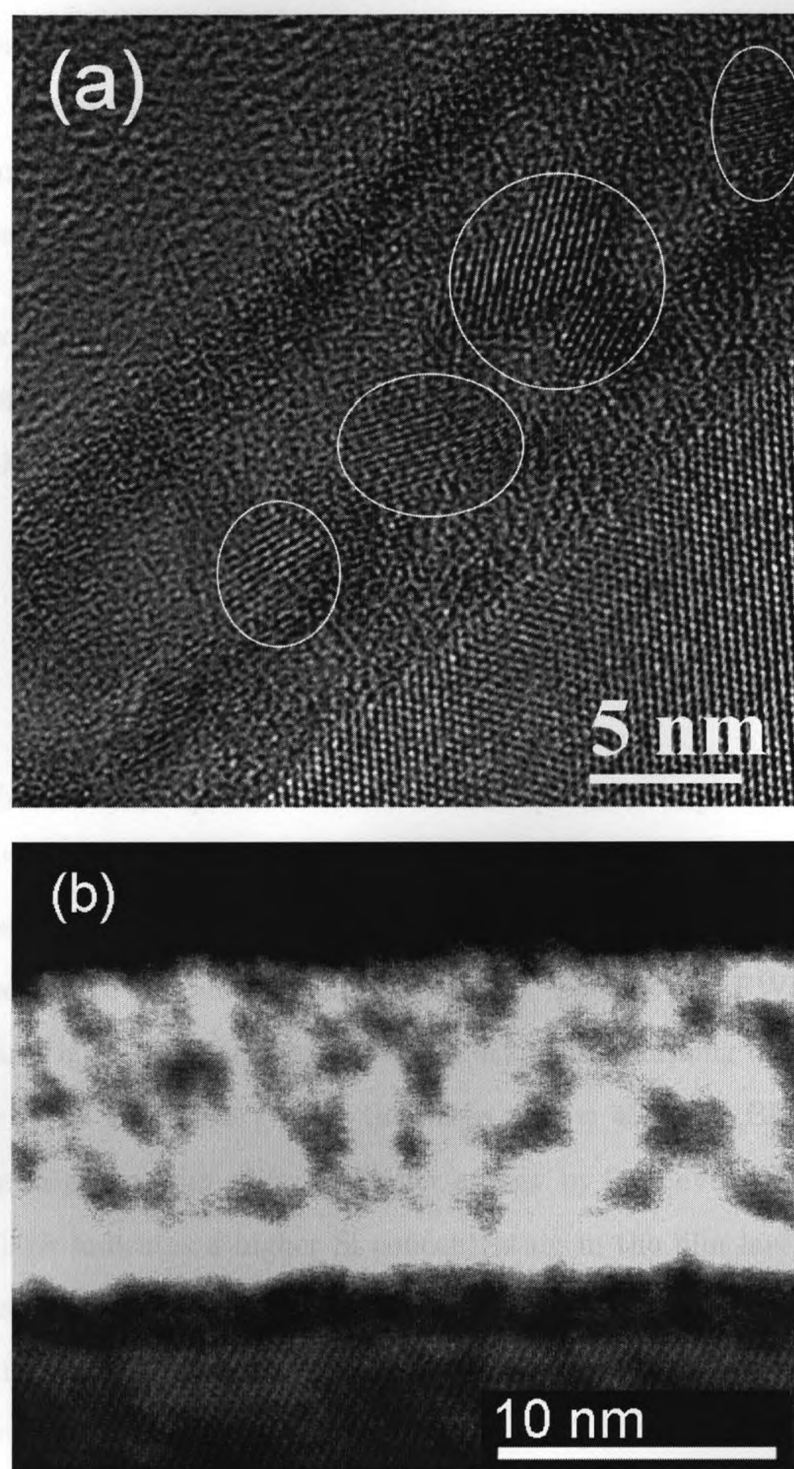


Figure 5.16: (a) BF and (b) DF images of the 12.5 nm film after 600 s anneal at 800 °C in N₂. Some of the crystalline regions are encircled.

the BF image of the 20 nm as-grown film. Figure 5.17(c) shows the DF image of this film. This film shows characteristics of the SDS in thin films: Hf-rich and Si-rich layers can be identified near the surface and interface and in the film bulk, Hf-rich clusters are mixed with Si-rich clusters randomly. The DF image is similar to the simulation result for the SDS in thin film geometry [18].

The plan-view BF images presented in Figs. 5.18(a) and 5.18(b) show the 6.1 nm film after RTA and 600 s anneal at 800 °C in N₂, respectively; these images also indicate a growth of the single-phase domains in the plane of the film during a longer time anneal.

5.2.5 XPS and MEIS analysis

Figure 5.19 shows the Si 2p, Hf 4f and O 1s XPS peaks at a photoelectron takeoff angle, θ , of 75° and 45° for the 5.3 nm film before and after RTA. The binding energies and intensities of the Si 2p peaks from the film for both photoelectron takeoff angles barely changed before and after RTA [Fig. 5.19(a)]. The BE and FWHM of Hf 4f_{7/2} peaks shown in Fig. 5.19(b) are given in Table 5.2. The sampling depth of the XPS signal for $\theta = 75^\circ$ is 1.37 times greater than that at $\theta = 45^\circ$. The BE of the Hf 4f_{7/2} peak from the as-grown film shifts to higher energy by 0.27 eV as θ increases from 45° to 75°, which indicates a higher Si concentration in the film layer closer to the substrate since the ARXPS signal is more surface sensitive at lower θ and a higher Hf concentration in Hf silicate films results in a shift of BE to lower energy [29]. This observation is in accord with the HRTEM images of Fig. 5.3. The intensity of the Hf 4f peak at $\theta = 45^\circ$ decreases after RTA, suggesting a diffusion of Hf atoms toward the substrate which results in an increase in the Hf concentration in the film layer closer to the substrate, and therefore a shift (0.14 eV) of the Hf 4f peak to lower BE at θ

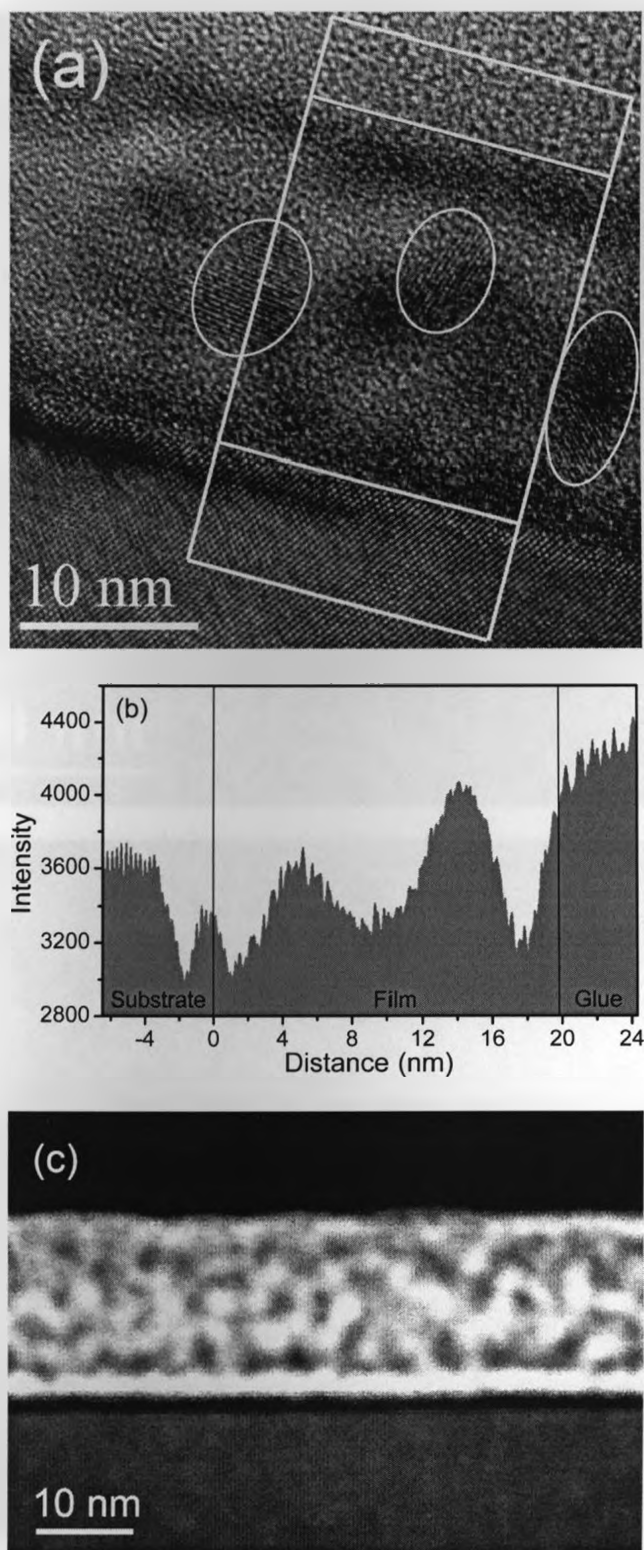


Figure 5.17: (a) BF image of a 20 nm as-grown film; (b) line intensity profile integrated over the width of the rectangle shown in (a); (c) DF image of the 20 nm as-grown film. Some of the crystalline regions are encircled.

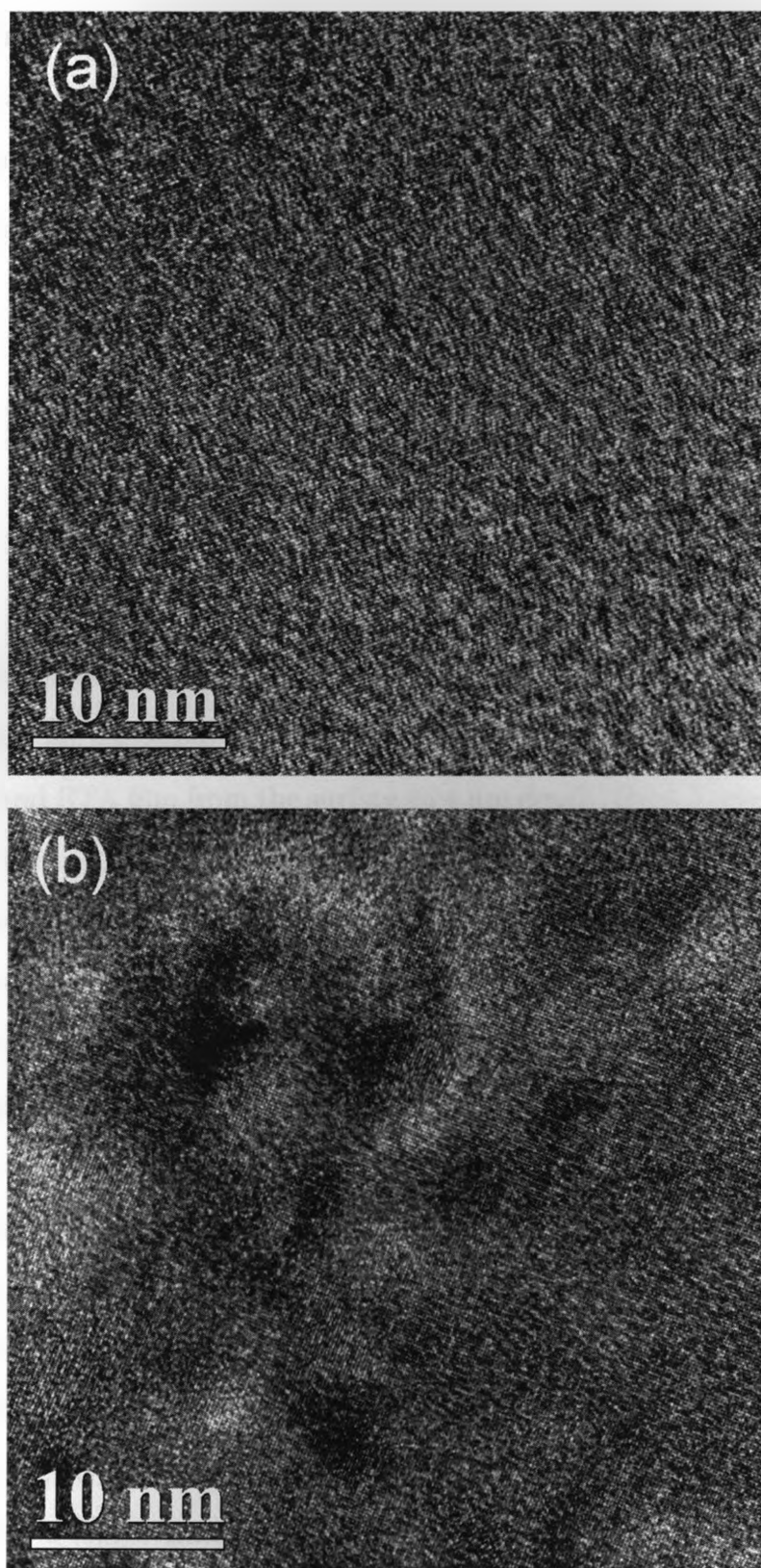


Figure 5.18: Plan-view BF images of the 6.1 nm film: (a) after RTA and (b) after a 600 s anneal at 800 °C in N₂.

$= 75^\circ$. The area of the O 1s peak corresponding to the Si–O–Hf bond component [Fig. 5.19(c), as-grown 45°] also decreases after RTA, which is in agreement with the observed decrease of the Hf 4f peak intensity at $\theta = 45^\circ$ after RTA.

Table 5.2: Summary of binding energies and peak widths of Hf 4f_{7/2} peaks shown in Fig. 5.19(b).

	θ	Hf 4f _{7/2}	
		BE (eV)	FWHM (eV)
As-grown	45°	18.25	1.26
	75°	18.52	1.26
RTA	45°	18.27	1.27
	75°	18.38	1.27

Figure 5.20 shows the Hf 4f ARXPS peaks (at $\theta = 45^\circ$ and 75°) for the 6.1 nm as-grown film, and for the same film after RTA and 600 s anneal at 800°C in N_2 . For the as-grown and RTA film from the surface to 4 nm depth, the 6.1 nm film (Figs. 5.5 and 5.8) has a similar structure as the 5 nm film (Figs. 5.3 and 5.7): i.e., a Hf-rich layer near the surface followed by a Si-rich layer. It is known that the number of photoelectrons that escape from the film surface decreases exponentially with depth. The contribution to the XPS peak from the Hf-rich layer closest to the substrate (Fig. 5.8) is negligible compared with the contribution from the layers above. It is therefore not surprising that Hf 4f XPS peaks from the 6.1 nm film have similar shifts as those peaks from the 5.3 nm film when θ changes from 45° to 75° before and after RTA. For the as-grown film, the Hf 4f_{7/2} peak shifts to higher energy by 0.23 eV as θ increases from 45° to 75° . At $\theta = 75^\circ$, the Hf 4f_{7/2} peak shifts 0.08 eV to lower energy after RTA compared with the as-grown film. After a 600 s anneal, the Hf 4f_{7/2} peaks shift to higher BE for both $\theta = 45^\circ$ and 75° , indicating that the Hf-rich phase in the film after a longer time anneal has a lower Hf concentration than that in the as-grown film or in the film after RTA. The intensities of these Hf peaks should not be compared because they are not aligned to a reference.

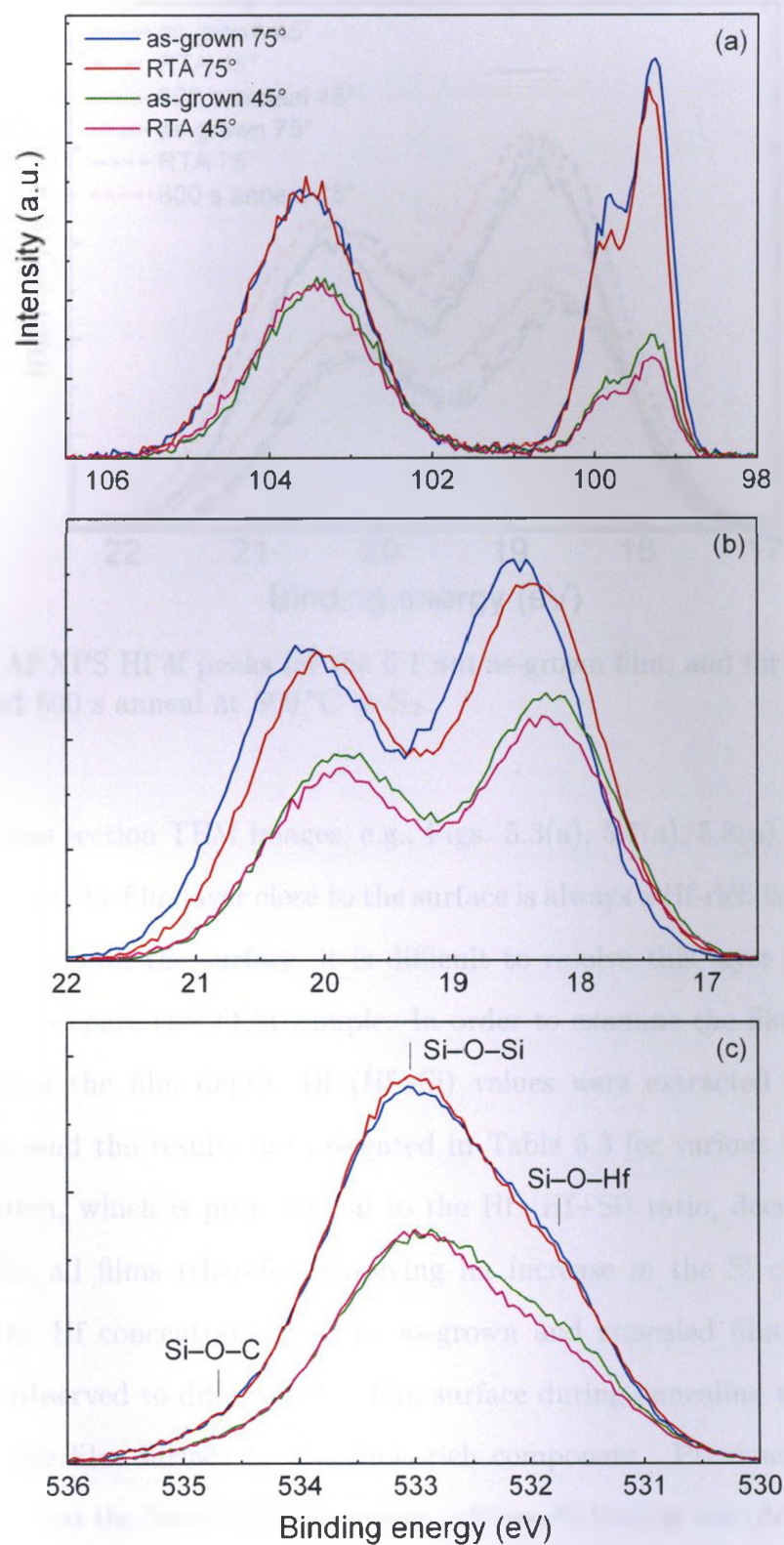


Figure 5.19: ARXPS peaks for the 5.3 nm film before and after RTA at $\theta = 45^\circ$ and 75° : (a) Si 2p; (b) Hf 4f; (c) O 1s.

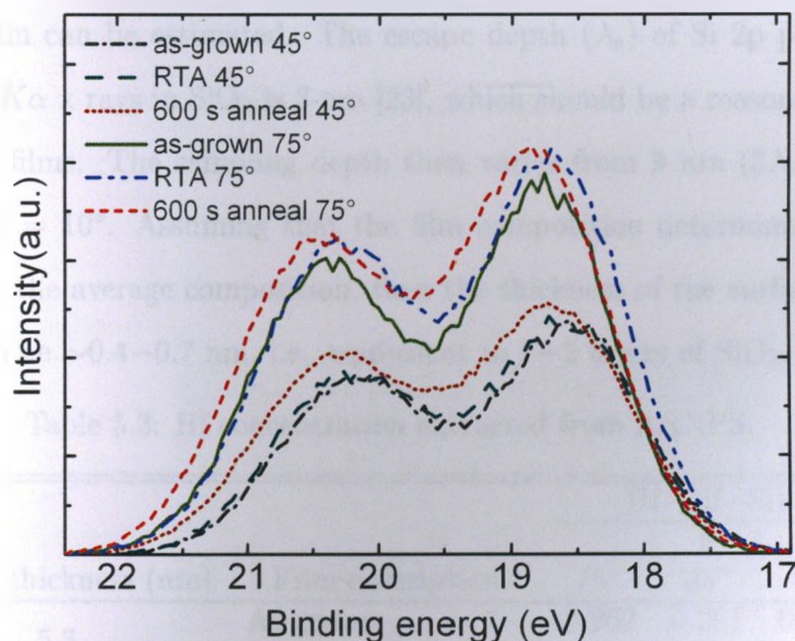


Figure 5.20: ARXPS Hf 4f peaks for the 6.1 nm as-grown film, and for the same film after RTA and 600 s anneal at 800 °C in N₂.

From those cross section TEM images, e.g., Figs. 5.3(a), 5.7(a), 5.8(a), 5.13(a), 5.14, etc., it seems that the film layer close to the surface is always a Hf-rich layer. However, if a Si-rich layer is on the surface, it is difficult to resolve this layer from the glue that is used to prepare the TEM sample. In order to examine the film composition as a function of the film depth, Hf/(Hf+Si) values were extracted from ARXPS measurements and the results are presented in Table 5.3 for various θ values. The Hf concentration, which is proportional to the Hf/(Hf+Si) ratio, decreases towards the surface for all films (therefore implying an increase in the Si concentration). Comparing the Hf concentration in the as-grown and annealed films at $\theta = 10^\circ$, more SiO₂ is observed to diffuse to the film surface during annealing which suggests a wetting of the film surface by the SiO₂-rich component. Previously, simulation results showed that the Si-rich phase contains >98 mol% SiO₂ in the (ZrO₂)_x(SiO₂)_{1-x} system after phase separation during 900 °C anneals [5]. Assuming that the Si-rich phase in the (HfO₂)_{0.25}(SiO₂)_{0.75} films is pure SiO₂, then the thickness of the surface

layer of the film can be estimated. The escape depth (λ_e) of Si 2p photoelectrons excited by Al $K\alpha$ x rays in SiO_2 is 3 nm [23], which should be a reasonable estimate for Hf silicate films. The sampling depth then varies from 9 nm ($3\lambda_e$) at $\theta = 90^\circ$ to 1.6 nm at $\theta = 10^\circ$. Assuming that the film composition determined at $\theta = 75^\circ$ corresponds to the average composition, then the thickness of the surface SiO_2 layer is estimated to be $\sim 0.4\text{--}0.7$ nm, i.e., equivalent to 1–2 layers of SiO_2 .

Table 5.3: Hf concentration extracted from ARXPS.

Film thickness (nm)	Film description	Hf/(Hf+Si)		
		θ		
		75°	45°	10°
5.3	As-grown	0.262	0.261	0.249
	RTA	0.260	0.249	0.225
6.1	As-grown	0.242	0.246	0.228
	RTA	0.225	0.236	0.198
	600 s anneal	0.220	0.223	0.189
12.5	600 s anneal	0.239	0.235	0.178
	RTA, HF etch, RTA	0.222	0.212	0.140

The film compositions (Table 5.3) calculated from the ARXPS peak intensities show that the 5.3 nm as-grown film has the same Hf concentration at $\theta = 45^\circ$ and 75° . However, Fig. 5.19(b) shows that the Hf 4f peaks of this film shift to higher energy as θ increases from 45° to 75° , indicating a lower Hf concentration in the film layer closer to the substrate. This apparent discrepancy can be explained by a simplified schematic for the Hf concentration gradient across the film depth as shown in Fig. 5.21. Layer 1 is SiO_2 and Layer 2 ($\text{Hf}_x\text{Si}_{1-x}\text{O}_2$) has a higher Hf concentration than Layer 3 ($\text{Hf}_y\text{Si}_{1-y}\text{O}_2$), i.e., $x > y$. The average composition of Layers 1 and 2 is the same as the composition of Layer 3. When the XPS measurements are taken at $\theta = 45^\circ$, most of the signal intensity comes from Layers 1 and 2. As θ increases to 75° , the contribution of photoelectrons excited in Layer 3 increases significantly; therefore the Hf 4f peak will shift to higher energy since Layer 3 has a lower Hf concentration

than Layer 2. However, the film composition calculated from XPS peak intensities will not change since Layer 3 has the average composition of Layer 1 and 2. The layered structure shown in Fig. 5.21 agrees with the HRTEM image shown in Fig. 5.3.

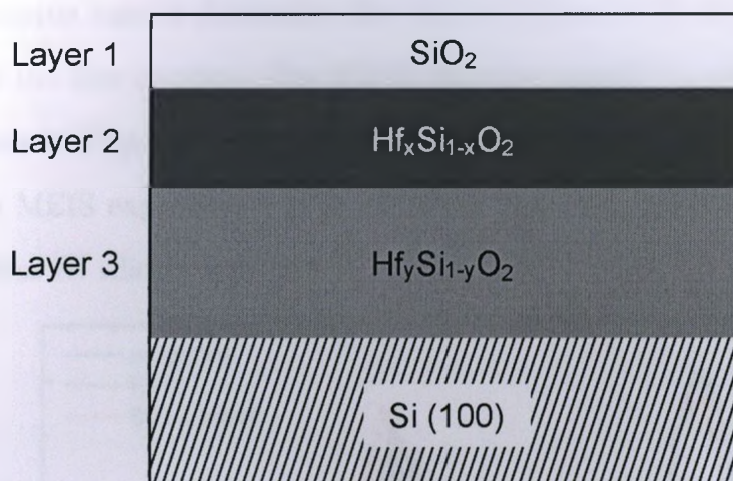


Figure 5.21: Schematic of the layered structure of the 5.3 nm film.

MEIS measurements were also performed to study film compositions and Hf depth profiles for the 6.1 nm film. Figure 5.22 shows the MEIS spectra for the 6.1 nm as-grown film and for the same film after RTA and 600 s anneal at 800 °C in N₂. The MEIS spectra are aligned to the O edge. As can be seen, the Si edges of the three spectra are also aligned. The Hf edge shifts slightly to lower energy after RTA, which indicates a diffusion of the HfO₂ component to the substrate or a diffusion of SiO₂ to the film surface. After a 600 s anneal, the Hf edge shifts to lower energy by 120 eV. If the density of the surface SiO₂ layer is assumed to be 2.2 g/cm³, then this energy shift corresponds to a diffusion of 0.35 nm SiO₂ to the film surface during the 600 s anneal process. This result is in good agreement with the estimate of the surface SiO₂ layer thicknesses from ARXPS data and confirms that the film surface is wetted by the SiO₂ layer after anneal. Compared to the as-grown film, the Si and O peaks are obviously wider after a 600 s anneal, which is due to the oxidation of the substrate

by O_2 impurities in N_2 , as mentioned earlier. The slight increase of the O and Si areas after RTA probably results from the same process. It should be pointed out that MEIS measures absolute areal density (i.e., the product ρt , where t is the film thickness and ρ is the film density) for the atomic constituents of a film. Therefore, the MEIS technique cannot determine the film thickness without a knowledge (or assumption) of the film density. The MEIS data are unable to resolve the layered structures shown in Figs. 5.5 and 5.8, since the ion beam extent in any direction (0.1–1 mm) in MEIS experiments is much larger than the composition wavelength observed for these Hf silicate films.

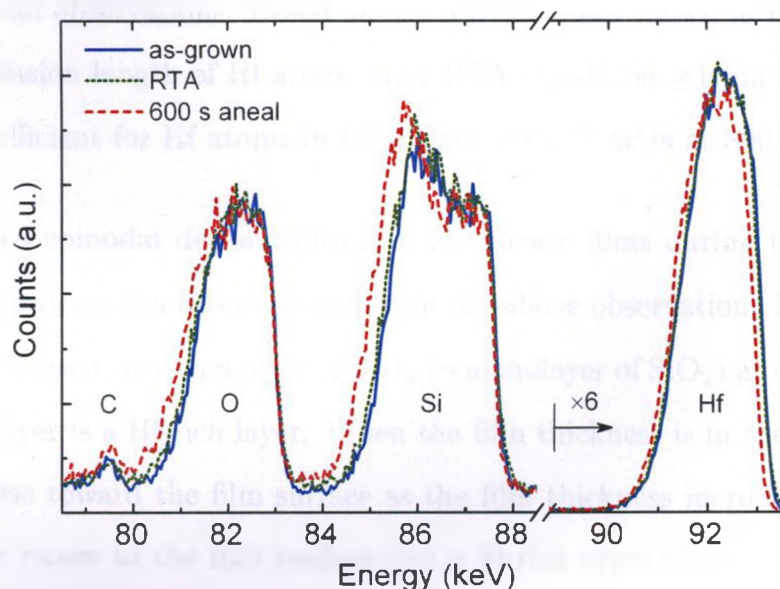


Figure 5.22: MEIS spectra of the 6.1 nm film: as-grown, after RTA and after 600 s anneal at 800 °C in N_2 .

5.3 Discussion and conclusion

Using grazing-incidence small angle X-ray scattering (GISAXS), Stemmer *et al.* [4] observed interference peaks in the horizontal cuts of their two-dimensional GISAXS intensity distribution, which correspond to a Hf concentration fluctuation in the plane

of the film with λ_C -values of 5 nm in the 4 nm $(\text{HfO}_2)_x(\text{SiO}_2)_{1-x}$ films ($x = 0.4$) after 1000 °C annealing. The observation was confirmed by their plan-view TEM image, which showed interconnected Hf-rich and Si-rich regions. However, these authors did not try to interpret vertical cuts of their GISAXS data but still concluded that their observations were inconsistent with SDS. In contrast, the TEM images reported in this thesis always show a layered structure for post-annealed films of thickness < 8 nm, which is consistent with SDS.

The diffusion coefficient of Hf in these $(\text{HfO}_2)_{0.25}(\text{SiO}_2)_{0.75}$ films can be estimated from the experimental observations. Based on the TEM images shown in Figs. 5.5(c) and 5.8(c), the diffusion length of Hf atoms after RTA should be ≥ 1 nm, which suggests a diffusion coefficient for Hf atoms in Hf silicate $\geq 10^{-19}$ m²/s at 800 °C.

Surface-directed spinodal decomposition in Hf silicate films during the film growth and annealing process can be envisioned from the above observation. In the as-grown film, there is always a very thin layer of SiO_2 (\sim monolayer of SiO_2) at the film surface. Beneath this layer is a Hf-rich layer. When the film thickness is in the range < 5 nm, Hf atoms diffuse toward the film surface as the film thickness increases, resulting in a Hf-rich layer closer to the film surface and a Si-rich layer closer to the substrate. As the film thickness increases to > 5 nm, some of the Hf atoms in the Hf-rich layer closer to the film surface diffuse towards the substrate. If the thickness is $1.5\lambda_C$, the film separates into three layers after RTA: a Si-rich layer sandwiched between two Hf-rich layers. If the film thickness is $\sim 2\lambda_C$, the film has a four-layer structure starting from the substrate surface: Si-rich, Hf-rich, Si-rich and Hf-rich. If the film thickness increases to $> 2\lambda_C$, the film loses its layered structure in the center of the film. After a longer time anneal, the layered structure coarsens and the composition wave grows. Crystallization of HfO_2 was observed in a 12.5 nm film after a longer time anneal at 800 °C or in a 20 nm as-grown film, indicating that the nucleation

and growth mechanism follows spinodal decomposition during the annealing or film deposition process.

The configurations in as-grown and annealed $(\text{HfO}_2)_{0.25}(\text{SiO}_2)_{0.75}$ films are qualitatively in agreement with the theory of SDSD, i.e., the composition waves were observed normal to the film surface. The observation that the composition of the film layer in contact with the substrate can be affected by film thickness has never been predicted by any SDSD simulation. Presumably, theoretical studies of SDSD could be modified to accommodate these new experimental results. At this time, it is difficult to study SDSD in $(\text{HfO}_2)_{0.25}(\text{SiO}_2)_{0.75}$ films to determine whether the composition wave obeys the growth law $\lambda_C \sim t^{1/3}$ [30], because: (i) TEM is a qualitative technique concerning atomic composition; (ii) SD in oxide systems is not easily controlled since the process occurs during the film deposition process; (iii) an alternative kinetic process, viz., nucleation and growth, can impede SD during the late stages of phase separation; and (iv) any O_2 impurity in the annealing N_2 ambient may also diffuse through the film and oxidize the substrate. While SDSD in the $(\text{HfO}_2)_{0.25}(\text{SiO}_2)_{0.75}$ thin films has been confirmed, the composition range for which $(\text{HfO}_2)_x(\text{SiO}_2)_{1-x}$ films experience SD and the resultant compositions of the phase-separated domains are still open questions.

The present observation of SDSD in $(\text{HfO}_2)_x(\text{SiO}_2)_{1-x}$ films may present significant device performance and reliability challenges for high- κ gate dielectric applications of pseudobinary alloy systems including ZrO_2 - SiO_2 , Y_2O_3 - SiO_2 and La_2O_3 - SiO_2 [5], and have effects on thin film applications for any two-component system whose phase diagram shows a miscibility gap. The ALD growth mechanism for two-component films could also be influenced by SDSD if the film surface is preferentially attracted to one of the two components.

BIBLIOGRAPHY

- [1] M. A. Quevedo-Lopez, M. R. Visokay, J. J. Chambers, M. J. Bevan, A. LiFatou, L. Colombo, M. J. Kim, B. E. Gnade, and R. M. Wallace, J. Appl. Phys. **97**, 043508 (2005).
- [2] D. A. Neumayer and E. Cartier, J. Appl. Phys. **90**, 1801 (2001).
- [3] S. Stemmer, Z. Chen, C. G. Levi, P. S. Lysaght, B. Foran, J. A. Gisby, and J. R. Taylor, Jpn. J. Appl. Phys. **42**, 3593 (2003).
- [4] S. Stemmer, Y. Li, B. Foran, P. S. Lysaght, S. K. Streiffer, P. Fuoss, and S. Seifert, Appl. Phys. Lett. **83**, 3141 (2003).
- [5] H. Kim and P. C. McIntyre, J. Appl. Phys. **92**, 5094 (2002).
- [6] J. W. Cahn, Trans. Metall. Soc. AIME **242**, 166 (1968).
- [7] C. Lupis, *Chemical Thermodynamics of Materials* (North-Holland, 1983).
- [8] J. W. Cahn, J. Chem. Phys. **42**, 93 (1965).
- [9] F. S. Bates and P. Wiltzius, J. Chem. Phys. **91**, 3258 (1989).
- [10] P. Wiltzius, F. S. Bates, and W. R. Heffner, Phys. Rev. Lett. **60**, 1538 (1988).
- [11] A. J. Bray, Adv. Phys. **43**, 357 (1994).
- [12] P. G. de Gennes, J. Chem. Phys. **72**, 4756 (1980).
- [13] R. C. Ball and R. L. H. Essery, J. Phys.-Condes. Matter **2**, 10303 (1990).
- [14] S. Puri and K. Binder, Phys. Rev. A **46**, R4487 (1992).
- [15] R. A. L. Jones, L. J. Norton, E. J. Kramer, F. S. Bates, and P. Wiltzius, Phys. Rev. Lett. **66**, 1326 (1991).
- [16] F. Bruder and R. Brenn, Phys. Rev. Lett. **69**, 624 (1992).
- [17] G. Krausch, C.-A. Dai, E. J. Kramer, and F. S. Bates, Phys. Rev. Lett. **71**, 3669 (1993).
- [18] S. Puri and K. Binder, J. Stat. Phys. **77**, 145 (1994).

- [19] S. Puri and K. Binder, Phys. Rev. E **49**, 5359 (1994).
- [20] S. Das, S. Puri, J. Horbach, and K. Binder, Phys. Rev. E **72**, 061603 (2005).
- [21] M. Geoghegan and G. Krausch, Prog. Polym. Sci. **28**, 261 (2003).
- [22] J. Chen, W. J. Yoo, and D. S. H. Chan, J. Electrochem. Soc. **153**, G483 (2006).
- [23] Z. H. Lu, J. P. McCaffrey, B. Brar, G. D. Wilk, R. M. Wallace, L. C. Feldman, and S. P. Tay, Appl. Phys. Lett. **71**, 2764 (1997).
- [24] D. A. Cole, J. R. Shallenberger, S. W. Novak, R. L. Moore, M. J. Edgell, S. P. Smith, C. J. Hitzman, J. F. Kirchhoff, E. Principe, W. Nieveen, et al., J. Vac. Sci. Technol. B **18**, 440 (2000).
- [25] D. F. Mitchell, K. B. Clark, J. A. Bardwell, W. N. Lennard, G. R. Massoumi, and I. V. Mitchell, Surf. Interface Anal. **21**, 44 (1994).
- [26] S. Puri and K. Binder, Phys. Rev. E **49**, 5359 (1994).
- [27] J.-P. Maria, D. Wicaksana, A. I. Kingon, B. Busch, H. Schulte, E. Garfunkel, and T. Gustafsson, J. Appl. Phys. **90**, 3476 (2001).
- [28] G. Pant, A. Gnade, M. J. Kim, R. M. Wallace, B. E. Gnade, M. A. Quevedo-Lopez, and P. D. Kirsch, Appl. Phys. Lett. **88**, 032901 (2006).
- [29] M. D. Ulrich, J. G. Hong, J. E. Rowe, G. Lucovsky, A. S.-Y. Chan, and T. E. Madey, J. Vac. Sci. Technol. B **21**, 1777 (2003).
- [30] G. Krausch, C.-A. Dai, E. J. Kramer, and F. S. Bates, Phys. Rev. Lett. **71**, 3669 (1993).

CHAPTER 6

CONCLUSIONS

Hf silicate films were grown on p-type Si(100) substrates by ALD using the precursors TDEAH and TMBS. Based on the analysis of carbon impurities in the films (Chapter 4), it was found that C contamination can be reduced by applying a series of post-deposition processes. First, the introduction of O₂ into the film growth chamber after film deposition eliminates the C–Hf bond. Since the C–Hf bond can be oxidized at room temperature in an atmospheric ambient, the substrate temperature should be kept low so that the O₂ does not diffuse through the film where it may oxidize the substrate to form a (thin) SiO₂ layer. Second, a vacuum rapid anneal performed at 800°C removes the unreacted precursor molecules. Following these steps, it is possible to lower the carbon contamination to <1%.

In this study, due to the reaction mechanism discussed in Chapter 4, the Hf concentration [i.e., (Hf/Hf+Si)] can only be varied in a small range (0.22–0.30) by adjusting both the substrate temperature and the TMBS pulse time. Calculations show that the dielectric constant of (HfO₂)_x(SiO₂)_{1–x} increases linearly with the Hf content, i.e., the x value [1], which is in very good agreement with some recent experimental measurements [2, 3]. It is therefore expected that the (HfO₂)_{0.25}(SiO₂)_{0.75} has a κ -value of ~ 8.5 . This value is too low to be used in today's transistors. In comparison, Al₂O₃

has a κ -value in the range of ~ 8 – 10 [4]. The EOT of the gate dielectric produced in Intel's 45 nm technology is 1 nm. If $(\text{HfO}_2)_{0.25}(\text{SiO}_2)_{0.75}$ were used as the gate insulator in future transistors, then its physical thickness would be < 2 nm and there is almost no room for further scaling. In order to enhance the Hf content in the Hf silicate films deposited by TDEAH and TMBS, the film deposition process requires some modification. For example, water can be introduced to react with TDEAH to form HfO_2 , thereby increasing the $\text{Hf}/(\text{Hf}+\text{Si})$ ratio.

If the film composition can be modified by changing the film deposition process to ensure the required high- κ value, then the observation of SDSD in Hf silicate films presents a large challenge for applying these films as gate dielectrics. As we have seen, those $(\text{HfO}_2)_{0.25}(\text{SiO}_2)_{0.75}$ films that are thinner than 8 nm separate into a layered structure during the film deposition process at 350°C and the subsequent annealing process at 800°C , with one phase containing a very low Hf concentration. This Si-rich layer has a low κ -value and a thickness of 1–2 nm, which would then make an EOT of < 1 nm unachievable.

The main reason for studying the $(\text{HfO}_2)_x(\text{SiO}_2)_{1-x}$ system for use as a possible gate dielectric material is that the crystallization temperature of HfO_2 is low, 350°C for a 60 nm film [5], i.e., much lower than a typical dopant activation temperature, $\sim 900^\circ\text{C}$. Although the onset of crystallization temperature of HfO_2 increases with decreasing film thickness [6], the 2 nm HfO_2 film was found to crystallize at 800°C [7]. In 2007, Intel announced that their first generation high- κ + metal gate transistors are made by the gate-last process to avoid annealing the gate electrode at high temperature [8]. Using the gate-last process, the gate dielectric need not be annealed at high temperature. Thus, HfO_2 is probably the best choice for a high- κ gate dielectric material.

BIBLIOGRAPHY

- [1] P. Broqvist and A. Pasquarello, Appl. Phys. Lett. **90**, 082907 (2007).
- [2] K. Tomida, K. Kita, and A. Toriumi, Appl. Phys. Lett. **89**, 142902 (2006).
- [3] S. V. Elshocht, U. Weber, T. Conard, V. Kaushik, M. Houssa, S. Hyun, B. Seitzinger, P. Lehnem, M. Schumacher, J. Lindner, et al., J. Electrochem. Soc. **152**, F185 (2005).
- [4] G. D. Wilk, R. M. Wallace, and J. M. Anthony, J. Appl. Phys. **89**, 5243 (2001).
- [5] M. Modreanu, J. Sancho-Parramon, D. O'Connell, J. Justice, O. Durand, and B. Servet, Mater. Sci. Eng. B **118**, 127 (2005).
- [6] P. S. Lysaght, J. C. Woicik, M. A. Sahiner, B.-H. Lee, and R. Jammy, J. Non-Cryst. Solids **354**, 399 (2008).
- [7] F. Bohra, B. Jiang, and J.-M. Zuo, Appl. Phys. Lett. **90**, 161917 (2007).
- [8] M. T. Bohr, R. S. Chau, T. Ghani, and K. Mistry, IEEE Spectr. **44**, 29 (2007).

APPENDIX A

COPYRIGHT PERMISSION

A.1 Copyright permission for material contained within Chapter 3 and Chapter 4

Request for Permission to Reproduce or Re-Publish ECS Material

Please fax this form to: The Electrochemical Society (ECS), Attn: Permissions Requests, 1.609.737.2743.
You may also e-mail your request to: copyright@electrochem.org. Include all the information as required on this form. Please allow 3-7 days for your request to be processed.

I am preparing a (choose one): ☐ paper ☐ chapter ☐ book ☒ thesis

entitled: Growth and Characterization of Hafnium Silicate Films

to be published by: The University of Western Ontario

in an upcoming publication entitled: _____

I request permission to use the following material in the publication noted above, and request nonexclusive rights for all subsequent editions and in all foreign language translations for distribution throughout the world.

Description of material to be used—Indicate what material you wish to use (figures, tables, text, etc.) and give the full bibliographic reference for the source publication. You may attach a separate list, organized by ECS title.

I would like to use Figs. 1-8, Figs. 10-11, Tables I-II and 90% of the text of the article entitled
"Atomic Layer Deposition of Hafnium Silicate Thin Films Using Tetrakis(diethylamido)hafnium
and Tris(2-methyl-2-butoxy)silanol" [J. Liu, W. N. Lennard, L. V. Goncharova, D. Landheer,
X. Wu, S. A. Rushworth, and A. C. Jones, J. Electrochem. Soc., 156, G89, (2009)] in my PhD
thesis.

Signature: _____ Date: 2009/09/18

Name: Jian Liu

Address: Department of Physics and Astronomy

The University of Western Ontario

1151 Richmond Street, London, Ontario, Canada, N6A 3K7

Telephone: _____ Fax: _____

E-mail: _____

Permission is granted to include the above-referenced paper in your thesis, provided that you obtain permission of the other individual authors. In the thesis, please acknowledge the authors and the citation given above, and include the words: "Reproduced by permission of ECS — The Electrochemical Society."

Sept. 25, 2009
Date

Ann F. Goedkoop, Director of Publications

A.2 Copyright permission for material contained within Chapter 5



AMERICAN PHYSICAL SOCIETY

One Physics Ellipse, College Park, MD 20740 · <http://www.aps.org>

September 18, 2009

Jian Liu
Department of Physics and Astronomy
The University of Western Ontario
1151 Richmond Street
London, Ontario
Canada, N6A 3K7

Ref # 8202

Thank you for your permission request dated on September 18, 2009. We are pleased to grant you a non-exclusive, non-transferable permission, English rights, limited to **print and electronic format**, provided you meet the criteria outlined below. Permission is for a one-time use and does not include permission for future editions, updates, databases, translations, or any other matters. Permission must be sought for each additional use. This permission does not include the right to modify APS material.

Please print the required copyright credit line on the first page that the material appears: "Reprinted (abstract/excerpt/figure) with permission from [FULL REFERENCE CITATION] as follows: authors names, journal title, volume number, page number and year of publication. Copyright (YEAR) by the American Physical Society.

The following language must appear somewhere on the website: "Readers may view, browse, and/or download material for temporary copying purposes only, provided these uses are for noncommercial personal purposes. Except as provided by law, this material may not be further reproduced, distributed, transmitted, modified, adapted, performed, displayed, published, or sold in whole or part, without prior written permission from the American Physical Society."

Provide a hyperlink from the reprinted APS material (the hyperlink may be embedded in the copyright credit line). APS's link manager technology makes it convenient and easy to provide links to individual articles in APS journals. For information, see: <http://publish.aps.org/linkfaq.html>

You must also obtain permission from at least one of the authors for each separate work, if you haven't done so already. The author's name and address can be found on the first page of the published Article.

Use of the APS material must not imply any endorsement by the American Physical Society.

Permission is granted for use of the following APS material only:
Article, Phys. Rev. B Vol. 80, 041403 (2009)

Permission is limited to the single title specified or single edition of the publication as follows:
A PhD thesis entitled "Growth and characterization of hafnium silicate films" to be published by The University of Western Ontario.

If you have any questions, please refer to the Copyright FAQ at: <http://forms.aps.org/author/copyfaq.html> or contact me at assocpub@aps.org.

Sincerely,

Eileen LaManca
Publications Marketing Coordinator